DOTTORATO DI RICERCA

SEZIONE SCIENZE DELL'INGEGNERIA CIVILE

CICLO DEL CORSO DI DOTTORATO

XXX

Towards the non-destructive assessment

of mechanical properties in roads and railways:

new concepts and methodologies

PhD Candidate:

Luca Bianchini Ciampoli   _____

Tutor:

Prof. dott. ing. Andrea Benedetto   _____

Co-tutor:

Dott. ing. Fabio Tosti   _____

PhD coordinator:

Prof. dott. ing. Gianmarco De Felice   _____

Towards the non-destructive assessment of mechanical properties in roads and railways: new concepts and methodologies

Towards the non-destructive assessment of mechanical properties in roads and railways: new concepts and methodologies

Luca Bianchini Ciampoli

Abstract

A proper maintenance of the transport infrastructure asset is a factor of paramount importance with dramatic macro-economic and safety implications. In this framework, the spreading of maintenance approaches based on the critical conditions of an infrastructure has determined a growing demand for non-destructive testing (NDT) methods for the non-intrusive assessment and the health monitoring of civil engineering infrastructures.

Amongst the various NDTs available in the market, ground-penetrating radar (GPR) is a well-acknowledged electromagnetic tool capable to assess the geometric and physical properties of the subsurface. GPR systems equipped with air-coupled antennas and mounted on dedicated instrumented vehicles allow to investigate long distances with a very high productivity. This feature makes the system particularly suitable for transport asset monitoring purposes.

This thesis focuses on the use of GPR and other NDTs for the assessment of the mechanical response of road pavements and track-beds for highway and railway engineering applications.

In this regard, the main aim of the research is to provide new experimental-based methodologies for the detection of decay areas within a transport infrastructure network. This is crucial to plan maintenance effectively and avoid potential growth of damage.

In regard to the roads, a parametric model capable to assess the overall stiffness of flexible pavements is proposed. The model considers as input information the thickness of the base layer and the potential presence of clayey particles in the deeper layers. These information are assessed using GPR. The model is developed using ground-truth data collected by deflection-based NDT equipment for calibration purposes.

With regard to the railways, a geometric and physical assessment of the ballast aggregates composing the railway track-bed is obtained by both time domain and frequency-based analyses of the data collected by air-launched GPR systems.

The results achieved demonstrate the viability of the proposed methodologies for application purposes and inclusion in survey protocols as part of assessment programs for the maintenance of transport infrastructure assets.

Contents

List of Figures

List of Tables

Introduction

Background

The course of history witnesses that the capability of connecting populations, and ensuring safe and fast movements of armies, people, goods throughtout territory is at the foundation of every great nation or empire ever existed.

It is here worthwhile to recall the words of Dionysius of Halicarnassus, a Greek historian and teacher of rhetoric who flourished during the reign of Caesar Augustus, most likely the brightest demonstration of the concept above.

> *Rome's greatness rested on three wonderful achievements:*
> *roads, aqueducts, and the sewage system*
>
> DIONYSIUS OF HALICARNASSUS

To underpin this statement, the road network realised by the Romans held for centuries a key role in land transportation in Europe, Asia and Africa, and it is nowadays still largely employed by modern vehicles.

Actually, most of the economic activities have always developed on roads and water systems. Accordingly, most of the economists consider the public infrastructure as a critical matter for a country's growth. As far as the transport infrastructures are concerned, road traffic has started to become a relevant issue after the Industrial Revolution. Rapid and safe tradings of good bacame a major concern for trade companies, that aimed at maximising the profits while minimising the related risks. This concept was well stressed by Adam Smith, as reported hereafter:

> *Good roads, canals, and navigable rivers by diminishing the*
> *expense of carriage, put the remote parts of the countries more*
> *nearly upon a level with those in the neighbouring town. They are*
> *upon that account the greatest of all improvements*
>
> ADAM SMITH

As a result, mechanised transport technologies such as cars and trains were shortly patented and commercialised on the market, which involved a general need for new and more performing infrastructures. From that momento onwards, road and railway networks started to blossom all over the industrialised countries. Hence, even the most remote areas could be connected with the most flourished economical and cultural centres.

Nowadays, the extent of transportation assets recorded in a country, is a relatively good indicator of the industrialisation rate. In fact, as confirmed by Tab. 1, the most developed world areas are actually related to transport assets with the highest quality.

Area	Roads	Railways
Europe	4.89	4.00
North America	4.00	3.66
South America	3.29	1.78
Asia	4.29	3.67
Africa	3.49	2.43
Australia	4.70	3.70

Table 1: Average quality of transport assets, 1 (low) - 7 (high). Source: *World Economic Forum*

Of couse, the extent of the assets has to comply with high serviceability requirements, in order to be a reliable indicator of development. In other words, when considering the transport assets of a country two main questions must be raised, namely, *how effective is the development of the transport infrastructure in the country?* and *what is its actual condition?*

Most of the attention is frequently focused on realising new public infrastructures, that turn out to provide high level of visibility and political consensus. This is rather frequent in developing countries. On the other hand, very limited attention is paid on the maintenance management of the existing asset. Such a negligence can generate serious macroeconomic issues [1].

In general terms, maintenance operations are referred to as those activities that allow the public infrastructures to effectively provide the service as per the design task [2]. The effects of a deficient maintenance program involve, on a different scale and extent, the public administrations that often need to resurface or reconstruct the infrastructure before the end of its operational time, and the private users who travel on damaged infrastructures. This causes many drawbacks, such as a crucial decrease of safety, damaging of vehicles and an increase of the travel times.

There is still an active debate in the scientific community about the optimal mix of investments on 'capital' (new projects) and 'current' (maintenance) expenditures. However, many authors agree that without a sufficient allocation of resources on the latter, the former may have even negative macroeconomic effects [1] [3], highlighting the importance of an effective maintenance activity.

The so called maintenance management systems, which schedule the time, define the methodology and evaluate the cost of every maintenance activity, are fundamental tools to achieve a reliable management of the infrastructure facilities [4]. *Maser* [5] proposes a three-level vertical system to classify the decision process occurring within the context of an effective network management:

1. *Strategic planning.* At this level, priorities and budgets are assigned to the activities at the network level. Decisions at this stage involve long-term projections, project selections, manpower, equipment management and financial planning. Therefore, they require an overall knowledge about the state of the managed asset. Such pieces of information are provided by levels 2 and 3.

2. *Operational and control.* Decisions are here taken with regard to the inspection methodologies, the specific intervention options (repair, replace, rehabilitate) and their cost/benefit ratio and priority. At this level, main- tenance needs and guidelines are defined at the level of a single infrastructure using part of the data provided by next level.

3. *Tactical.* Decisions related to the inspection of components are made at this level. Within these components, timing and frequency of the surveys, required detail of the information and the scheduling of maintenance effectiveness controls are worthy of mention.

Firstly, the decision-making chain expressed above is a *bottom-up* process. The data gathered through Level 3 must be synthesized in Level 2 in order to address the maintenance policies of the facility. Afterwards, outputs from the second stage are integrated at the network level into Level 1 up to the definition of long-term asset improvement plans, with related financial considerations. Hence, financial constraints are set, due to political-economic conditions and the process turns out to become a *top-down* one.

The maintenance problem

According to the above, the Tactical Level is a crucial decisional step affecting the effectiveness of the whole maintenance program. When, where and how to carry out inspection surveys over the infrastructure network is highly dependent on the type of maintenance that is expected to perform. Indeed, the maintenance activities are traditionally sorted into two main approaches [6]:

- *Corrective maintenance.* The maintenance is performed when a breakdown or an evident failure is noticed over the network [7]. Corrective maintenance can be performed also with the system continuing to run, for instance, in case of a large network recording a failure of one out of two parallel connections. However, corrective maintenance can be extremely expensive due to several reason. First of all, the cost of restoring operations is not linearly dependent on the extent of the item failure. Secondly, a major failure can cause a large amount of correlated damages to other substructures, and, in addition several collateral effects (e.g., safety issues or lacking of operational efficiency). Also, the failure can occur at a time that is most inconvenient to both the user and owner, thereby creating serious inconveniences over the network.

- *Preventive maintenance.* Maintenance, either scheduled in time- and space-based intervals, is performed in order to prevent any possible breakdown. With regard to the transport infrastructures, a preventive approach to the asset maintenance is strongly recommended by the experts [1][2] and, to date, largely used by managing bodies.

However, it is again possible to recognize different sub-categories, when referring to preventive maintenance [6]:

- *Predetermined maintenance.* The interventions are scheduled on a time-based criterion (e.g. road resurfacing every 10 years). Such type of maintenance is priorly planned and then performed at a convenient time due to costs reduction. However, this approach does not account for the actual condition of the asset. In fact, the infrastructure may not need maintenance at all, or it may even end-up into a worse final condition, as a result of the maintenance activity [8].

- *Condition-based maintenance (CBM)*[9]. The interventions are scheduled on the basis of the actual need for maintenance, recorded on the site. The intervals between interventions, hence, are dynamic.
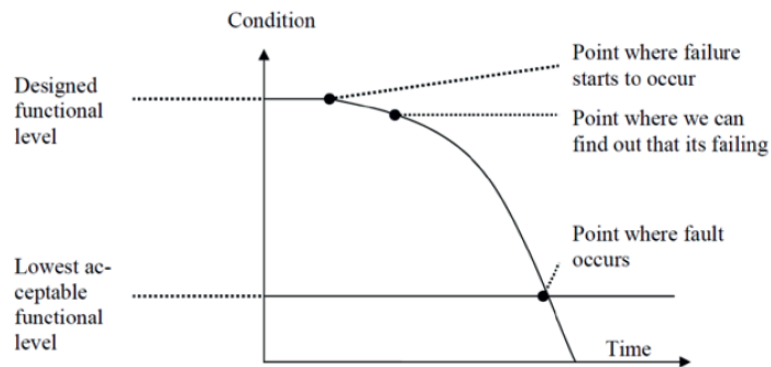
Figure 1: The Condition-Based Maintenance strategy [12]

As shown in Fig. 1, a CBM approach allows to minimize wastes in maintenance expenditures, as it prevents from any useless intervention, while ensuring to perform maintenance prior to increase of costs. To this effect, a field-related literature review points it out as the most suggested by researchers [10] [11]. On the other hand, it requires a comprehensive survey plan, capable of ensuring a correct and updated knowledge of the asset conditions.

Traditional inspection methods aimed at road infrastructures maintenance rely on the use of destructive techniques, such as coring, drilling or otherwise removing part of the structure to allow inner visual inspections (e.g., bridge deck inspections) or to verify the material performances through standard laboratory tests [13].

Despite the high reliability of such techniques, they hold several drawbacks. First, they are expensive and time-consuming. In addition, results can not be extended to long distances if compared to the large-scale extension usually required for road inspections. These factors are highly impacting on the effectiveness and efficiency of maintenance as well as upon the cost and time of the decision making process illustrated in previous section.

To overcome the limitations above, several non-destructive testing or evaluation (NDT/NDE) techniques have been introduced in the market [14]. NDTs can be roughly sorted into acoustic [15], optical [16], electromagnetic [17] and thermographic [18] methods. Actually, these technologies turn out to be faster and more cost effective, thereby leading the way towards semi-continuous and updated knowledge of the whole managed networks, based on both visual and performance-based, on-site inspections.

Summarizing up the evolution of maintenance over time (Fig 2), it is possible to recognize common features in the focus of managers and researchers.
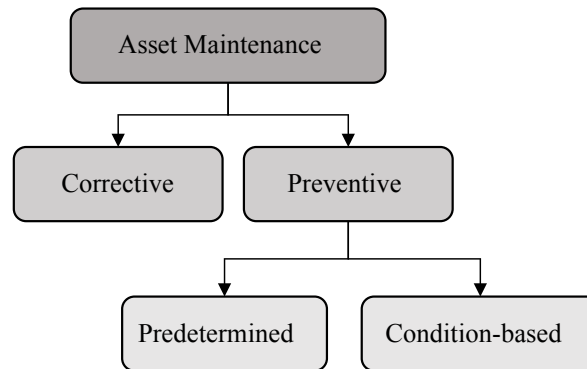
Figure 2: On overview of the current maintenance approaches

Indeed, by considering the life-time of an infrastructure as divided into a nominal life and a period between the first extraordinary maintenance measure and the final decommissioning, the final goal for a managing administration has always been to find as early as possible a trade-off between these two conditions, in order to reduce the extent of maintenance activities.

This type of of *symptomatic* approach is aimed at recognizing the signs of damages prior than their evolution requires structural countermeasures. In view of this, the great resources spent in research over the last decades, have been addressed towards an early-stage detection of distresses. As a result, researchers' studies and applications, supported by the growing technology facilities and the spreading of NDTs, allowed to skip from a corrective intervention (i.e., used once a structural failure had been detected) to a condition-based intervention (i.e., intervention carried out as soon as a millimetric deformation is observed). Beyond any doubt, this is a remarkable achievement, that have consistently raised the maintenance efficiency over years.

Nevertheless, this time-chasing process has limitations, by definition. In fact, current technologies are yet capable of detecting sub-millimetric deformations also in a very early-stage process of damage. Of course, new challenges can be tackled regarding the accuracy and spatial resolution of any relevant information, but the restrained possibilities of future breakthroughs are something to worry about, as far as maintenance expenditures are still a major concern for administrations and managing companies.

Furthermore, it is worthy of mention that a visible deterioration at the surface level in multi-layered systems such as road and railway superstructures, is usually related to a more advanced stage of decay with deeper distresses involved. On the other hand, considering the high non-linearity of the damages evolution process in

a multi-phase materials, the performance-based measurements are not sufficient to gather a comprehensive knowledge of the process itself.

Accordingly, symptomatic approaches, even at the greatest accuracy, can hold by definition some constraints - by definition - that may limit their own effectiveness.

A novel maintenance concept

In view of above, it could seem clear that great advances in maintenance matter will be hardly achievable in the next future, as far as the attention keeps to be focused on methodologic rather than conceptual issues.

For the sake of clarity, it is here useful to make use of a medical analogy: in the case a certain disease occurs, the curing physician can well treat the patient with drugs capable of reducing or even eliminating the symptoms of the disease. Of course, the patient will feel relief. If the chosen treatment was particularly suitable for the specific disease, he will even feel totally healed. However, as long as the causes behind the symptoms are not removed, they will appear again, sooner or later. This is obviously strictly related to the specific case.

Analogously, in the case of a "sick" infrastructure, the approach is to detect the effects of deteriorations and to restore the initial conditions. Obviously, the sooner these effects are identified, the less extensive the restoring measure will be. This type of approach has been referred to as corrective or preventive maintenance in the previous sections, depending on the timing of the intervention. Nevertheless, just as in case of the medical patient, if the causes of the distresses are not tackled, they will certainly reoccur.

Therefore, it is author's belief that, in order to raise the impact of research, so opening the path to new possible breakthroughs in infrastructure maintenance, it is mandatory to radically change the point of view upon the matter, stepping out this run for an earlier detection of damages, and moving from a *symptomatic* to a *causative*, predictive concept of maintenance.

In such a context, new challenges may be tacked on a more effective use of NDTs not only for sensing the visual effect of damage or a drop in material performances, but rather for detecting the critical factors triggering the deterioration of the infrastructures.

Indeed, as shown in Fig. 3, the development of methodologies and models for detection of the critical factors related to damage, would allow specific rehabilitative interventions prior to the first distress. In this regard, differently
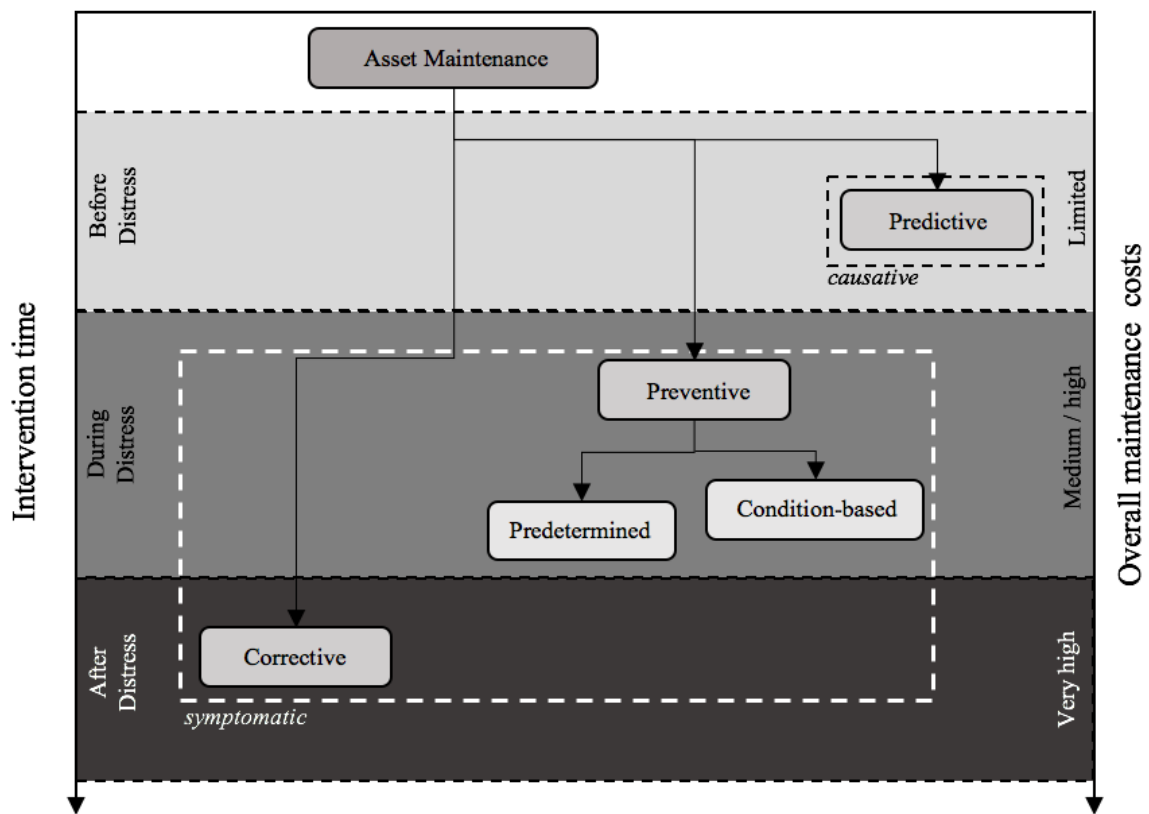
Figure 3: A new point of view in infrastructure maintenance

from symptomatic approaches, causative maintenance acts on the nominal portion of the asset life-cycle. Removing the causes prior to the occurrence of their effects might extend the nominal life of the infrastructure, which will theoretically undisturbed.

Such a result holds significant impacts on the overall maintenance costs at the network scale and, more important, on the safety levels for the network users. Indeed, as the portions of the network characterised by high levels of critical factors are detected, a map of risks for the infrastrucutres condition at the network level might be extracted, which is crucial in assuming priorities in monitoring scheduling and actions development.

Objectives

In such a framework, the aim of this work is to improve the effectiveness and efficiency in the application, integration and fusion of different non-destructive testing methods for transport infrastructure causative maintenance in order to stimulate researchers' and professionals' attention in this promising field.

More specifically, this thesis will focus on novel pilot models for the assessment

and the health monitoring of road pavements and railway track-beds. Combination of different NDTs will be considered in this thesis, with the ground-penetrating radar (GPR) being the reference equipment. The above Aim will be pursued with the following objectives:

- Development of a self-consistent approach for evaluating road flexible and semi-rigid pavement stiffness at the network level avoiding the use of destructive samplings

- Development of prediction models for inferring the physical characteristics of the track-bed in ballasted railways

Several practical implications may result from this work. Among the most relevant, it is possible to mention:

- The implementation of these GPR-based models in the network inspection procedures would allow a quasi-continuous knowledge of the state of the asset, at competitive time and cost expenses

- A great contribution on the reliability predictive service life models can be provided, as the amount of relevant physical parameters (e.g., water and clay contents) and the loss of layer moduli may be quantified more accurately

Thesis outline

- Chapter 1: The functioning principles of the used NDTs are herein given, with particular reference to the highway and railway engineering applications.

- Chapter 2: Road applications are presented in this chapter. The description involves the experimental activity, the processing and interpreting stage, and the presentation of the results.

- Chapter 3: Railway applications are herein tackled. The description involves both laboratory and on-site experimental activity, the processing and interpreting stage, and the presentation of the results.

- Chapter 4: In this chapter procedural insights are provided about further integrations of NDTs for both roads and railway applications.

- Chapter 5: General conclusions from the study are listed, and final recommendation for the practical use of the proposed models are given.

Chapter 1

Theoretical framework

1.1 Electromagnetic fundamentals

1.1.1 GPR principles

An aware use of GPR requires a comprehensive understanding of the behaviour and characteristic of the radio waves propagation. The more the actual capabilities and limitations of this tool are acquainted, the easier and more effective the interpretation of the collected signal will be.

This tool works by emitting and receiving short electromagnetic (EM) impulses in a given bandwidth [20]. In practical terms, the dielectric contrasts within the investigated media generate a partial reflection of the EM waves. The analysis of the reflected signal and its related delay time, allows a basic interpretation of the subsurface features [21].

Since the major goal of this work is to deal with practical applications, the focus will not be to concentrate on advanced theoretical insights. For a comprehensive dissertation about the Maxwell's equations and constitutive relationships, it is possible to refer to [22] and [23]. The behaviour of the EM waves traveling through a medium depends on both the signal frequency and the dielectric properties of the material [21]. The constitutive equations, hypothesizing linear, isotropic, non dispersive, homogeneous and stationary material, account for the physical properties of the medium, namely,

$$D = \varepsilon \mathbf{E} \tag{1.1a}$$

$$B = \mu \mathbf{H} \tag{1.1b}$$

$$J = \sigma \mathbf{E} \tag{1.1c}$$

where D and B are respectively the electric and magnetic fields intensity; J is the current density, E and H are the electric and magnetic field, and with σ, ε and μ being the electrical conductivity, the dielectric permittivity and the magnetic permeability, respectively.

The complex variable $\sigma = \sigma' + i\sigma''[\mathrm{S\,m^{-1}}]$ influences the generation of electric current (charge movements) in presence of an electric field. The higher is the resistance the electric current, the more the EM signal will exert dissipation. On the contrary, the parameter $\varepsilon = \varepsilon' + i\varepsilon''[\mathrm{F\,m^{-1}}]$ describes the displacement of charges due to the electric currents. The more are the displacements, the more energy is stored by the medium. This turns out to provide a which reflects in a slower wave velocity. The two parameter are related as follows [24]:

$$\varepsilon'' = \frac{\sigma}{\varepsilon_0 \omega} \qquad (1.2)$$

with $\varepsilon_0 = 8.85 * 10^{-12}[\mathrm{F\,m^{-1}}]$ being the dielectric permittivity of the vacuum. Finally, μ does not need to be considered as complex, and defines the rate of intrinsic atomic and molecular moments responding to an acting magnetic field. In practical terms, ε and σ greatly influence the EM behaviour of the travelling wave, by affecting its velocity and attenuation, respectively, whilst μ was found to be equal to free space magnetic permeability, μ_0, for all the non-magnetic materials, and does not affect the propagating wave.

Usually, GPR data are visualised in the time domain on a diagram having with the time delay in the x axis and the amplitude in the y axis. However, for sake of mathematical simplicity, theoretical formulations are instead expressed in the frequency domain, by applying a Fourier Transform[21]. As an instance, convolving time-domain signals is equivalent to multiplying their Fourier transforms in frequency domain. Thus, what appears to be a complicated operation in time, is simple if viewed in terms of frequency.

1.1.2 EM wave propagation

Let us consider the EM wave propagation as a one-dimensional wave equation, expressed in Eq. 1.3. In Fig. 1.1, the wave propagation observed along the z axis (time) is shown, with electric (E) and magnetic (H) fields on the perpendicular axes.

$$\frac{\partial^2 E}{\partial z^2} = \mu\varepsilon\frac{\partial^2 E}{\partial t^2} \qquad (1.3)$$

When referring to a perfect dielectric EM wave propagation, as in Fig. 1.1, it
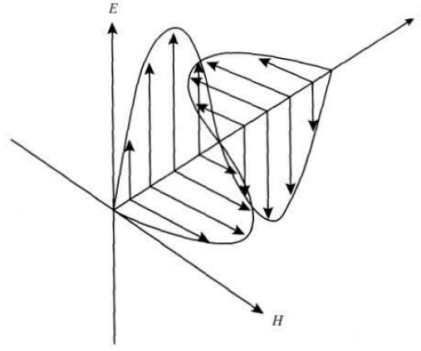
Figure 1.1: Propagation of electromagnetic waves in free space [20]

is possible to describe the behaviour of the electric field $E(z)$ against the positive propagating direction z, as:

$$E(z) = E_0 e^{-ikz} \tag{1.4}$$

with

$$\kappa = \frac{\omega}{\nu}, \tag{1.5}$$

being the wave number $[\text{m}^{-1}]$, and

$$\nu = \frac{c_0}{\sqrt{\varepsilon_r}}, \tag{1.6}$$

being the wave velocity [ns/cm]. Still, c_0 is the speed of wave in the void, and

$$\varepsilon_r = \frac{\varepsilon'}{\varepsilon_0} \tag{1.7}$$

is generally referred to as relative dielectric permittivity or dielectric constant.

EM signals propagating through dispersive media inevitably undergo electrical losses, to both the electric (E) and magnetic (H) fields [20][21]. This causes an attenuation of the received electromagnetic wave. In fact, considering Eq. 1.6 it is evident that κ is a complex number as well, expressed as:

$$\kappa = \alpha + i\beta \tag{1.8}$$

It is possible now to rewrite Eq. 1.4, as:

$$E(z) = E_0 e^{-\alpha z} + E_0 e^{-i\beta z} \tag{1.9}$$

The first term represents the dissipation of the plane wave through the lossy

medium. The attenuation rate is defined by $\alpha[\mathrm{dB\,m^{-1}}]$, named attenuation constant, Eq. 1.10a. On the other hand, the second term describes the wave propagation, with the phase being controlled by the phase constant $\beta[\mathrm{m\,s^{-1}}]$, Eq. 1.10b.

$$\alpha = \omega \sqrt{\left[\frac{\mu\varepsilon'}{2}\sqrt{1 + \left(\frac{\varepsilon''}{\varepsilon'}\right)^2} + 1\right]} \tag{1.10a}$$

$$\beta = \omega \sqrt{\left[\frac{\mu\varepsilon'}{2}\sqrt{1 + \left(\frac{\varepsilon''}{\varepsilon'}\right)^2} - 1\right]} \tag{1.10b}$$

By looking at Eq.1.2 and Eq.1.10a it is evident that the attenuation constant α depends on both the conductive and the dielectric properties of the medium. Values of attenuation constants and relative dielectric permittivity for most common materials are given in [20] and [25].

As the propagation velocity is given, it is possible to infer the depth of a reflector immersed in a homogenous medium, by looking at the time Δt [s] between the emission and the reception of a pulse. Considering a monostatic configuration of the GPR, i.e. a system having transmitter and receiver at the same physical position, the depth h [m] can be calculated as follows:

$$h = \frac{\nu\Delta t}{2} \tag{1.11}$$

The delay Δt is referred to as the travel time. In a monostatic configuration, it includes the time necessary for the wave to hit the reflector, and for the way back, which explains why it is divided by 2 in Eq. 1.11.

Signal reflections occur anytime an inhomogeneity in dielectric properties, i.e. change in ε_r, is encountered. Such an occurrence, as aforementioned, determines a reflection of portion of the propagating energy, and the transmission of the remaining beyond.

1.1.3   Main GPR configurations

The application of GPR in highway engineering is mostly related to the use of impulse radar systems, due to a major easiness of usage and data interpretation. These systems operate by transmitting toward the target a very short pulse ($\sim 10^9$ [s]), characterized by a fixed central frequency. This is done by means of

one or more antennas, and by recording the signal that is back-reflected by the dielectric discontinuities. The two-way travel time signal is then recorded in the timedomain, and a map of reflections generated in the sub-surface can be finally displayed.

Conversely, stepped-frequency continuous-wave (SFCW) radar systems operate in the frequency domain. Amplitude and phase of the emitted and received signal are sampled and collected as a function of the frequency, which is linearly incremented of a fixed step within a defined frequency range. The high costs of the electronics, a major complexity in data processing and the lack of dedicated commercial software have broadly resulted in a lower spread of SFWC radars in highway and railway engineering, although their use has recently increased [26].

Concerning the configurations of the antennas, a GPR system is configured as mono-static when a unique antenna operates as both transmitter and receiver. Conversely, the GPR system is defined as bi-static in the case of separated transmitter and receiver. Furthermore, GPR systems can be sorted in ground-coupled and air-coupled systems according to the type of antenna. In the first case, the antenna is in direct contact with the ground. This allows higher depths of penetration throughout the medium. Usually, central frequencies available for this configuration range from 80 [MHz] to 1500 [MHz]. In the second survey configuration, the antenna is typically kept at a constant height above the surface, mostly ranging from 0.15 [m] to 0.50 [m]. Most common air-coupled GPR systems are pulsed systems operating in the range 0.5÷2.5 [GHz], with a central frequency typically of 1 [GHz]. The penetration depth of an air-coupled system is dependent on the central frequency and rarely exceeds 0.9 [m] for road pavement and railway track-bed applications [27]. Despite this main drawback, air-coupled systems allow to survey at traffic speed by mounting the system onto an instrumented vehicle [28]. The advantage of avoiding traffic interruption makes the air-couple GPR systems the most common devices used in transport infrastructure surveys.

1.1.4 GPR signal imaging

There are a multitude of ways for displaying a GPR response, as shown in Fig. 1.2. In general, it is possible to represent the signal collected as:

$$f(x, y, z) = A(x_i, y_j, z_k) \tag{1.12}$$

with i, j and k ranging from 1 to N, M, P, respectively.

A single radar trace, or waveform, is called A-scan (Fig. 1.2a), and it can be defined as:
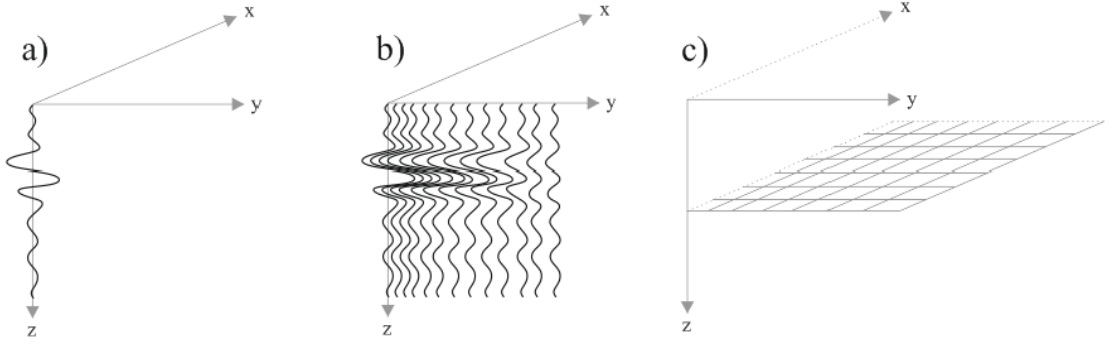
Figure 1.2: Visualization modes of a GPR signal: (a) A-scan, (b) B-scan, and (c) C-scan

$$f(z) = A(x_i, y_j, z_k) \tag{1.13}$$

with k ranging from 1 to P, i and j equal to a constant value. The A-scan provides a punctual information about the subsurface configuration. It should be noticed how the z-axis can represent both time and depth, which are related by the propagation velocity.

A set of consecutive radar waveforms along a particular direction (x, for instance) represents a B-scan (Fig. 1.2b), and it can be defined as follows

$$f(x, z) = A(x_i, y_j, z_k) \tag{1.14}$$

with i and k ranging from 1 to N and P, respectively, and j being a constant value. Therefore, a B-scan visualization mode allows to achieve a two dimensional view along a specific direction. In highway and railway engineering applications, B-scan is a widely used imaging methodology, wherewith the variations occurring on the main geometrical features of the substructures, such as the thickness of the layers, can be relatively easily checked.

If a value along the z-axis is set as constant, the visualization of the horizontal domain (x, y) is called C-scan (Fig. 1.2c), and it is defined as follows:

$$f(x, y, z) = A(x_i, y_j, z_k) \tag{1.15}$$

over the range $i = 1$ to N, $j = 1$ to M and $k = $ constant. Practically, the C-scan view mode provides an amplitude map at a specific time of collection. When one area is surveyed, for instance by collecting data along a regular grid, the C-scan visualization mode can be very useful in detecting inhomogeneous spots, which are characterized by a high reflectivity in terms of signal amplitudes.

In general, the GPR data are processed and depicted according to the above three visualization modes. Since the A-scan mode provides information about the temporal delay between the emission and the reception of a single transmitted or back-reflected signal, the processing of the single A-scan operates exclusively in the punctual spatial domain influencing that signal. When a set of consecutive waveforms is considered, such temporal frames are gradually set beside along a linear track. Therefore, the processing of a B-scan operates in both temporal (i.e., in depth along the z axis) and spatial (i.e., along the path of scan, namely, the x axis) dimensions. The C-scan visualization concerns a defined temporal instant, such that the processing operates only in space. Due to the considerable extension of the investigated infrastructures and the resultant huge amount of data processing required, the C-scan visualization mode is rarely adopted in road applications.

1.2 Theory of elasticity

Performance-based mechanical assessment tools are fundamental means of calibration and validation to develop reliable failure prediction models. Regardless of their pratical functioning principles, they mostly exploit the so-called Analytical-Empirical or Mechanistic-Empirical method to predict the mechanical response of a superstructure.

This method, particularly developed for application purposes in road pavements and bearing soils, combines the major physical properties of the investigated materials and a theoretical model in order to predict stresses, strains and deflections exerted in a medium by an external load. If the hypotheses about the material properties and boundary conditions are correct, this method is assumed as reliable for the prediction of the mechanical response of the structure for any combination of load, climatic conditions and construction materials.

The theoretical outcome is then combined with the empirical relationships derived from the behaviour of pavements, in order to infer a performance-based prediction of the superstructure response. For instance, the occurrence of asphalt cracking is related to the exceedance of the limit tensile strain within the asphalt concrete layer, or the permanent deformations are expected if the maximum compressive strain is overcome (Fig. 1.3).

In this section, a brief overview of the theory of elasticity, likely the most used in pavement design, is given. This theory generally assumes continuous deformations, homogeonous, isotropic and linear elastic materials.
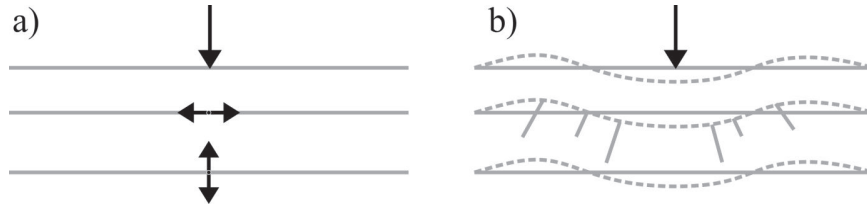
Figure 1.3: Mechanical response (a) and performance (b) of a pavement exerted by a load
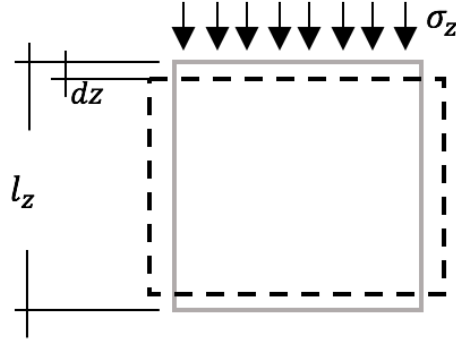
Figure 1.4: Uniaxial stress of a cube of homogenous, isotropic and linear elastic material

1.2.1 Elastic parameters

Let us consider a discrete cube of material. As a uniform uniaxial stress in the vertical direction σ_z is applied, it will return a deformation, and a subsequent change of the length of its sides, as shown in Fig. 1.4.

Elastic parameters are constitued by the vertical strain ε_z and the Poisson coefficient ν, defined as follows:

$$\varepsilon_z = \frac{dz}{l_z} \tag{1.16a}$$

$$E = \frac{\sigma_z}{\varepsilon_z} \tag{1.16b}$$

$$\nu = -\frac{\varepsilon_x}{\varepsilon_z} \tag{1.16c}$$

Since, by hypothesis, the material is linear elastic, the Hook's law can apply. Accordingly, the ratio between the vertical stress σ_z and the vertical strain ε_z is equal to the elasticity coefficient, or Young's Modulus E. Moreover, the ratio of horizontal strain ε_x and vertical strain ε_z is a negative constant, whose modulus is called Poisson's ratio. According to above, a stress applied along a particular direction is expected to generate a perpendicular strain proportional to $-\nu/E$.

As shear stresses $\tau_{xz} = \tau_{zx}$ are considered, a strain $\gamma_{xz} = \gamma_{zx}$ is expected. By imposing the same starting hypotheses than above, the constant shear modulus G is expressed as:

$$G = \frac{\tau_{xz}}{\gamma_{xz}} \tag{1.17}$$

For a three-dimensional loading of the same isotropic material, the Hook's law can be expressed as follows:

$$\varepsilon_x = \frac{\sigma_x}{E} + \frac{-\nu\sigma_y}{E} + \frac{-\nu\sigma_z}{E} \tag{1.18}$$

The plane stress case is particularly useful for assessing stresses and strains in a continuum. Much of the following refers to [29].

When referring to an isotropic, linear elastic materials, the theory assumes the following three hypotheses, leading to the three equations expressed by Eq. 1.19:

1. Equilibrium

2. Continuity between normal and shear strains

3. Hook's law

$$\frac{\partial\sigma_x}{\partial x} + \frac{\partial\tau_{xy}}{\partial y} = 0 \tag{1.19a}$$

$$\frac{\partial\tau_{yx}}{\partial x} + \frac{\partial\sigma_y}{\partial y} = 0 \tag{1.19b}$$

$$\tau_{xz} = \tau_{zx} \tag{1.19c}$$

It is worth noting that, according to Eq. 1.19, static loads and weightless material are also assumed.

From the hypotesis of continuity between normal and shear, Eq. 1.19b, derives:

$$\frac{\partial^2\varphi_{xy}}{\partial x\partial y} = \frac{\partial^2\varepsilon_x}{\partial^2 y} + \frac{\partial^2\varepsilon_y}{\partial^2 x} \tag{1.20}$$

with φ being the angular shear strain.

Hook's law can be finally rewritten for plane stresses, as:

$$\varepsilon_x = \frac{1}{E}\left[\sigma_x - \nu\sigma_y\right] \tag{1.21a}$$

$$\varepsilon_y = \frac{1}{E}\left[\sigma_y - \nu\sigma_x\right] \tag{1.21b}$$

$$\varphi_{xy} = \frac{2(1+\nu)}{E}\tau_{xy} \tag{1.21c}$$

The introduction of a stress function ϕ allows to express the stresses through the following differentials equations satisfying the equilibrium conditions:

$$\sigma_x = \frac{\partial^2 \phi}{\partial^2 y} \tag{1.22a}$$

$$\sigma_y = \frac{\partial^2 \phi}{\partial^2 x} \tag{1.22b}$$

$$\sigma_z = \frac{\partial^2 \phi}{\partial x \partial y} \tag{1.22c}$$

It is now possible to replace the stresses in Eq. 1.22 into Eq. 1.20, so obtaining:

$$\nabla^2\nabla^2\phi = 0 \tag{1.23}$$

The solutions to this equation are retrieved through the boundary conditions, by separating the variables of the second order differential equation.

1.2.2 Boussinesq's equations

The solutions proposed by Boussinesq (1885) for quantifying stresses, strains and displacements in a homogenous, isotropic, linear elastic, semi-infinite space, with Young's Modulus E and Poisson's ratio ν, are at the base of most of the modern mechanistic-empirical methods.

As far as transport infrastructures are considered, most interesting closed solution to the problem is represented by the center line of a uniformely distributed circular load, as shown in Fig. 1.5.
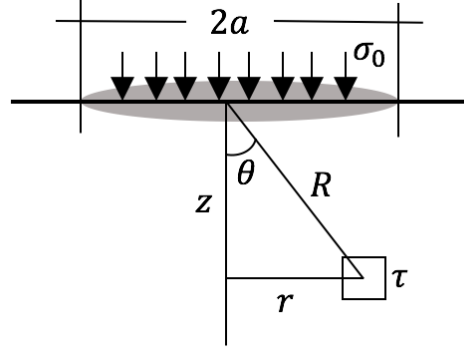
Figure 1.5: Bousinessq's equation notation for a circular load, in polar coordinates

$$\sigma_z = \sigma_0 \left[1 - \frac{1}{\left(\sqrt{1 + (a/z)^2} \right)^3} \right] \quad (1.24\text{a})$$

$$\sigma_r = \sigma_t = \sigma_0 \left[\frac{1 + 2\nu}{2} - \frac{1 + \nu}{\sqrt{1 + (a/z)^2}} + \frac{1}{2 \left(\sqrt{1 + (a/z)^2} \right)^3} \right] \quad (1.24\text{b})$$

$$\varepsilon_z = \frac{(1 + \nu)\sigma_0}{E} \left[\frac{(z/a)}{\left(\sqrt{1 + (z/a)^2} \right)^3} - (1 - 2\nu) \left(\frac{(z/a)}{\sqrt{1 + (z/a)^2}} - 1 \right) \right] \quad (1.24\text{c})$$

$$d_z = \frac{(1 + \nu)\sigma_0 a}{E} \left[\frac{1}{\sqrt{1 + (z/a)}} + (1 + 2\nu) \left(\sqrt{1 + (z/a)} - (z/a) \right) \right] \quad (1.24\text{d})$$

with d_z being the deflection under the load.

Closed solution for the case of a load transferred via a uniformly loaded circular rigid plate is also given by Boussinesq. This specific case is particularly relevant as most of the common NDTs for the mechanical characterisation of layered media relies on the application of a load onto a circular metal plate, as shown in Fig. 1.6. In such conditions, the following solutions are required:

$$\sigma_z = \frac{\sigma_0}{2} \left[\frac{1 + 3(z/a)^2}{(1 + (z/a)^2)^2} \right] \quad (1.25\text{a})$$

$$\varepsilon_z = \frac{(1 + \nu)\sigma_0}{2E} \left[\frac{2(1 - \nu)}{1 + (z/a)^2} - \frac{1 - (z/a)^2}{(1 + (z/a)^2)^2} \right] \quad (1.25\text{b})$$

$$d_z = \frac{(1 + \nu)\sigma_0 a}{2E} \left[(1 - \nu)(\pi - 2\arctan(z/a)) + \frac{(z/a)}{1 + (z/a)^2} \right] \quad (1.25\text{c})$$
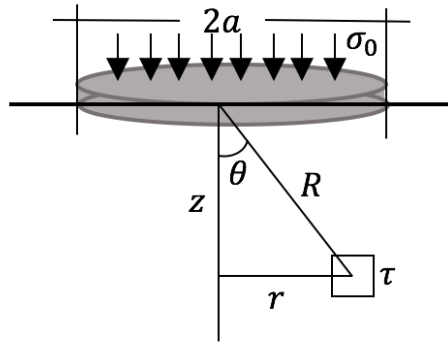
Figure 1.6: Load onto a circular metal plate
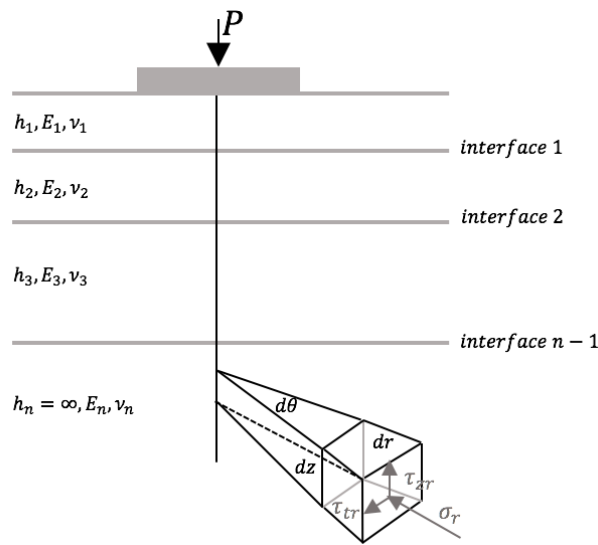
Figure 1.7: Generalised multi-layer elastic system

1.2.3   Multi-layered structures

In Fig. 1.7 a typical scheme of a multi-layered elastic system is represented. A full set of simplifying assumptions are herein accounted for, namely, (i) the materials composing the different layers are homogeneous; (ii) the thickness of each layers, with the exception of the subgrade, are finite, whereas the later extension is infinite; (iii) the materials are isotropic; (iv) a full friction at the interfaces is considered; (v) there are no tangential forces acting at the surface and (vi) the solution to problem is influenced by E and ν of each layer. Note that, to date, constraints (iv) and (v) can be overcome through the use of computerised multilayered software packages.

For any element within any layer in the system above, a particular orientation can be identified such that the tangential stresses acting on the element are null. In this condition, the normal strains referred to as principal, are calculated as
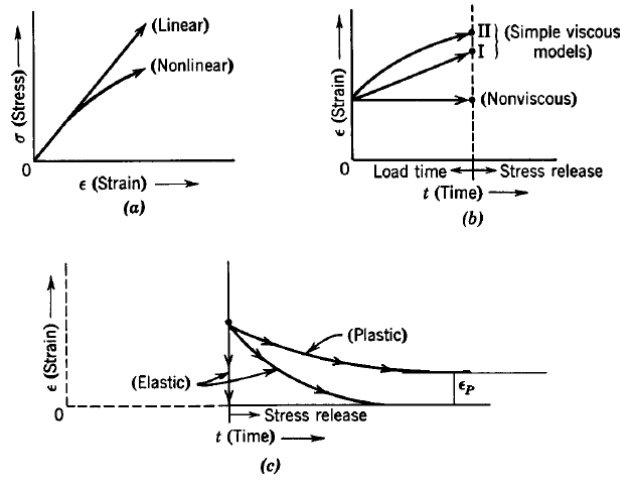
Figure 1.8: Material characteristics: (a) linearity; (b) viscous effects, (c) plastic effects [30]

follows:

$$\varepsilon_z = \frac{1}{E}[\sigma_z - \nu(\sigma_r + \sigma_t)] \tag{1.26a}$$

$$\varepsilon_r = \frac{1}{E}[\sigma_r - \nu(\sigma_t + \sigma_z)] \tag{1.26b}$$

$$\varepsilon_t = \frac{1}{E}[\sigma_t - \nu(\sigma_r + \sigma_z)] \tag{1.26c}$$

Depending on the mechanical response of the material, different theories are accounted for. This response relies on the linearity of strains, the viscous effects, and the recoverable effects (plasticity) of the material, which are shown in Fig. 1.8. Due to characteristic of the material, different models have been developed to represent effectively its behaviour when a load is exterted.

In regard to the road pavements, the composing material are generally nonlinear and characterised by viscoplastic responses. However, for limited stress rates, the use of a linear model most often provides satisfying results [30]. Accordingly, the most widely used theory is still the multi-layered linear elastic model.

One-layer solution

Fig. 1.9 shows a typical linear elastic one-layer system, with infinite thickness, Young's Modulus E_1 and Poisson's ratio ν_1. Considering a homogenous, isotropic, elastic medium, the vertical stress can be calculated with reference to a uniformly distributed circular load, by using the Boussinesq's relationship expressed in Eq.
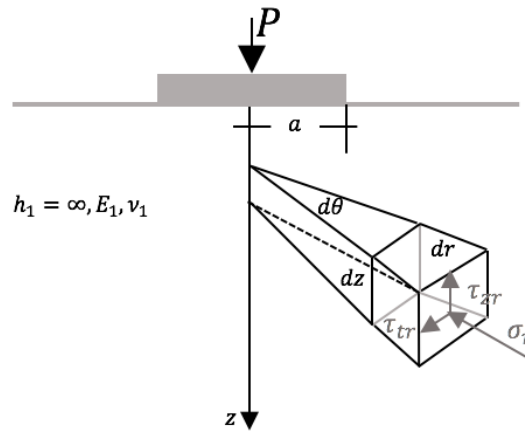
Figure 1.9: One-layer system stress condition

1.24 and 1.25.

More recent studies have focused on expanding the Boussinesq's solutions for different load conditions, better representing the typical case of a tire-pavement contact. In more detail, *Forster and Ulery* [31] proposed a number of charts to define the vertical and horizontal stresses and strains for semi-infinite elastic masses due to circular loaded plates, for different values of ν. These solutions rely on parametric functions, depending on the depth and offset distances in radii (z/a and r/a). The values of the parameters ($A, \ldots, H$) are determined, and provided through tables.

One-layer models are mostly applicable with success in the case of granular base/ subbase superstructures with just a thin asphalt covering layer.

Multi-layer solution

In order to reduce stresses and deflections at the subgrade interface, the trasportation infrastructures are mostly composed of a multi-layered system, having moduli of elasticity decreasing with the depth.

With regards to the two-layered systems, the solutions to the problem are given by *Burmister* in [32], under the assumption of a continuous contact at the surface between the two layers, and absence of any normal or shear stress on the surface, with the exception of the investigated loaded area. Values of stresses and deflections are presented with regards to the ratio between the Young's moduli of the layers E_1/E_2.

Fig. 1.10 shows the rate of vertical pressure perceived at the depth z, σ_z/p, as the depth z and distance a vary, with respect to the Young's moduli ratio. The influence of a higher-strength covering layer is clearly visible. Indeed, in the
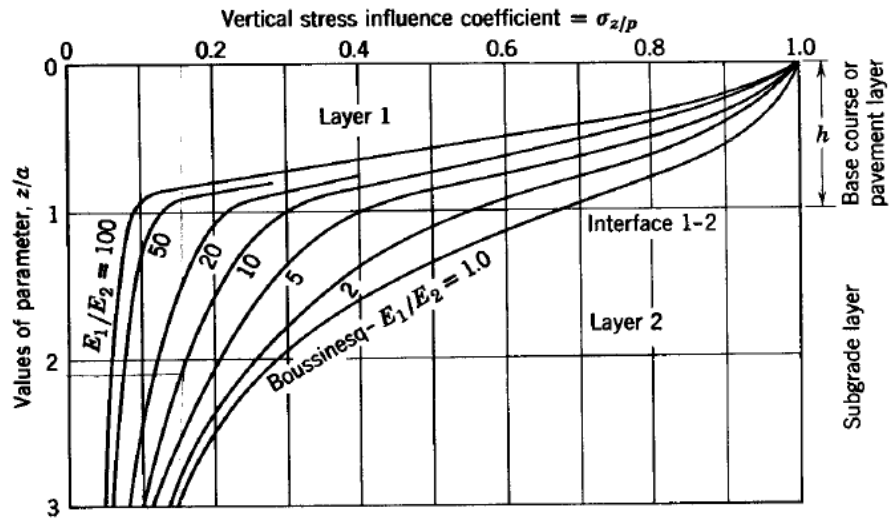
Figure 1.10: Basic patterns of Burmister's two-layer stress influence curves [33]

case of a homogeneous material ($E_1/E_2 = 1$) the vertical stresses at the layers interface are approximatively the 70% of the applied pressure, whereas on the opposite, when $E_1/E_2 = 100$ they result reduced to around 10%.

This fact involves a further consideration. Although for greater depths (e.g. $z/a = 3$) similar stresses are obtained for different E_1/E_2 ratios, the stress gradient at the interface depth ($z/a = 1$) highlights the importance of the quality and thickness of the base course in determining the general resistance to the deformation of the whole system.

The total deflection Δ calculated at the surface, in case of loaded circular plate, can be calculated by the following equations:

$$\Delta = 1.5 \cdot \frac{pa}{E_2} \cdot F_2, \text{ flexible plate} \tag{1.27a}$$

$$\Delta = 1.18 \cdot \frac{pa}{E_2} \cdot F_2, \text{ rigid plate} \tag{1.27b}$$

where p is the unit load on the plate with radius a, E_2 is the Young's Modulus of subgrade and F_2 a dimensionless deflection factor (see Fig 1.11) depending on both the E_1/E_2 and z/a ratios. The value of Δ for any specific depth has been calculated and presented by charts in [34], by extending the Burmister's theory, under the assumption of $\nu = 0.5$.

The tabular summary of stresses value for three-layer systems, simplified as shown in Fig. 1.12, were firstly given by Fox [35], and then extended to a wider range of parameters in [36] and [37]. The graphical and tabular solutions provided
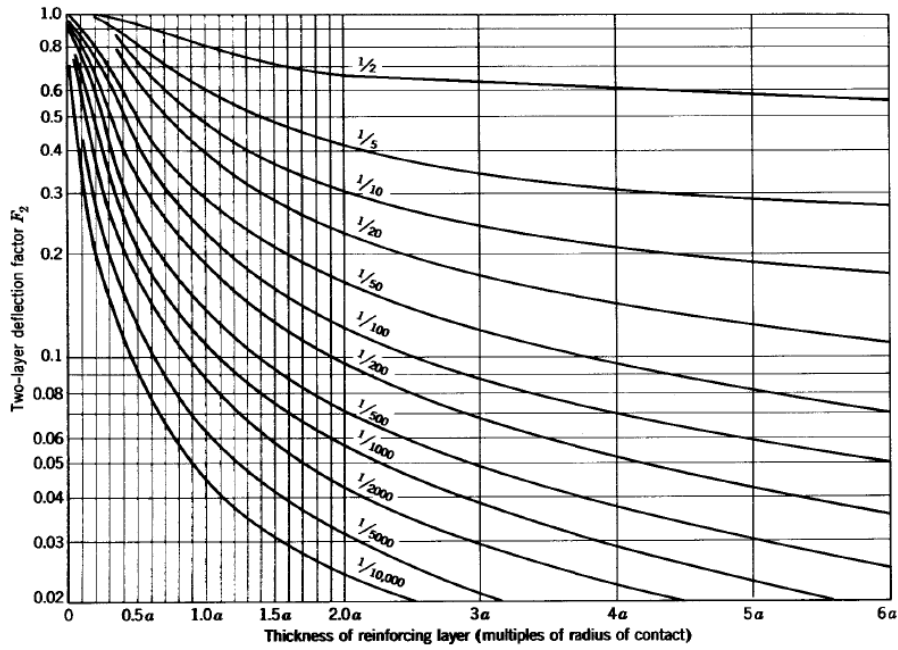
Figure 1.11: Influence values for a two-layer system [32]

by these studies are based on the use of the following parameters: $\kappa_1 = E_1/E_2$, $\kappa_2 = E_2/E_3$, $A = E_1/a/h_2$, $H = h_1/h_2$.

The Odemark's method

Odemark's method [38] allows to calculate stresses and strains within a layered elastic system by a very fast algorithm. This method relies on the assumption that the mechanical response observed below a layer mostly depends on the stiffness of the particular concerning layer. Accordingly, as the thickness, modulus and Poisson's ratio of the layer change, then stresses and strains below the layer keep
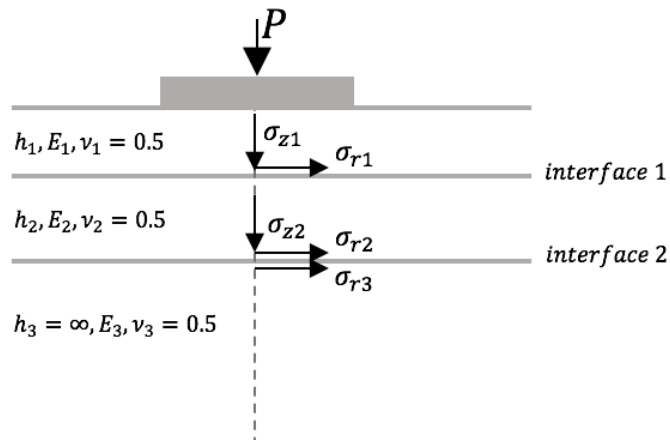
Figure 1.12: Schematisation of a three-layer elastic system [32]

Figure 1.13: Odemark's equivalent thickness method

being the same, as long as the overall stiffness remains approximativelty constant. Hence, since the stiffness of a layer with thickness h is proportional to:

$$\eta = \frac{h^3 E}{1 - \nu^2}, \tag{1.28}$$

a variation of h ,E and ν, that not involves a change of η, does not influence the mechanical response of the layer. It is then possible to consider the two-layer system in Fig. 1.13, and theoretically to produce an equivalent system, where the first layer has the same modulus and Poisson's ratio than the layer below, and a thickness such that the overall stiffness remains unchanged ($\eta_1 = \eta_2$). This is analytically expressed by Eq. 1.29.

$$\frac{h_1^3 E_1}{1 - \nu_1^2} = \frac{h_e^3 E_2}{1 - \nu_2^2} \tag{1.29a}$$

$$h_e = h_1 \sqrt[3]{\frac{E_1}{E_2} \cdot \frac{1 - \nu_2^2}{1 - \nu_1^2}} \tag{1.29b}$$

where h_e is referred to as "equivalent" thickness, which gives the name to the whole method (Method of the Equivalent Thickness - MET). In order to reduce the uncertainties derived from the simplifying assumption at the base of the MET, a corrective factor f is considered. Furtherly, if ν is assumed as constant for all layers, Eq. 1.29b becomes:

$$h_e = f \cdot h_1 \sqrt[3]{\frac{E_1}{E_2}} \tag{1.30}$$

with f equal to 0.8 generally returning good agreement with the theory of elasticity for all the interfaces but the first one, for which a value of 0.9 or 1.0 is considered for a two-layer system and a multi-layer system, respectively.

With regard to a typical multi-layer system, the equivalent thickness of the upper $n - 1$ layers with respect to the reference layer n, is:
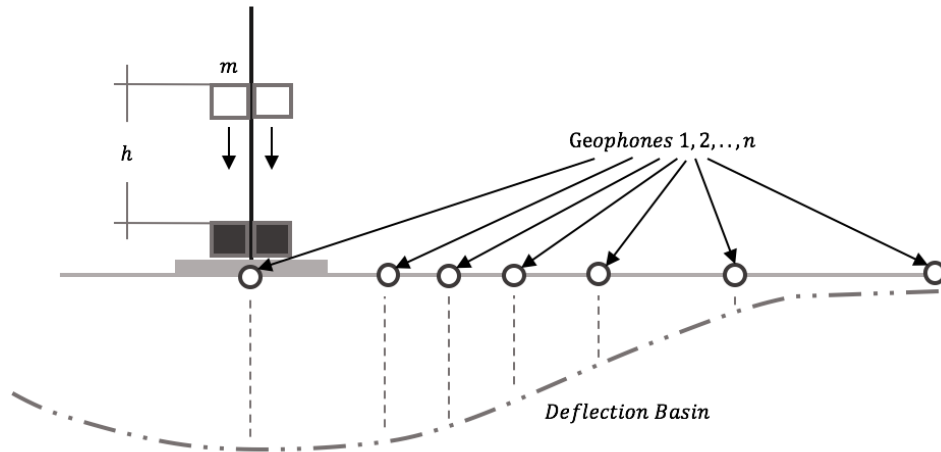
Figure 1.14: Functioning principles of FWD

$$h_{e,i} = f \cdot \sum_{i=1}^{n-1} h_i \sqrt[3]{\frac{E_i}{E_n}} \tag{1.31}$$

1.2.4 NDTs for mechanical assessments

The non-destructive structural assessment of highways' superstructures is a crucial stage in a pavement management process. The direct measurement of the pavement surface deflections under a load is typically used for these purposes. The analysis of these deflection data allows for the evaluation of the structural response of a superstructure.

Falling Weight Deflectometer (FWD)

The Falling Weight Deflectometer (FWD) [39] is a NDT device used to produce transient impulse forces by applying a load onto a surface, through a circular metal-made loading plate. This impulse force, measured by a load cell onto loading plate, determines a relevant deflection of the structure. This deflection, illustrated in Fig. 1.14, is measured by specific geophones, i.e. seismic deflection transducers, placed at fixed distances from the plate to observe the deflection basin.

FWD has progressively replaced Benkelmann's Beam as in situ survey device over the years. This is due to a higher suitability for extensive surveying. Indeed, it can be towed by a medium-sized or, better, a truck-type vehicle.

Synthesizing the functioning principles of FWD, it basically works by dropping a fixed weight from a known height onto rubber buffers connected to a metal

plate, at contact with the surveyed surface. The impact peak force P, can be determined by the following relationship:

$$P = \sqrt{2 \cdot g \cdot h \cdot m \cdot k} \tag{1.32}$$

with g being the acceleration of gravity, h the height of drop of the mass m and k the spring constant of the buffers.

The aforementioned theoretical framework is used into a number of current design methods. This is performed to retrieve the elastic modulus of the layers composing the superstructure from the analyses of the deflections collected by FWD. Note that such an approach would always return in a value which holds in memory a number of simplifications and approximations from the linear elastic theory. Accordingly, what is generally indicated as "elastic modulus" should be clear to be rather an apparent modulus or effective stiffness. This is due to the actual plastic, viscous, viscoelastic and/or viscoplastic behaviour of most of the bearing layers under loads.

The determination of the elastic modulus E of each layer from the FWD-calculated deflection basin is generally referred to as "back-calculation" or "back-analysis" [40] [41]. In this iterative process, a starting value of elastic modulus for each layer is assumed. Then, the deflection in the hypotesized scenario theoretically are calculated and compared with the observed ones. The values of E are then updated according to results, up to the maximisation of the agreement between the observed and the modelled deflections.

Light Falling Weight Deflectometer (LFWD)

The light falling weight deflectometer (LFWD or LWD) [42] is a portable version of FWD, capable to overcome potential issues with the accessibility of test sites, that are often encountered with more cumbersome equipment [43]. Several studies analysed the influence domain of the deflections exerted by LFWD [44][45] in various types of subgrade soils under different test conditions. From an application's point of view, high potential was found for LFWD-based models, especially in unbound subgrade soils.

As a small-sized FWD device, LFWD relies on the same working principle. Indeed, a portable circular metal plate is loaded by a load hammer. The geophones in contact with the surveyed surface allow to measure the deflections caused by the impulsive force. Since the deflection basin, according to the lower applied load, holds a limited influence in depth, for thick covering layers it is possible to use a Boussinesq-type model as per a homogeneous medium, for calculating an

Figure 1.15: Typical configurations of a) FWD and b) LFWD

equivalent modulus, as follows:

$$E = \frac{k(1 - \nu^2)\sigma \cdot R}{\delta_c} \tag{1.33}$$

Chapter 2

Road Applications

2.1 Background

2.1.1 Flexible pavements assessment

Although the fields of applications for non-destructive methods in road main-
tenance are various, in this study the focus has been set onto the evaluation
of flexible pavements, due to their wide diffusion as a construction methodol-
ogy worldwide, and to the large scientific and professional relevant contributions,
which make a clear view of the state of the art of high-productivity and non-
destructive flexible pavements surveying.

Generally speaking, a flexible road pavement is a multi-layer structure com-
posed of hot-mixed asphalt (HMA) bitumen-bound layers overlaying unbound
granular courses, which in turn lay on a bearing subgrade. A scheme of a typical
flexible plavement configuration is shown in Fig. 2.1. The need for binding the
shallower layers is due to the high horizontal strain imposed by the vehicles at the
wheel-surface contact. Conversely, the unbound granular layers, typically com-
posed of a subbase and the subgrade, stand for the major structural contribute,
and grant the proper resistance to the vertical stresses.

The bearing capacity of subgrade soils can be assessed by tests carried out
in-situ [46][47] and in the laboratory environment [48], which mainly evaluate the
deformation induced by the pavement when a fixed stress is applied. Due to the
high time and costs required for running the tests, these can be performed only
at few and discrete points along the road path, and provide partial knowledge
of the bearing capacity of the road pavement. Furthermore, it is important to
emphasize on the invasiveness of these techniques (i.e., they require destructive
testing of the soil) and the interference with the traffic flow, which may have

HMA/AC surface course
HMA/AC binder course
bond base course
loose subbase course
subgrade
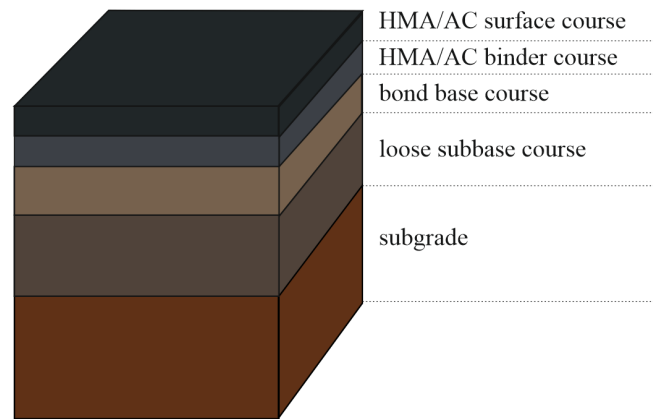
Figure 2.1: Typical configurations of a flexible pavement

impact on the driving safety of roads.

In view of the above limitations, as mentioned in Chap. 1, NDT techniques such as the FWD and LFWD, which provide reliable, non-invasive and high-efficiency surveys, have become popular for the assessment of the mechanical properties of the flexible pavements.

However, although the FWD can be mounted onto a vehicle, it cannot collect data while in motion. This reflects into a limited productivity as well as in the need for slowing down the traffic flow by partially or fully closing the road. Furthermore, the back-calculation process described in Sect. 1.2.4, which allows to infer the elastic moduli of the layers by observing the deflection basin generated by a FWD test, requires the prior knowledge of the thickness of each layer composing the pavement. Such an information is generally acquainted by means of on-site corings, which returns in a both extremely cost-expensive and discrete knowledge about the whole extension of the pavement.

2.1.2   NDTs integration

Accordingly, the possibility to use a non-destructive on-board technique for the real-time assessment of the bearing capacity of the roads at traffic speed, as an integration to FWD tests, could represent a real breakthrough in the field of highway engineering. The main benefit could be related to the possibility of collecting data efficiently and effectively in order to create fully comprehensive databases for integration in pavement management systems (PMS).

Amongst the numerous NDTs used in road surveys, GPR is nowadays well acknowledged as one of the most powerful and effective, due to its significant flexibility of usage and reliability of results. As described in Chap. 1, this tool

basically enables to retrieve information on the physical and geometrical properties of the subsurface, by means of short EM impulses in a given frequency band [49][50].

According to [50], GPR road applications can be broadly divided into four main categories, namely: 1) surveys used in new road projects; 2) surveys performed prior to designing the rehabilitation of existing roads; 3) surveys carried out as quality control or quality assurance (QC/QA) of existing roads; and 4) surveys carried out for implementing pavement management systems.

The propagation speed and the attenuation of the GPR signal are mainly related to the relative dielectric permittivity ε_r and the electrical conductivity σ, which are highly sensitive to the presence of air and water. Accordingly, the content of air and water filling the inner voids of bounded and unbounded granular layers, highly affects the dielectrics of materials embedded in flexible pavements. To this effect, it is reasonable assuming that the density of the construction materials, highly influenced by the content of inner voids, is a key parameter affecting the whole EM behaviour of the layers [20].

On the other hand, as far as load bearing layers and subgrade soils are concerned, the compaction rate of the soil particles largely depends on their grain size distribution. In turn, this also affects the number of contacts between the grains and the overall shear strength of the material [51]. In view of the above, a compaction procedure is typically performed after the laying of the granular soil materials in order to activate resistive mechanisms and reach the highest bearing capacity.

Another occurrence capable of influencing both the mechanical and EM behaviour of a road pavement, is the presence of clay rising from the natural subgrade up to the voids within the bearing layers, namely base and subbase. Indeed, clay particles are well known to drammatically reduce the mechanical performances of a granular material, by penetrating between the solid grains and limiting the shear angle, particularly in wet conditions [52]. On the other hand. the effects of clay on the EM response of bearing materials have been thoroughly investigated by several researchers over years [53][54]. Undoubtely, the major effect of the clay on GPR signal is a significant attenuation of the EM waves amplitudes, by directly affecting the attenuation constant α, which describes the tendency of EM waves to get reduced in amplitude while traviling through a certain medium, and which is related to the propagation loss function L, as:

$$L = \exp\left(-\alpha z\right) \qquad (2.1)$$

with z being the depth. The coefficient α, described in Eq. 1.10a, is highly dependent on the overall conductivity of the material σ, which in turn is greatly affected by the presence of clay.

However, further EM effects induced by clay pollution have been reported by [55] and [56], which observed influences onto both the shape of back-received frequency spectra and the variation of material dielectrics with regards to the water content.

As a common practice in road engineering, GPR and FWD techniques are used separately for the assessment of the geometric (i.e., layer thicknesses) and the strength and deformation properties (i.e., deflection bowl) of the pavement, respectively. The integration of these information allows to evaluate the elastic moduli of the pavement layers. Combining the potential of these two techniques into a highly reliable technique capable to collect EM data at traffic speed and converting these into mechanical parameters of the road pavement may optimise their strength points.

2.2 Objective & methodologies

This project primarily aims at addressing a major challenge within the context of identification of early decay and loss of bearing capacity in flexible pavements by integrating GPR and other non-destructive testing equipment.

In particular, the objective of the study is to propose a preliminary-stage highly productive methodology capable of detecting low-strength spots over a road network by surveying the asset through air-launched GPR systems and by collecting ground-truth data through LFWD for calibration purposes.

2.3 Modelling

Such an integration of NDT techniques was previously investigated in a test site [60] composed of a two-lanes flexible pavement section, intensively investigated with both GPR and LFWD. Particularly, LFWD allowed collecting very deep mechanical data, hardly possible by less flexible technologies. In that case, a first prediction methodology based on the reflection amplitude at the interfaces between the layers, was developed. This study has taken this reference as a starting point for the development of a more stable and reliable technique.

As tackled in Sect. 1.2 it is possible to describe the behaviour of the stresses as
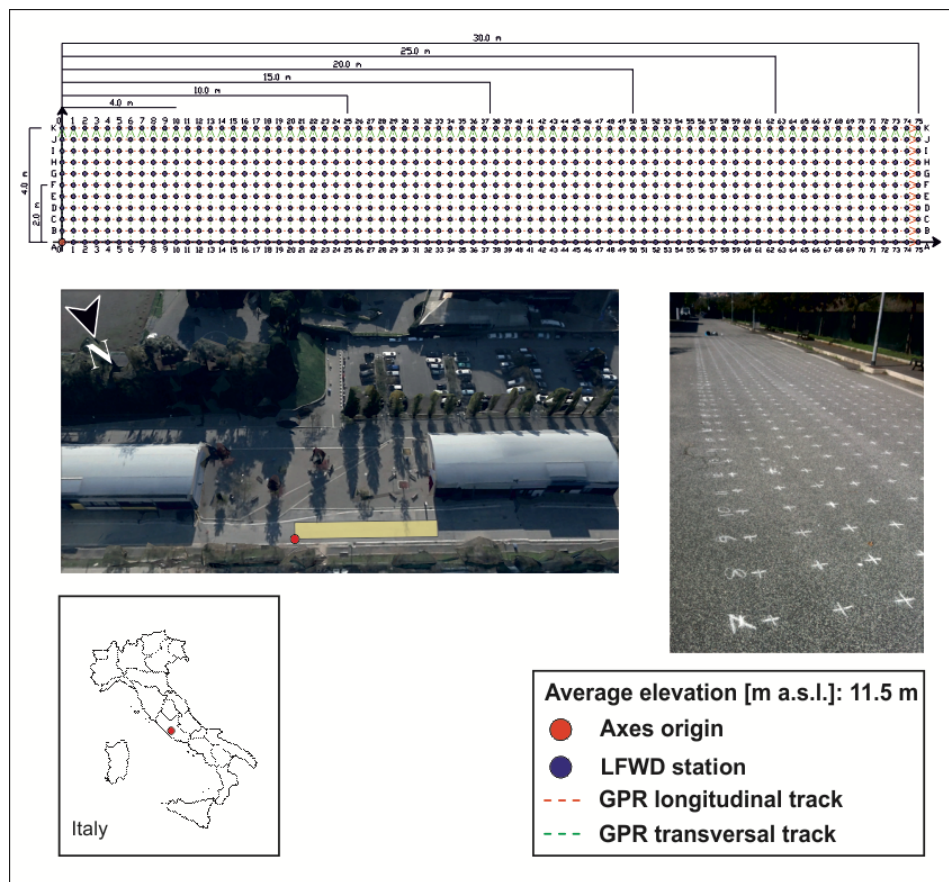
Figure 2.2: Test site for data acquisition along a 4 m x 30 m square regular grid mesh of 836 nodes [60]

the depth and the distance from the load vary, using the theory of Boussinesq and its generalization to multi-layer configurations [33][34]. In accordance with this theory, the graphical solutions proposed in [32] and shown in Fig. 1.10, clearly show that in case of homogeneous material ($E_1/E_2 = 1$) the vertical stresses at the layers interface are approximatively the 70% of the applied pressure, whereas on the opposite, when $E_1/E_2 = 100$ they result reduced to around 10%. This occurrence has been also demonstrated using numerical simulations [57].

Thereby, it can be argued that the loosely bound or unbound granular layers, and especially the base, may affect sensitively the mechanical behaviour of the pavement. To underpin the rationale of this thesis, it can be mentioned the research work made by Scullion and Saarenkeeto [50]. The authors have observed volumetric contractions caused by freezing in several base layers up to an order of magnitude greater than those occurring in the asphalt layers. These events were observed to cause cracking at the surface. Furthermore, in structural rutting, i.e. [58][59], related to deeper rather than shallower causes, is observed. As a result, it can be argued how the geometric properties of the base layer can have a major impact on the bearing capacity of the whole pavement structure.

In view of the above, the pavement mechanical strength at the point x of investigation, in terms of stiffness Modulus E'_x MPa, can be predicted as:

$$E'_x = a(E_x) \cdot E_x \tag{2.2a}$$

$$E_x = b \cdot c_x \cdot \tau_x \tag{2.2b}$$

with $a(E)$ being a fitting function, and E_x [MPa] being a first approximation stiffness, defined in Eq. 2.2b as the product of a scale factor b [MPa·m-1] and the thickness of the base course τ [m] times the clay content contribution c [-], which in turn are calculated by GPR tests.

More specifically, the thickness of the base layer has been calculated with reference to the two-way travel time (TWTT) taken by the GPR signal to pass through the layer [61]. This can be determined in Eq. 2.3 as follows:

$$\tau = \frac{c_0 \cdot t}{2 \cdot \sqrt{\varepsilon_{r,base}}} \tag{2.3}$$

where c_0 [ms^{-1}] is the wave velocity of propagation in the free space, t [s] is the temporal distance between the reflection amplitudes from the top and the bottom of the base course (i.e., the peak-to-peak time distance), and $\varepsilon_{r,base}$ [-] is the relative dielectric permittivity of the material composing the base course.

As far as the clay contribution c is concerned, the amplitude of the central peak of the back-received frequency spectrum A is taken as a reference for the assessment of the clay content rising from the subgrade. Indeed, in the tested sites, the expectation on the content of clay rising from the underneath of the tested pavement was that of a poor contribution from this factor. Thereby, highly attenuated spectra are interpreted as indicators of the presence of clay, hence, of a local reduction of the bearing capacity. On the contrary, standard frequency spectra are interpreted as an indicator of stability about the mechanical strength of the pavement.

2.4 Experimental activities

2.4.1 Data collection

In order to calibrate the parametric model, a specific experimental activity has been organised in the District of Rieti, Italy. In more detail, a 1500 m longitudinal section of a two-lane highway (one lane per direction), composed of a typical flexible pavement, has been surveyed using GPR and LFWD equipment. By design charts, the superstructure results in 0.05 m of HMA course, 0.10 m of bitumen-bond base course, and a 0.30 m of subbase layer of unbound granular material, as summarised in Tab. 2.1.

Course	Material	Thickness	SI
Covering	Hot Mixed Asphalt	0.05	m
Base	Bitumen-bond aggregates	0.10	m
Subbase	Granular	0.30	m

Table 2.1: The configuration of the surveyed flexible pavement

More specifically, data from NDTs were collected on the SP31 rural road, nerby the city of Rieti, Lazio, Italy. Surveys were carried out over a lane of a 1500 m long section, shown in Fig. 2.3, on February 18th, 2015.

Quasi-continuous GPR scans were collected with both used antennas along a longitudinal trajectory parallel to the right road shoulder in the travelling direction, at a distance of approximatively 0.75 m. On the other hand, LFWD drops were performed with a 10 m interaxis, at the same distance from the road shoulder.

In practical terms, once the starting point had been identified and marked through a coloured spray on the asphalt as "0", a mark was signed with a constant
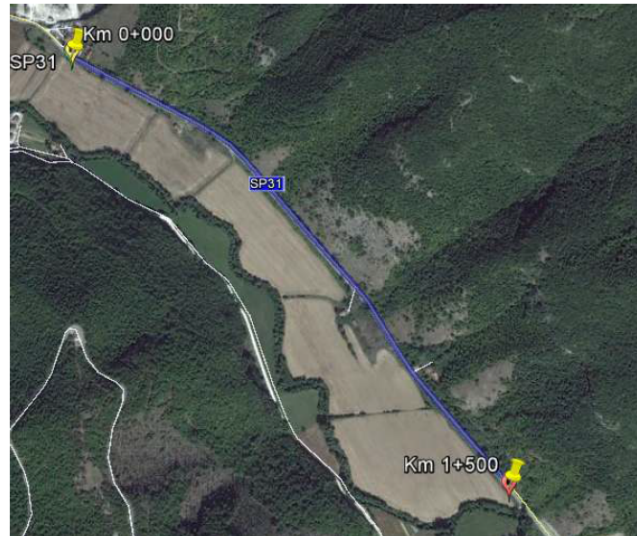
Figure 2.3: The rural road SP31 surveyed with GPR and LFWD in Rieti (IT), 2015

Figure 2.4: The signs marking the interax between the LFWD tests

interaxis of 10 m in the longitudinal direction. Accordingly, 151 marks were apposed over the whole road section, as reference for the position of the LFWD (Fig. 2.4). Furthermore, the distance between the LFWD test positions and the road shoulder was set in order to ensure the perfect matching between GPR and LFWD data. In particular, the distance had been chosen due to the spacing between the center of the antenna and the right wheel of the instrumented van, 0.75 m. The longitudinal matching between GPR scans and LFWD tests were ensured by means of GPS coordinates.

2.4.2 Test Equipment

Concerning the GPR equipment, the RIS Hi-Pave HR1 air-coupled antenna system, manufactured by IDS Georadar, has been used. It is composed of a mono-static horn antenna, with 1000 MHz and 2000 MHz centre frequencies of investigation, mounted behind an instrumented van, shown in Fig. 2.5a. The high frequency of investigation and the type of antenna allowed to single out the reflection from the interface between the thin layers as well as to perform the survey at the traffic speed. The device settings adopted for the on site tests are presented in Tab. 2.2.

Characteristic	Measure	SI
Radar system	Pulse Radar	-
Type of antenna	Horn	-
Central frequency	1000/2000	MHz
Height of antenna overtour	40	$m \cdot 10^{-2}$
Time window	25/40	$s \cdot 10^{-9}$
Numer of samples	512	-
Time resolution	0.049/0.078	$s \cdot 10^{-9}$
Space resolution	2.7	$m \cdot 10^{-2}$

Table 2.2: GPR device setting parameters

The mechanical tests have been carried out using the LFWD Prima 100 (Fig. 2.5b), manufactured by Carl Bro Pavement Consultants Kolding, Denmark. The device is composed of a circular metal plate (diameter 100 mm) loaded by a 10 kg hammer, and geophones that allow to record the surface deflections δ m. The device settings adopted for the on site tests are presented in Tab. 2.2.

However, it is worth noting that as a mechanical testing device for bound layers, LFWD is less acknowledged than FWD. Nevertheless, for sake of consistency with the promising previous field-related studies [60], it was employed for calibration and validation purposes.

2.4.3 Data processing

LFWD data processing

For each load dropping, the device control unit provides the following test parameters:

- Applied Strength [KN]

- Applied Stress [kPa]

Figure 2.5: The GPR (a) and LWFD (b) equipment utilised for surveys in Rieti (IT), 2014

Characteristic	Measure	SI
Height of device	140	$m \cdot 10^{-2}$
Weight of device	27	kg
Falling weight	10	kg
Drop height	85	$m \cdot 10^{-2}$
Plate diameter	10	$m \cdot 10^{-2}$
Load range	$1 \div 15$	kN
Pulse time	$15 \div 25$	$s \cdot 10^{-9}$
Load cell precision	980 ± 40	kN
Resolution	0.1	kN
Frequency range	$0 \div 400$	Hz
Number of geophones	4	-
Geophone precision	± 2	$\%$
Geophone resolution	1	$m \cdot 10^{-6}$

Table 2.3: LFWD device setting parameters

- Surface Deflection [μm]

- Load Pulse [ms]

- Stiffness Modulus [MPa]

Furthermore, at each test point six load droppings have been carried out, in order to gather a statistically significant sample. The database was eventually subjected to a processing stage aimed at filtering out any potential outlier and data related to errors occured in the acquisition.

Concerning the latter, the double-acquisitions due to software bugs (e.g. identical data within the same acquisition, identical data between two consecutive acquisitions) were removed.

As far as the former are taken into account, the statistical distribution of the parameter "Applied Strength" was analysed. Since this value is related to the survey setting rather than the single test location, any anomalous observed value might indicate an incorrect application of the load onto the buffers (e.g. device non perfectly vertical) and, hence, an irregular test.

By calculating the sample mean $\bar{X}$ and the standard deviation σ, a 95% confidence interval for the distribution was defined as:

$$\bar{X} \pm z^* \frac{\sigma}{\sqrt{n}} \tag{2.4}$$

with z^* and n being the 0.025% critical value for the standard normal distribution and the sample size, respectively. The droppings showing outliers strength value, with respect to this interval, have been automatically removed from the database.

Moreover, by observing the speficic survey points, another filter was applied with the scope of limiting the variability between the stiffness moduli calculated at the same location. The following criteria were adopted as idoneity conditions to be respected by the survey point performed at the generic distance x:

$$\frac{|E_{max,x} - E_{avg,x}|}{E_{avg,x}} \cdot 100 < 20\% \tag{2.5a}$$

$$\frac{|E_{min,x} - E_{avg,x}|}{E_{avg,x}} \cdot 100 > -20\% \tag{2.5b}$$

$$\frac{|E_{max,x} - E_{min,x}|}{E_{avg,x}} \cdot 100 < 30\% \tag{2.5c}$$

with $E_{max,x}$, $E_{min,x}$ and $E_{avg,x}$ being the maximum, the minimum and the average value of stiffness observed at the particular LFWD test x.

As a result of these filtering stages, approximatively 18% of the total 151 survey points, have been removed from the database. Accordingly, the remaining length of the test of 1230 m represents the actual database of the study.

GPR data processing

According to the LFWD data, the GPR traces correspondent to the trimmed off areas were also filtered out.

The EM data have been processed following a standard processing scheme for road surveys [18]. In particular, the following processing scheme has been applied to the raw signal:

1. *zero-offset removal* - by applying this filter, the distortion of the received signal due to both the initial direct current signal component and the lowest frequencies signal trend, has been removed. Particularly for road inspections, where the strong dielectric constast at the surface level can generate saturation of the signal by early arrivals, this occurrance is not negligible. The removal has been performed through a simple average-subtractional algorithm, such as the following:

$$y'(n) = y(n) - \frac{1}{N} \sum_{k=1}^{N} y(k) \qquad (2.6)$$

where $y'(n)$ and $y(n)$ are the amplitude of the nth sample of the trace at the pre- and post-processing level, respectively, and with (n, k) ranging from 1 to N. This filter returns an A-scan with mean equal to zero, which means an amplitude's symmetric probability distribution.

2. *band-pass filter* - this filter provides and increase of the Signal to Noise Ratio (SNR) by cutting off from spectrum the frequencies being outside the nominal working bandwith of the employed GPR system. This means that every other sources of signal except the emitter, such as ground-waves and the 'cultural sources' of noise (e.g. nearby vehicles, fences, ...), can be filtered out. In more detail, in case of a time domain raw signal $y(t)$ and its frequency representation $Y(\omega)$ are accounted for, the band-pass filter $H(\omega)$ works as follows:

$$Y'(\omega) = Y(\omega) \cdot H(\omega) \qquad (2.7)$$

where $Y'(\omega)$ is the post-processed signal. There exists various type of band-pass filters, affecting the way the spectrum get reshaped. In this study, a 2nd level Butterworth filter has been used. As width of the working spectrum, a 1.5 times the central frequency has been employed, as suggested by literature [25]. This involves a high-pass frequencies of 250 MHz and 500 MHz and low-pass frequencies of 1750 MHz and 3500 MHz for the two employed antennas, namely, 1000 MHz and 2000 MHz, respectively.

3. *time-zero correction* - the position of the reflection coming from the surface is hardly constant in road inspections, as the vibrations due to the vertical acceleration acting on the towing vehicle determine oscillation of the support of the antenna. This filter helps in preventing possible misin-
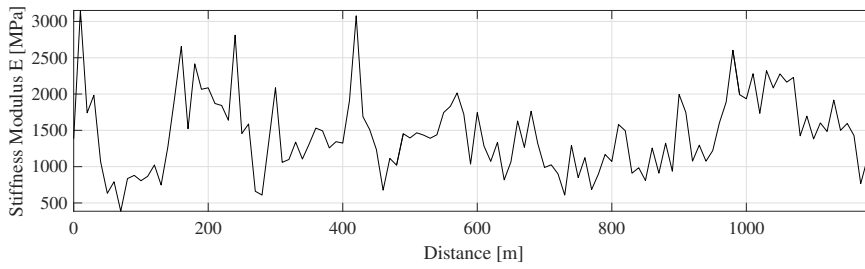
Figure 2.6: Stiffness modulus E [MPa] calculated by LFWD
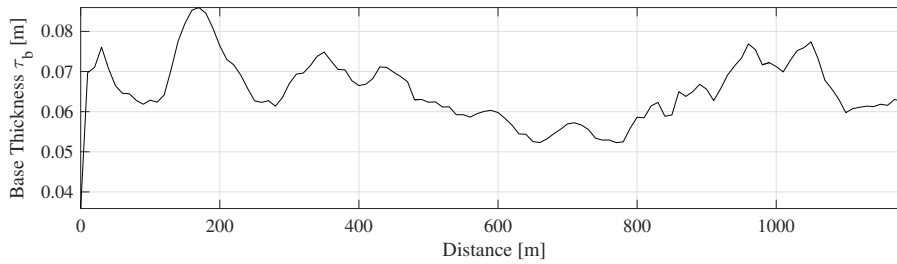
Figure 2.7: Base thickness τ_b [m] calculated by GPR

terpretation of the surface reflection position (e.g. surface damaging) by correcting the first reflection at a common level. Mainly, this obtained by cutting the air layer to a fixed threshold, set at a mostly stable point of the considered trace. Amongst the possible most adviced thresholds, by literature, it was herein chosen to adopt as threshold the zero-amplitude point between the negative and the positive peaks of the first reflection.

Processing outcome

The outcomes of the survey are shown in Fig. 2.6 and 2.7. The trend of the ground-truth values of the stiffness by LFWD (Fig. 2.6) and the trend of the base layer thickness measured by GPR and calculated as in Eq. 2.3 by the TWTT method (Fig. 2.7), are depicted.

2.5 Model calibration

A 100 m-long section (l_{cal}), located between 170 m and 270 m, has been randomly selected for calibration purposes. This distance represents the 6.7% and the 8.3% of the "full" ($l_{tot} = 1500$ m) and the "processed" ($l_{proc} = 1200$ m) road stretch lengths, respectively.

It is worth noting that the outcomes of the calibration process discussed hereafter are representative of the specific testing conditions of this study. These

Figure 2.8: Comparison between trends of measured (solid line) and preliminarily modelled (dashed line with square markers) stiffness modulus

include the flexible pavement structure described in Sect. 2.4 and the percentage of ground-truth data of pavement stiffness taken for calibration purposes. Hence, other values of the calibration parameters apply in the case of different boundary conditions.

Dimensional scaling

The scale factor b is set as:

$$b = \frac{E_{mea,max}}{\tau_{b,max}} \tag{2.8}$$

where $E_{mea,max}$ is the overall maximum value of the stiffness modulus observed within the 120 LFWD measurements collected over the total length l_{proc}, and $\tau_{b,max}$ is the maximum thickness of the base course recorded by GPR, calculated by TWTT within the calibration length l_{cal}.

In Fig. 2.8 the trend of preliminarily modelled stiffness modulus $E_{mod,x}^*$, calculated as:

$$E_{mod,x}^* = b \cdot \tau_{b,x} \tag{2.9}$$

along l_{cal}, is shown. The application of the preliminar model produces an evident overestimate of the measured ground-truth data $E_{mea,x}$ (solid line in the figure). This mismatch is further addressed in the following subsection, by means of a dedicated fitting function.

Clay contribution

The amplitude of the central peak of the frequency spectrum A_p is considered as the benchmark parameter to account for the presence of clay rising from the foundation level [62]. To this purpose, geological maps of the site [64] are analysed and the investigated stretch of road is classified as belonging to a poorly-clayey geological area. Hence, highly attenuated frequency spectra are interpreted as indicators of likely presence of clay and are related to areas of early decay and loss of road bearing capacity. On the contrary, standard frequency spectra are interpreted as indicators of stability in terms of strength and deformation properties of the pavement.

The stair function $c(A_{p,x})$ is defined from the analysis of the central peak amplitude $A_{p,x}$ of the frequency spectrum of the GPR signal collected at a generic position x within the calibration road stretch l_{cal}. This function is developed to lower the modelled stiffness modulus when the value of $A_{p,x}$ is lower than a reference optimal threshold value (i.e., when the spectrum is attenuated). It is expressed as follows:

$$c(A_{p,x}) = \begin{cases} 0.80, & \text{if } A_{p,x}^{[0,1]} < A_t \\ 1, & \text{elsewhere} \end{cases} \tag{2.10}$$

where $A_{p,x}^{[0,1]}$ is the central peak amplitude of the frequency spectrum, normalised in the calibration range l_{cal} and A_t is the set threshold. The threshold A_t is defined after running the model for each i_{th} value $A_{t,i}$, with i ranging between 0.80 and 1 at steps of 0.01. The trend of the i_{th} values of $A_{t,i}$ in the defined range is described by the following objective function $\varphi(A_{t,i})$:

$$\varphi(A_{t,i}) = \sqrt{\frac{\sum_{x=0}^{l_{cal}} |E_{mod,x,A_{t,i}} - E_{mea,x}|^2}{\sum_{x=0}^{l_{cal}} E_{mod,x,A_{t,i}}^2}} \tag{2.11}$$

expressing the mismatch between the modelled $E_{mod,x,A_{t,i}}$ and the measured E stiffness modulus. Fig. 2.9 shows the performance of the model with varying values of $A_{t,i}$. A minimum value of 0.034 for $\varphi(A_{t,i})$ is reached when $A_{t,i}$ is equal to 0.857; hence, this value is taken as the optimal threshold expressing A_t.

It is worth specifying that the $A_{p,x}^{[0,1]}$ parameter improves the model matching at the local maximum and minimum points of the measured trend of stiffness, whereas the overall model overestimation is addressed using a dedicated fitting function, as detailed further in following subsection.
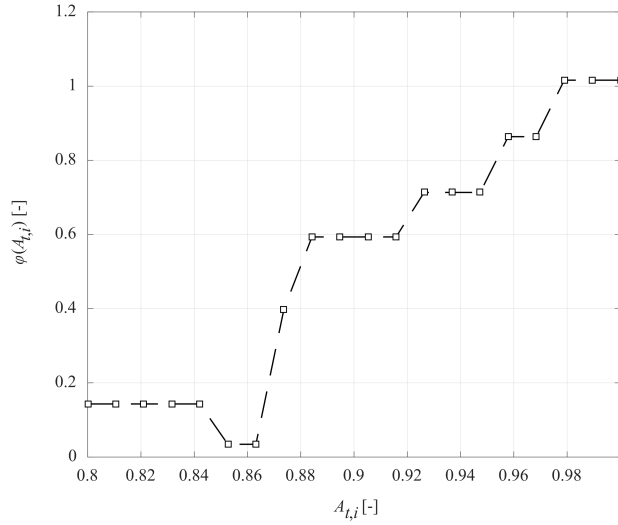
Figure 2.9: The trend of the objective function $\varphi(A_{t,i})$ with varying values of $A_{t,i}$

Fitting function

A percentile analysis of measured and modelled stiffness moduli (Fig. 2.10a) is performed to ensure accurate evaluation of the model overestimation. The ratio of the modelled to the measured percentiles (Fig. 2.10b) is therefore calculated as a reductive factor for compensation purposes. Hence, the continuous function $a(E_{mod,x})$ is derived using the following third-degree polynomial fitting relationship:

$$a(E_{mod,x}) = \sum_{i=0}^{3} a_i E_{mod,x}^i \tag{2.12}$$

The values of the fitting parameters a_i are reported in Tab. 2.4.

a_0	a_1	a_2	a_3
-22.618	0.027	$-1.24 \cdot 10^{-6}$	$1.74 \cdot 10^{-9}$

Table 2.4: Fitting parameters a_i in Eq. 2.12

The adjusted modelled trend of stiffness modulus is therefore derived working out the value of the fitting function $a(E_{mod,x})$ from Eq. 2.12 into Eq. 2.2a. Fig. 2.11 shows the comparison between trends of measured and (adjusted) modelled stiffness modulus along the calibration road stretch.
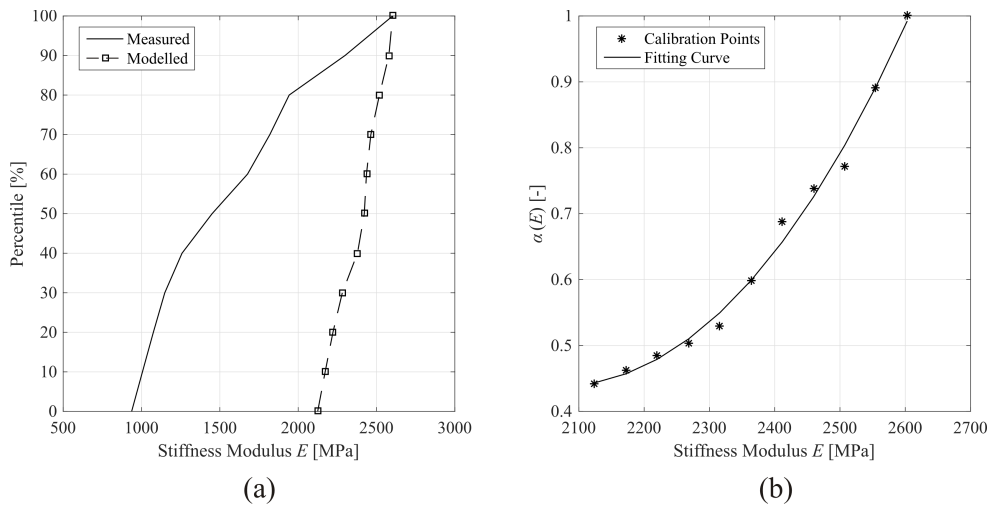
Figure 2.10: Percentile analysis of measured (solid line) and modelled (dashed line with square markers) stiffness moduli; (b) fitting function $a(E_{mod,x})$expressed by Eq. 2.12
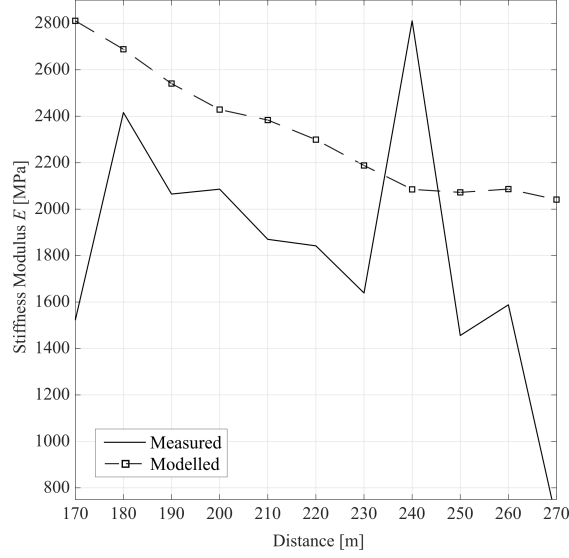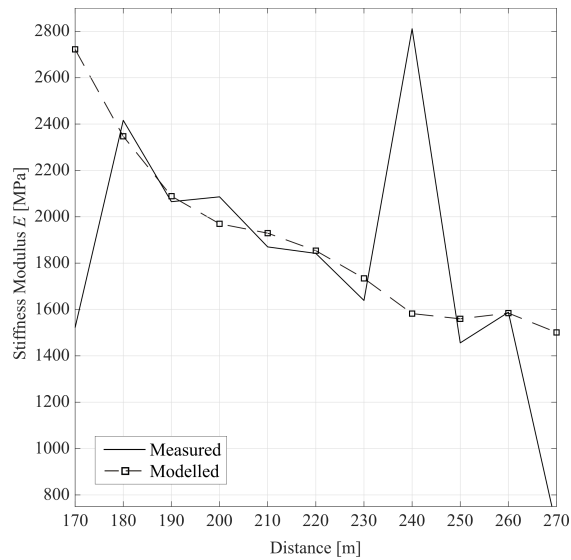

Figure 2.11: Comparison between trends of measured (solid line) and modelled (dashed line with square markers) stiffness modulus after the application of the fitting function $a(E_{mod,x})$ (Eq. 2.12).

2.6 Results

2.6.1 Quantitative considerations

The trend of modelled values of fully-calibrated stiffness modulus $E'_{mod,x}$ is estimated along the processed road stretch length l_{tot}. An overall comparison between trends of measured and modelled stiffness modulus is shown in Fig. 2.12. For the sake of clarity with the data interpretation, the 1200 m road stretch length is divided into two sub-areas, i.e., from markers "0 m to 600 m" and "600 m to 1200 m". The area related to the calibration road stretch is marked in grey.

A relatively good reliability of the model for the interpretation of the actual road pavement stiffness is proven. A few areas of ground-truth data misinterpretation from the model are still recognizable in the neighbourhood of markers "100 m", "400 m", "550 m" (Fig. 2.12a) and "900 m" (2.12b). The normalised root-mean-square deviation (NRMSD) is equal to 0.273. This provides a quantitative measurement of disagreement between measured and modelled datasets of stiffness modulus.

The assumption made on the percentage size of the LFWD calibration points (i.e., 10% of the data from the full dataset) is further investigated to verify the robustness of the model. To this purpose, the fully-calibrated model is applied with calibration data ranges comprised between 10% and 30% in steps of 5%; hence the relative values of NRMSD are found and plotted (Fig. 2.13).

It is worth noting how the robustness of the model has a weak dependence on the percentage range of calibration points. This is proved by the slight variability of the NRMSD values and the fair horizontality of the least square fitting trend line. Thereby, it is possible to argue that a robust calibration can be performed using 10% of ground-truth calibration points, whereas the length of the relative full dataset is at least the same as the length of the road stretch investigated in this study. This may represent an invaluable outcome for the development of a more time-efficient methodology for the estimation of the stiffness of road flexible pavements. In fact, the use of FWD could be potentially limited to the 10% only of the full length of the roadway whereas the rest of the survey could be carried out using an air-coupled GPR system for a more time-efficient data collection.

2.6.2 Qualitative considerations

To foster the viability of using air-coupled GPR antenna systems in combination with FWD systems in PMSs, a qualitative and streamlined approach to estimate stiffness of road flexible pavements is further proposed. The rationale
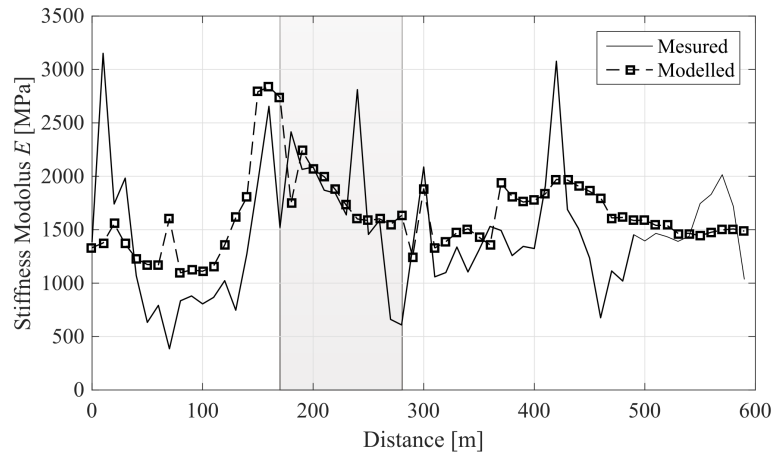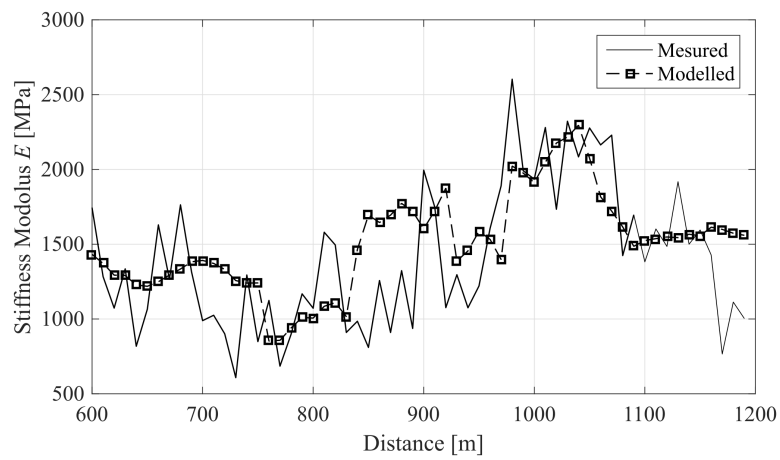
Figure 2.12: Comparison between trends of measured $E_{mea,x}$ (solid line) and modelled $E'_{mod,x}$ (dashed line with square markers) stiffness modulus after the application of the fully-calibrated model. The area related to the calibration road stretch is marked in grey. (a) Markers "0 m – 600 m"; (b) markers 600 m – 1200 m".
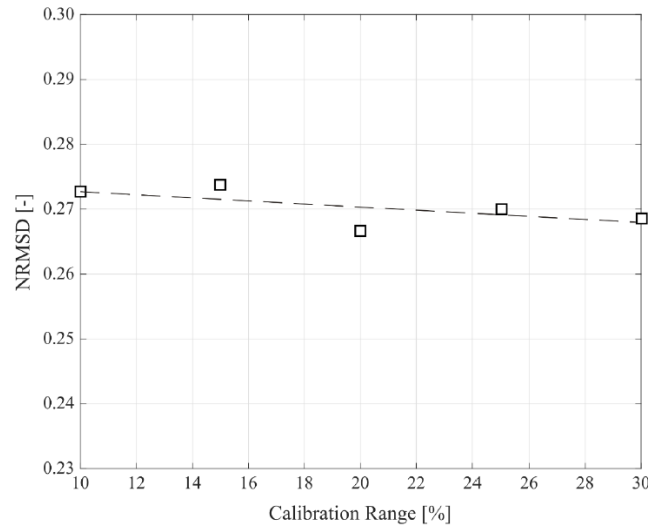
Figure 2.13: The trend of NRMSD values of the model against the percentage range "10% - 30%" of LFWD calibration points.

behind this process is to provide rapid identification of early decay and loss of bearing capacity areas at the network level. Hence, time and cost of further and more detailed investigations can be planned and allocated more effectively.

Stiffness moduli estimated from Eq. 2.2a and Eq. 2.2b are here considered as ground-truth and modelled values, respectively. The investigated road stretch is divided into 50m-long value ranges of stiffness modulus wherein the average value is taken as a benchmark. Three classes of stiffness are therefore identified, i.e., "high stiffness", "medium stiffness" and "low stiffness" classes. These are set as a function of two thresholds, arbitrarily fixed at 1900 MPa and 1100 MPa, according to the overall trend of modelled stiffness moduli. This step allows for customisation of the methodology as per the specific requirements of the survey. Fig. 2.14 shows the outcomes of the qualitative modelling.

From the comparison between measured and modelled stiffness by the qualitative approach, matches of two main areas of lowest stiffness are observed in the value ranges "100 m – 150 m" and "700 m – 900 m". In addition, a good match between highest stiffness moduli is noticed in the value ranges "200 m – 250 m" and "1050 m – 1100 m". The remaining intervals match well with intermediate stiffness conditions of the road pavement.

It is worth noting the relative range of applicability of the proposed approach. The set values of the threshold are specific to the dataset collected in this investigation. Hence, they may change for a different dataset (e.g., the same pavement structure at a different life cycle stage or another road pavement with a different cross section and/or construction materials). To this effect, the proposed
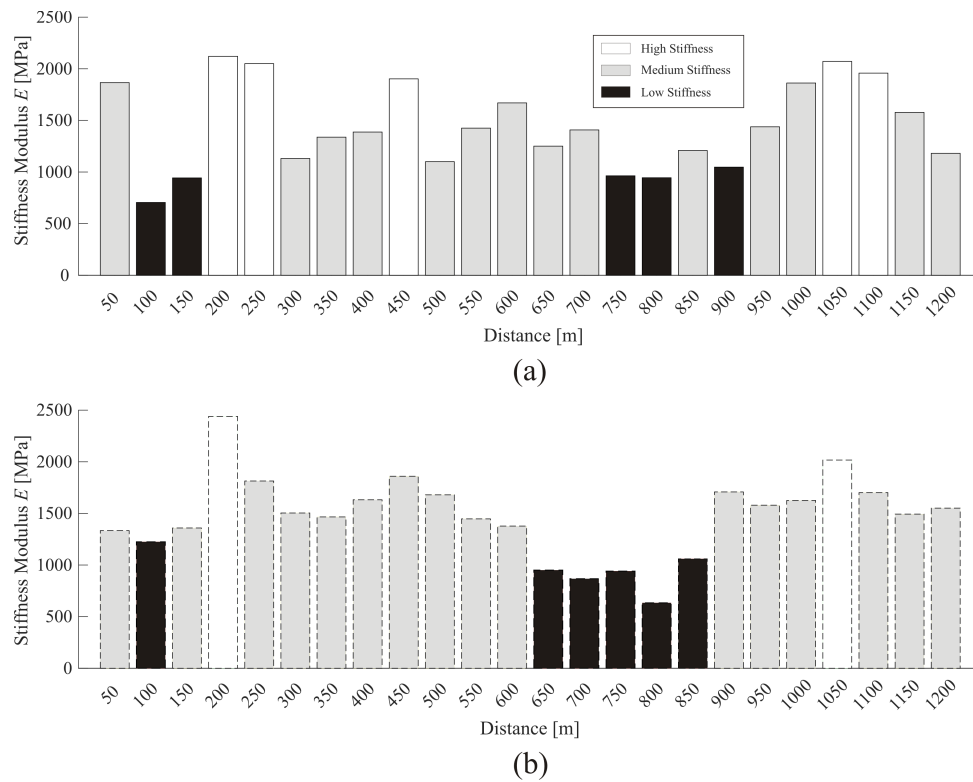
Figure 2.14: Comparison between the three qualitative classes of stiffness modulus: (a) measured stiffness modulus (bar charts with solid contour lines); (b) modelled stiffness modulus (bar charts with dashed contour lines).

methodology is reliable and can be used to investigate other road flexible pavements only if suitable threshold values are set after a preliminary data analysis at the network level.

2.7 Conclusions

This work proposes an experimental-based model for the assessment of stiffness in a road flexible pavement using ground-penetrating radar (GPR) and light falling weight deflectometer (LFWD). The model uses ground-truth data of road stiffness inferred from LFWD as well as geometric and physical information of the pavement structure derived from a GPR system equipped with high-frequency horn antennas.

To this purpose, 1500 m of a two-lane highway (one lane per direction) with a flexible pavement structure are investigated. After filtering out the outliers from the collected LFWD data (and the relative GPR traces), the model is calibrated via an optimisation process using the ground-truth stiffness moduli at the investigation points of a randomly-selected 100m-long road stretch (i.e., 10% of the processed dataset), the thickness of the base layer and the central-peak amplitudes of the frequency spectrum. These latter parameters are both estimated using GPR and account for the structural quality of the pavement and the clay content in the load-bearing layers, respectively.

In addition to the quantitative approach for the estimation of the pavement stiffness modulus, a qualitative procedure is further developed. The investigated road stretch is divided into 50m-long value ranges of stiffness modulus, wherein the average value is taken as a benchmark. Three classes of pavement stiffness (i.e., "high stiffness", "medium stiffness" and "low stiffness") are therefore set based on two arbitrarily-fixed threshold values. These are selected according to the overall trend of modelled stiffness moduli and allow for customisation of the methodology as per the specific requirements of the survey.

The model viability is finally evaluated by quantitative and qualitative comparison of measured and modelled stiffness moduli. The quantitative analysis of the outputs shows a value of the normalised root-mean-square deviation (NRMSD) equal to 0.273. Hence, a relatively good agreement between measured and modelled data is proven. This outcome is also confirmed by the quantitative analysis, whereby good matches of the defined stiffness classes are found across the whole investigated road stretch.

It is important to emphasize the importance of the proposed methodology for

extensive and time efficient assessment of roads at the network level and potential implementation in pavement management systems (PMS). This could be crucial for road administrators and agencies in order to define priorities of intervention, allocate costs effectively and decrease the likelihood of envisaged accidents.

Future research could task itself with enriching the database for the development of the proposed methodology with a larger data sample from different road sections. In addition, different sources of ground-truth data for collection of stiffness moduli (e.g. falling weight deflectometer, curviameter, traffic speed deflectometer) could be used for the investigation of deeper domains and/or the gathering of more dense data. Comparison of model outputs against the actual strength and deformation data would allow for the understanding of the viability of different ground-truth equipment for modelling purposes.

Chapter 3

Railway Applications

3.1 Background

Railways are major transportation assets in fostering the economic development and providing massive transport of public and freight.

To tackle the challenge of i) sustaining a growing demand for freight and passengers timely and safely, and ii) competing with other modes of transportation, railway industries are seeking lower construction and maintenance costs while maintaining high levels of serviceability. To this purpose, the effective management of funds allocation (proper maintenance of the railways) and the efficient inspection of rail networks are factors of paramount importance, as stressed out in introduction section.

Within the railway construction types, the ballasted rail tracks are the most widespread as these allow for effective drainage of the track-bed and provide proper load-bearing capacity at relatively low costs. From a structural point of view, a track structure is composed of a superstructure (steel rails, fastening systems and concrete/timber sleepers) laying over a substructure (ballast, subballast and subgrade). The cyclic loading exerted by the moving trains affects the structural stability of these two components, although major deformations occur mostly in the ballast and subballast layers. Thereby, the proper selection and the effective monitoring of the ballast aggregates are factors of paramount importance in the construction and maintenance stages. This is due to the progressive deterioration and segregation of the aggregates under heavy cyclic loading [65].

The railway ballast layer usually consists of uniformly-graded coarse aggregates produced from crushed rocks such as granite, basalt, limestone or gravel. The major structural and functional tasks of the ballast aggregates are i) to resist to the vertical, lateral and longitudinal forces applied to the sleepers, ii) to lower

the pressure from the sleeper-bearing area into minor stress levels for the underlying material and *iii*) to provide effective water drainage [66]. Differential railway track settlements with implications on the operational safety of the infrastructure can be due to the combination of several critical factors, such as the number and the amplitude of the load cycles, the track confining stress, the aggregates grading, the angularity and the fracture strength of the grains. The track stability is also widely affected by the ballast fouling, which is broadly related to the breakdown of the ballast aggregates and the infiltration of external materials from the ballast surface and/or from the base of the ballast layer. Nevertheless, the most important source of fouling reported worldwide is related to the segregation of the ballast aggregates (i.e., the formation of smaller ballast aggregates) [66]. In view of this, the effective monitoring and detection of "critical" geometric features of the aggregates, such as the grain size characteristics, are necessary to ensure the optimum maintenance of the rail infrastructure. These actions contribute to preserve the structural stability of the rail track as well as to maintain proper operational safety conditions.

Drilling and digging trenches at even intervals along the track are widespread methods to retrieve physical and geometric information on the railway ballast. Nevertheless, these techniques are intrusive, locally representative of extensive rail infrastructures and require to constrain the operation of the trains. Within this context, NDTs are becoming popular in railway engineering. The applications of infrared imaging [67], electrical resistivity tomography [68], seismic surveys [69] and, mostly, ground-penetrating radar (GPR) [70] have increased over the last two decades. According to *Roberts et al.* [71], first GPR applications in railway engineering date back to the nineteen eighties [72]. In view of Section 1.1, information can be inferred about the layer thicknesses and the materials properties from the analysis of GPR signal collected on field.

Overall, the GPR-based research on railway ballast can be classified into *i*) research based on the analysis of the signal response in the time domain and *ii*) research based on the analysis of the signal spectrum in the frequency domain.

The earliest and the most tackled GPR investigations on railway ballast are broadly comprised in the above first class of research. Within this context, comprehensive analyses of different types of ballast (i.e., mineralogy and grain size) can be found in [73][74][75]. Usually, the assessment of the permittivity of the substructure layers [76][77] and the analysis of the signal amplitude variability are developed [78][79].

On the other hand, the frequency-based analysis (i.e., spectral analysis) of the GPR data has become popular for railway applications since the second half of the

noughties. The main benefit of this approach is that minimum or no destructive sampling is required for the calibration of the system. The time-variation of the frequency spectrum was investigated by *Leng and Al-Qadi* [80] using the short-time Fourier transform (STFT) approach. The authors demonstrated graphically the variation of the frequency energy with the ballast depth under different fouling conditions. *Shao et al.* [81] developed an algorithm to extract magnitude spectra at salient frequencies and to classify railway ballast conditions using support vector machines. *Xiao and Liu* [82] used the forward and the inverse S-transform to 100- and 400-MHz GPR data. The GPR spectra from both the frequencies were fused together and new spectra with broader bandwidth were derived. In view of this, the authors obtained an effective trade-off between good resolution and deep penetration in ballast surveys. More recently, the finite-difference time-domain (FDTD) simulation of the GPR signal has proved to be an effective technique for the interpretation of complex scenarios in rail substructures and the validation of the above approaches [83][84].

The above-mentioned methodologies demonstrated high reliability and good effectiveness for the ballast health monitoring and the fouling detection. Nevertheless, to the best of our knowledge, no studies to date have focused on the assessment of the "critical" geometric features of the ballast aggregates with GPR-based methods implemented in the frequency (spectral) domain of the signal. Furthermore, no research was specifically carried out in the spectral domain of the GPR signal to assess the geometric characteristics of coarse-grained sharp aggregates, such as the railway ballast aggregates.

In view of the above, a methodology based on the spectral analysis of GPR data collected using a high-frequency horn antenna is herein presented [85]. A multi-stage process in terms of ballast grain size was developed. FDTD numerical simulations and real tests were both performed to analyse the spectral behaviour of the collected GPR signals [84][85]. The data from these tests were used for modelling purpose. In this regard, information about relevant geometric features of the railway ballast aggregates was found with respect to the shifting of the frequency spectrum peak.

3.2 Objective & methodologies

This studies focuses on the assessment of "critical" geometric features of the ballast aggregates within a railway track-bed. To this purpose, spectral analyses

of the high-frequency GHz GPR data were performed in the frequency domain. A bottom-up approach that used simulated and real data collected from laboratory experiments was followed. FDTD simulations with the gprMax 2D numerical simulator [87] were firstly performed. In the first simulation tests, simplified models of monosized ballast particles were taken into account. The diameters of the above particles were progressively increased in the range of usage of the ballast aggregates for the construction of railway track-beds. Single- and multi-particle scenarios were simulated and the corresponding frequency spectra of the signals were analysed. Afterwards, the numerical model was rendered more complex by performing real-scale simulations of multi-sized ballast particles. The information on the grain size of these particles was retrieved by the grain size distribution of three typical grading curves used by railway network operators for the construction of ballasted track-beds. The reproduction of the above complex numerical model was obtained by the combination of the random sequential adsorption (RSA) paradigm and the FDTD technique. Real tests were subsequently carried out in the laboratory environment where three different scenarios of the ballast aggregates arrangement were manufactured [84]. Finally, the modelling of the frequency spectrum peak and the equivalent diameter of the ballast aggregates was developed.

Moreover, amongst the specific objectives of this work is the analysis of the EM response of this railway ballast as a function of the frequency of investigation, the system configuration, the arrangement of the ballast stones, and the permittivity estimate method. Basically, the time domain signals collected have been first processed and all the useless information filtered out from the raw signals. Then, the relative dielectric permittivity of the air-ballast system has been evaluated by means of an estimate of the wave propagation velocity within the medium [56]. In the case of air-coupled antenna systems, the surface reflection method (SRM) [24] has been also employed for retrieving the permittivity of the medium. The laboratory experiments were undertaken in a methacrylate tank wherein the ballast has been filled and emptied several times, such that different scenarios in terms of stones arrangement were performed.

3.3 Modelling

In order to investigate the propagation and the scattering of an EM wave through a dielectric medium such as a ballast layer in a railway track-bed, a
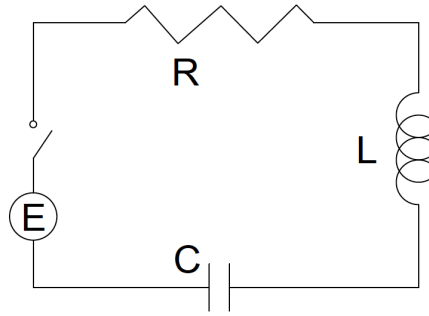
Figure 3.1: Diagram of the analogous electrical circuit representing one ballast grain to which an EM field is applied

simplified "analogous" physical model, based on the circuit theory, was proposed to approximate the real system.

It is known that the ballast particles hold an electrical conductivity σ that is dependent on the mineralogy of the source rock. Consequently, an EM wave that propagates through these dielectrics is expected to undergo electrical losses and attenuation. To this effect, a second order model can be used to represent a simple system composed of one ballast grain to which an EM field is applied. This system was streamlined in the analogous electrical circuit showed in the diagram of Fig. 3.1.

The system is composed of an electromotive force $E(t)$ applied to a circuit with one resistor R, one inductor L and one capacitor C, all of which are connected in series. According to the Kirchhoff's voltage law, a second order differential equation, expressing the charge $Q(t)$ that moves into the capacitor, can be derived as follows:

$$L\frac{\partial Q(t)^2}{\partial t^2} + R\frac{\partial Q(t)}{\partial t} + \frac{Q(t)}{C} = E(t) \tag{3.1}$$

In case of negligible R, the natural pulsation of the system ω_n is given by:

$$\omega_n = \frac{1}{\sqrt{LC}} \tag{3.2}$$

Considering now a single ballast aggregate particle subject to the influence of an EM field pulsed around a central frequency with a certain frequency bandwidth. According to the above simplification of the analogous electrical circuit, L and C depend on the geometric features of the single ballast particle, whereas R hinges on the inverse of the electrical conductivity $1/\sigma$ of the medium. Hence, once the dimension of the particle is fixed and σ is known, a particular frequency is expected to generate resonant effects. In the event that this particular fre-

quency belongs to the bandwidth of the EM pulse, it is therefore expected to observe an amplification of the spectrum at that specific frequency.

Accordingly, it is expected to propose a model as in Eq. 3.3, capable of relating the geometric feature representing the ballast grading D^* to the frequency of the spectrum peak P_f.

$$D^* = f(P_f) \tag{3.3}$$

In view of the above, the numerical simulation was used to investigate thoroughly the role exerted by L, C and R in the generation of the resonant effects as well as to infer information about the dimension of the ballast aggregates. This allowed analysing the spectral behaviour of different sizes of rock grains that were illuminated by a known pulsed EM field.

The resulting model was finally validated through real GPR data collected in laboratory environment, where an experimental set up was purposely accounted for.

3.4 Experimental activities

3.4.1 Laboratory activities

Geometrical assessment of ballast

The experimental design is focused on the analysis of the EM behaviour of clean limestone ballast aggregates in dry conditions. A laboratory setup is arranged for testing the combination of differing factors, namely, i) the type of radar system; ii) the antenna frequency; iii) the proposed data processing scheme; iv) the GPR method of data analysis; v) the arrangement of the ballast aggregates. Tests are carried out in static conditions and all the analyses were focused on the A-scan data outputs (e.g. Fig. 1.2a). A number of preliminary analyses are performed to investigate into the footprints of all the available radar systems [88][89]. To this effect, the testing conditions are reproduced using the GPR systems and the available PEC only. The effective areas illuminated by the antennas on the PEC are determined following the manufacturer's recommendation on the systems' beam of radiation and after double-checking the signal disturbance by practical tests. These provide a gradual approach of a metallic reflector from the edge to the centre of the PEC while measuring with the GPR systems. The footprint boundaries are therefore determined when a disturbance to the signal is noticed (i.e., the signal is subject to edge effects). In view of the above framework,
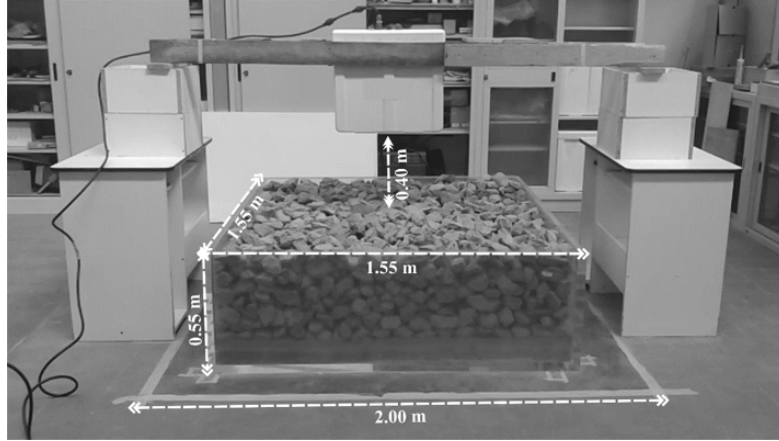
Figure 3.2: Experimental setup for the measurements carried out in the laboratory with an air-coupled antenna system

the largest dimension of the footprint at the PEC surface turns out to be 150 cm and it is taken as the benchmark for the side of the container. This investigation is useful for the design of the dimensions of the container in order to assume the surveyed medium as horizontally infinite with negligible border effects.

A square-based methacrylate tank is used for testing purposes (Fig. 3.2). The container has outer base side and height of, respectively, 1.55 m and 0.55 m, and inner dimensions of 1.47 m (side of the base) and 0.48 m (height). A 2 m × 2 m copper sheet PEC is laid underneath the container, thereby allowing for the full reflection of the EM waves propagating through the "ballast system". It is also worth noting that the dimensions of the investigated volume are designed to comply with the typical sizes of ballast layers in rail track beds.

Ground-coupled and air-coupled GPR antenna systems, manufactured by IDS Georadar (Fig. 3.3), are used for testing purposes. The RIS 99-MF Multi Frequency Array Radar-System is equipped with 600 MHz and 1600 MHz central frequency antennas. The system collects data by means of four channels, i.e., two mono-static and two bi-static. In this study, only the 600 MHz and 1600 MHz mono-static channels are used for data collection. A time window of 40 ns is used for the acquisition of the signal. In addition, three air-coupled GPR systems equipped with central frequency antennas of 1000 MHz (RIS Hi-Pave HR1 1000) and 2000 MHz (RIS Hi-Pave HR1 2000 and RIS Hi-Pave HR1 2000NA) are used. Time windows of 25 ns and 15 ns were set for, respectively, the 1000 MHz and the 2000 MHz GPR systems. Proper combination of time window and sampling interval is mandatory to avoid over-/under-sampling of the signal collected, hence to modify/lose information [20]. With regard to the 2000 MHz antenna systems, both a standard version of the horn antenna for the European market and a low-
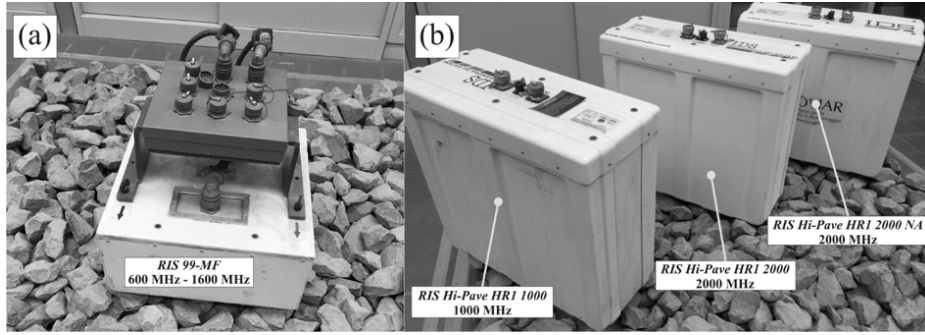
Figure 3.3: GPR equipment used for testing purposes: (a) RIS 99-MF ground-coupled multi-channel GPR system, and (b) RIS Hi-Pave air-coupled antenna systems (1000 MHz, 2000 MHz and 2000 MHz (NA))

	Ballast properties	Standard	Reference unit	Value	Class
Geometric	Grain size	EN [94]	passing %	100-100-79.9-30.6-1.2-0.3	A
	Fine content	EN [94]	passing %	0.5	A
	Grain length	EN [95]	%	5.5	B
	Shape Ind. -SI-	EN [95]	%	20.0	SI_{20}
Mechanical	Resistence -LA-	EN [96]	%	20.0	LA_{20}
	Density -ρ_s-	EN [97]	g/cm^3	2.8	-
& Physical	Voids perc. -ϕ-	EN [92]	%	41.0	-
	Moisture - w-	ISO [93]	%	0.2	-

Table 3.1: Main properties of the limestone ballast aggregates assessed by using standard test methods

powered version for the North-American (NA) market are used. In this regard, it is known that manufacturers must comply with different regulations about the power emission limit as per the country's specific needs. The challenge is mostly in countries like the United States where the threshold for the maximum power emission is very low. Due to this lower radiative power, this type of GPR systems exhibit worst performances in terms of signal-to-noise (SNR) ratio [90]. It is therefore important to test and compare the results to check the viability of low-powered GPR systems in assessing the dielectrics of railway ballast.

Limestone ballast aggregates, typically used for the construction of ballasted railroads, are utilised for testing purposes. Prior to the GPR tests, a thorough assessment of the main geometric, mechanical and physical properties of the ballast aggregates is carried out according to the EN 13450:2002/AC:2004 standard [91]. In addition to this standard, further standard test methods for the assessment of the percentage of voids [92] and the water content [93] are followed. All of the above properties are listed in Tab. 3.1.

Three main scenarios of arrangement of the ballast aggregates are reproduced in the laboratory, by filling up and emptying the container. For each scenario,

the full set of air-coupled GPR systems are used and 9 tests are performed.

Phyisical assessment of ballast

In addition, in order to investigate both clean and fouled conditions of railway ballast, four configurations of ballast aggregate particles and pollutant fine-grained silty soil material were manufactured within the square-based tank. The test scenarios have been set up by polluting the voids within ballast aggregates with the fine-grained material, through a three-step process. At each step of the fouling process, the data were collected using the GPR system presented above.

As far as the pollutant material is concerned, the most important geometric (i.e., grain size), mechanical and physical properties (i.e., plasticity, particle density, water content) were determined in the laboratory environment through standard tests shown in Fig. 3.4. Moreover, Tab. 3.2 summaryses the relevant values derived from the laboratory tests.

The considerable size of the investigation domain and the relevant quantity of ballast aggregates (1500 kg) and pollutant soil material (from 250 kg to 800 kg, depending on the fouling level) to manage, have led developing preliminary "small-scale" laboratory procedures. These have favoured standardizing the mechanical and physical conditions that were reproduced subsequently for the material within the entire volume of the tank.

To ensure the effective distribution and uniformity of the pollutant material within the ballast inter-particle voids, a wooden square grid mesh of 16 quadrants with 0.35 m sides was equipped with a 4 mm-size sieving grid. Once the silty soil was distributed within the wooden support quadrants, compaction and filling of the intergranular voids were obtained by using a hammer drill equipped with a square-shaped drill bit. To this purpose, a dedicated laboratory procedure was preliminarily implemented in a small-scale formwork with dimensions comparable to those of the above quadrants. In addition, the time required for reaching the maximum compaction of the silty material with the above hammer drill was evaluated. In this regard, the maximum value of dry density ρ_d was reached after 10 s of vibration induced by the hammer.

To make the results from the proposed compaction procedure comparable to the outcomes of the relevant standard test methods, the energy of compaction spent with the hammer drill was compared to the same parameter achieved with i) the Proctor test for mixes compacted with a 2.5 kg rammer in the Proctor mould and ii) the Modified Proctor test for mixes compacted with a 4.5 kg hammer in the
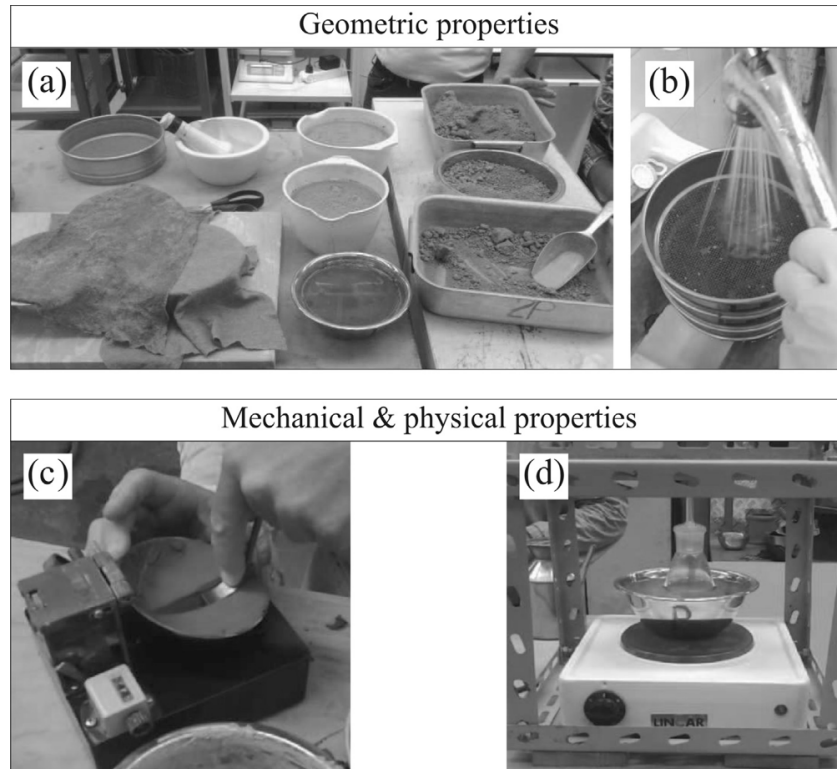
Figure 3.4: Tests performed in the laboratory environment for the assessment of the pollutant soil material properties: (a) samples preparation; (b) soil particles sieving under water flow (grain size analysis) [94] ; (c) cutting of a standard groove into the molded material with a test-specific knife (soil plasticity test) [98] ; (d) boiling of the immersed specimen for deaeration (particle density evaluation test) [99]

large Proctor mould [100]. The overall compaction energy per unit volume spent with the hammer amounted to $1.04 \cdot 10^6 \, J/m^3$, whereas values of $0.59 \cdot 10^6 \, J/m^3$ and $2.68 \cdot 10^6 \, J/m^3$ were found for the Proctor and the Modified Proctor tests, respectively. In view of the obtained values of energy, it can be argued that the compaction procedure here proposed ranked between the Standard and the Modified Proctor test.

Four main configurations (Tab. 3.3) were manufactured in the laboratory environment. In all of these scenarios, the material investigated filled the entire inner tank height of 0.48 m.

Starting from the clean ballast condition (i.e., Test scenario 0), the fouling was reproduced by layers of a mix between the pollutant A4 silty soil and the ballast aggregates. The height of this mix was progressively increased by steps of 0.10 m. Mixing and compaction of the materials were performed according to the procedures before discussed. The above fouled configurations were set to be representative of low (i.e., 0.10 m of fouled ballast (FB) – Test scenario I),

	Soil properties	Standard	Reference unit	Value	Class
Geometric	Grain size	EN [94]	passing %	100-99.6-99.4-84.7	A4
Mechanical	Liquid Limit -L_L-	EN [98]	%	24.6	-
	Plastic Index -I_P-	EN [97]	%	7.6	-
& Physical	Density -ρ-	EN [99]	g/cm^3	2.5	-
	Moisture - w-	ISO [93]	%	2.5	-

Table 3.2: Geometric, mechanical and physical properties assessed in the laboratory environment for the pollutant soil material

Test Scenario	Height of the mixtures [m]	Configuration [m]
0	0.48	0.48 CB
I	0.48	0.10 FB + 0.38 CB
II	0.48	0.20 FB + 0.28 CB
III	0.48	0.38 FB + 0.18 CB

Table 3.3: Configurations of the ballast-pollutant mixes investigated in the laboratory (CB = Clean Ballast; FB= Fouled Ballast)

medium (i.e., 0.20 m of FB – Test scenario II) and high (i.e., 0.30 m of FB – Test scenario III) levels of fouling within the ballast layer of a railway track bed. A loop laboratory procedure was followed for the manufacturing of the four scenarios. Starting from no-fouled ballast conditions (i.e., Test scenario 0), the clean ballast aggregates were removed from the top of the tank at progressively lower amounts each more step, up to reaching the wanted height of the fouled layer. Therefore, mixing and compaction procedures were carried out. Afterwards, the clean ballast aggregates were placed again above the compacted fouled layer of ballast up to filling the entire height of the tank. The above "emptying and filling" loop was repeated until the conditions of scenario III were reached. The GPR surveys with the three aforementioned air-coupled antenna systems were performed at each of the above reproduced scenarios.

Fig. 3.5 shows the tank filled with clean ballast aggregates (Fig. 3.5a) and an all-in-one image of the above four configurations merged together (Fig. 3.5b).

3.4.2   Numerical simulation

Particle scale

To verify the theoretical framework of Section 3.3, a number of numerical simulations were developed. A bi-dimensional scenario was built using the Finite Difference Time Domain (FDTD) technique implemented in the numerical simulator package gprMax 2D. The model did not include the physical structure of
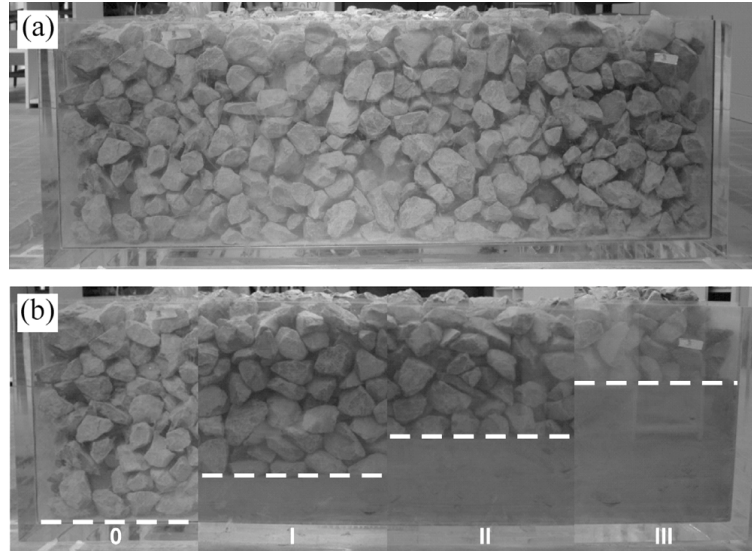
Figure 3.5: (a) Methacrylate tank filled with clean ballast aggregates; (b) all-in-one image of the four scenarios merged together (the dashed lines separate the clean (top) from the uniformly-fouled (bottom) ballast layer).

the antenna. A line of current suspended in the free space represented the source.

To reproduce the real conditions, the distance between the emitter TX and the receiver RX was set at 0.30 m. Finally, a circle-shaped target with dielectric properties of a typical limestone material (i.e., $\varepsilon_r = 7$; $\sigma = 0.001 Sm^{-1}$) was selected to represent the ballast particle, and it was placed 0.80 m below the source. The diameter D of the particle was varied between 0.04 m and 0.12 m with incremental steps of 0.01 m. This allowed to include the whole set of particle dimensions that are likely to be found on the track-bed and detected by the resolution of the used GPR system. Finally, the ballast particle and the line source were immersed into perfectly matched layers (PML), to avoid potential edge effects (Fig. 3.6). For each of the above-set diameters, an EM pulse was emitted. The central frequency and the time window were set to be 2 GHz and 15 ns, respectively, in accordance with the manufacturer recommendation for this antenna frequency system. The back-received signals were transformed from the time domain to the frequency domain and the corresponding frequency spectra were analysed.

A more complex numerical scenario with a multi-particle configuration of mono-sized ballast aggregates was reproduced and the relevant EM simulations carried out (Fig. 3.7). The main purpose of these simulations was to consider the actual contribution of the scattering effects and to model the particles arrangement and their EM interaction as close as to the real conditions.
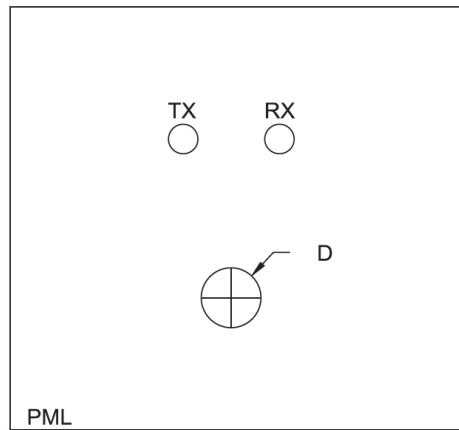
Figure 3.6: Simulation scenario for a single-particle configuration implemented in the gprMax 2D numerical simulator
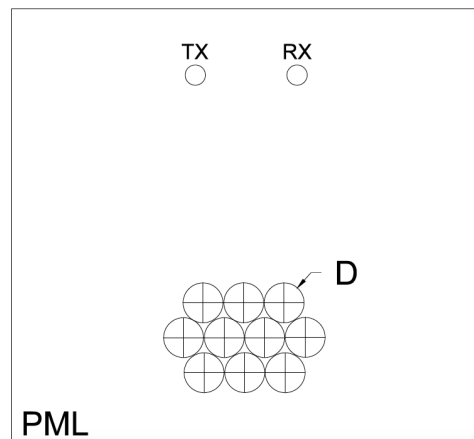
Figure 3.7: Simulation scenario for a multi-particle configuration implemented in the gprMax 2D numerical simulator

To this effect, sets of ten mono-sized round particles were illuminated by the synthetic EM field. The values of the geometric and the electric parameters remained the same as in the single-particle configuration. The relative position of the particles was set randomly to simulate the real-life condition of the ballast aggregates in a track-bed. The monosized diameter of each set of particles was increased progressively from 0.04 m up to 0.12 m.

Track-bed scale

A combined approach that uses the random-sequential adsorption (RSA) paradigm [101] and the finite-difference time-domain (FDTD) technique was implemented for the simulation of the GPR signal. The RSA paradigm was first used for generating random bi-dimensional (2-D) distributions of the compacted
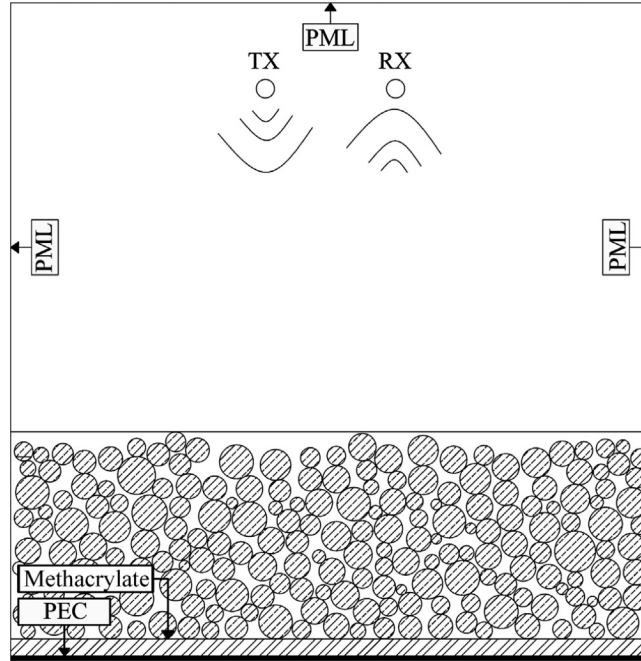
Figure 3.8: The simulation domain representing the methacrylate tank in Fig. 3.2

ballast aggregates, which were schematically represented by a comprehensive set of circumferences with different diameters. The RSA algorithm followed two main steps. As a first mandatory selection condition, the grain size distribution of the circumferences needed to comply with the experimental (actual) one (i.e. Tab 3.1). As a result, the algorithm provided a number of 200 circumferences, on the average, with diameters ranging from 0.025 m and 0.08 m. The second step of the RSA algorithm allowed compacting the circumferences along the vertical axis to ensure the contacts between the aggregates and reach a content of voids equal to 39%. This value was constrained to the actual value obtained from the relevant standard test method performed in the laboratory (Tab 3.1).

Afterwards, the generated 2-D scenario was simulated using the FDTD technique implemented in the gprMax 2D simulator package. The physical structure of the GPR antenna was not included in the model. The real test environment was reproduced by positioning a source of line of current in the free space at a height by the target equal to the actual height of the antenna source. The exact test domain was accurately designed with respect to the size of the tank, the layers composing the investigated multi-phase system (ballast/methacrylate/PEC) and the electric properties of the materials involved (Fig. 3.8). Detailed information about the simulation can be found in [75]. At the current stage of the research, the GPR signals obtained across the full set of scenarios using the 1000 MHz central frequency were simulated.

3.4.3   Data processing

The EM data collected in laboratory have been processed following the standard processing scheme used in section 2.4.3. In particular, the following processing scheme has been applied to the raw signal:

1. *zero-offset removal*

2. *band-pass filter*

3. *time-zero correction*

As far as the band-pass filter is concerned, the cut-off frequencies have been set in order to obtain a relevant bandwidth of 1.5 times the operating central frequency, as a rule of thumb. Since, by theoretical assumption, the central frequencies are expected to differ with respect to the nominal frequency due to the scattering and resonance effects previously addressed, this bandwidth has been set aftwards the central peak of the specific frequency spectrum had been identified.

The synthetic datased, as obtained in controlled environment enclosed by perfect matching layers (PMLs) ensuring no reflections from the domain borders, are affected by no clutter and, accordingly, needed no processing to raise the signal to noise ratio.

3.5   Model calibration

Frequency Domain

Under ordinary conditions, it is likely to observe a frequency spectrum with an amplitude peak value at the nominal central frequency. Nevertheless, in case the size and the dielectric properties of the ballast aggregate particle define a resonance frequency that belongs to the working bandwidth of the system, it is likely to detect the amplitude peak in the neighbourhood of this frequency. With regard to the abovementioned case of the analogous electrical circuit, it is expected to detect amplitude peaks at lower frequencies for larger particle diameters. This is principally related to the fact that the resonance frequency value depends on both L and C, hence, on the grain size of the particle.

Fig. 3.9a represents the frequency spectra of single-particle diameters that range between 0.04 m and 0.09 m. For the sake of clarity with the interpretation of the graph, the spectrum amplitude was normalized to the maximum amplitude

value of each trace. In accordance with the theory, it was observed that the amplitude peak progressively shifted towards lower values of the frequency as the size of the grain increased.

Upper and lower frequency-peak bounds of 2.60 GHz ($D = 0.04$ m) and 1.10 GHz ($D = 0.09$ m) were found, respectively. In the case of particle diameters larger than 0.09 m, the frequency spectra showed peak values centered in the neighbourhood of 2 GHz. This frequency value corresponded to the nominal central frequency of the used GPR system (3.9b).

The results of the simulations are shown in Fig. 3.9. As in the case of the single-particle simulations, it was observed a shift of the frequency spectrum peak as a function of the particle grain size. No resonance effects were observed for the particle diameters ranging between 0.09 m and 0.12 m, in accordance with the theoretical expectations. This was likely due to the fact that nearly no energy was pulsed at lower frequencies than 1 GHz.

As introduced in previous section, the modelling of the grain size of the ballast particles and the frequency spectrum peak of the collected GPR signal was developed to provide a relationship between these two parameters within the allowed frequency bandwidth bounds. To that effect, Fig. 3.11 shows the negative exponential relationship found using the data from the single-grain and the mono-sized multi-grain simulations:

$$P_f = \alpha e^{-\beta D^*} \tag{3.4}$$

where P_f is the frequency of the spectrum peak, D^* is the aggregate characteristic diameter, and $[\alpha, \beta]$ are fitting parameters dependent on the specific configuration. The mean squares fitting curves were characterised by high correlation coefficients R^2, as listed in Tab. 3.4.

Configuration	α	β	R^2
Single-particle	$4.8 \cdot 10^9$	17.20	0.946
Multi-particle	$4.8 \cdot 10^9$	15.70	0.983
Average	$4.8 \cdot 10^9$	16.45	0.964

Table 3.4: Regression coefficients in Eq. 3.4

To analyse the applicability of the above relationship over the multiparticle arrangement of ballast particles with multi-sized grading (i.e., the real-life like condition), let us now express Eq. 3.4 as a function of D^*:

$$D^* = -\ln\frac{P_f}{\alpha} \cdot \beta^{-1} \tag{3.5}$$
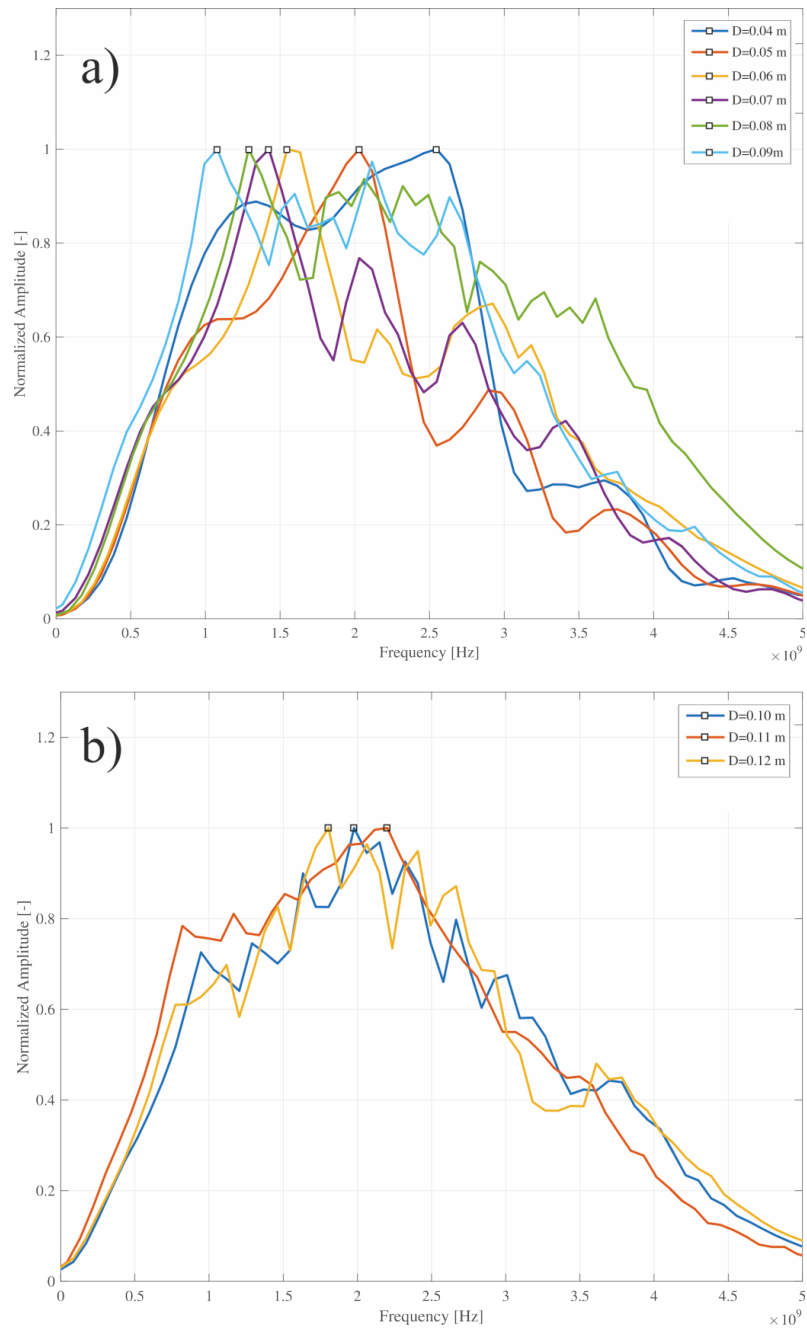
Figure 3.9: Frequency spectra and corresponding frequency peaks obtained from the singleparticle simulations with varying diameters, (a) diameters ranging from 0.04 m to 0.09 m, (b) diameters ranging from 0.10 m to 0.12 m
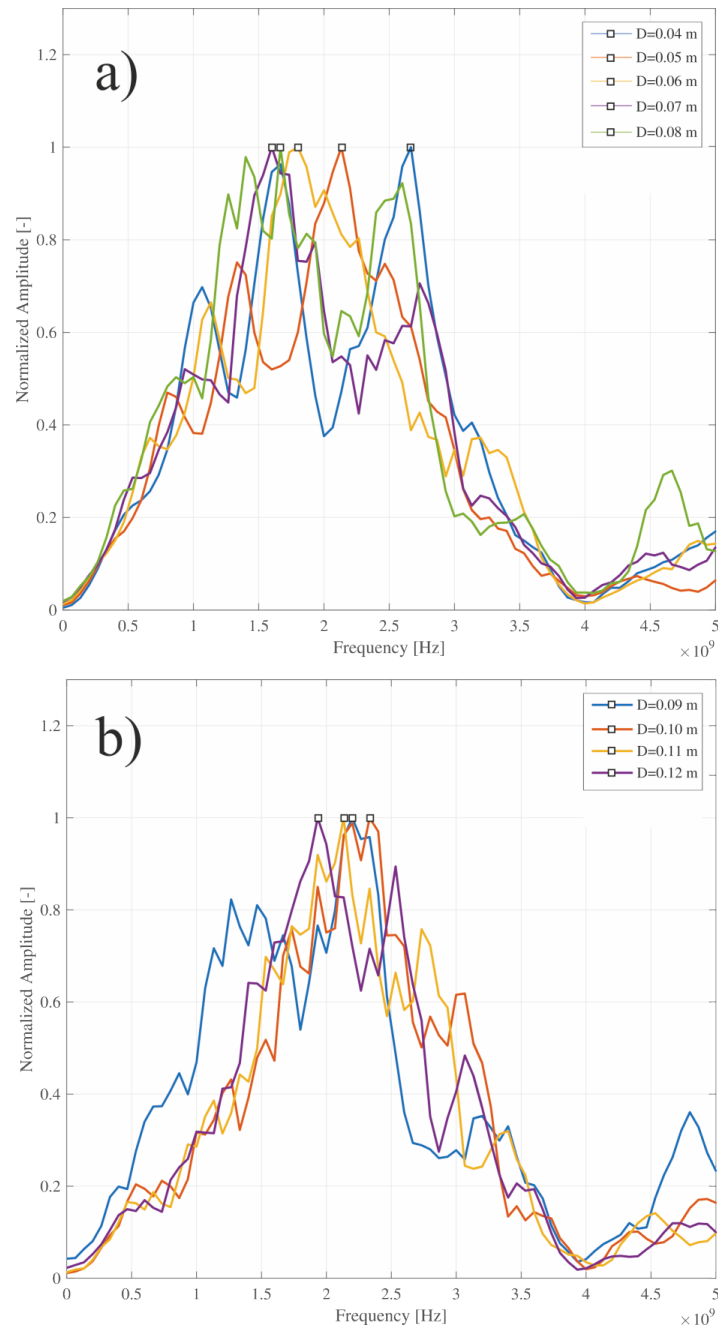
Figure 3.10: Frequency spectra and corresponding frequency peaks obtained from the multiparticle mono-sized simulations with varying diameters, (a) diameters ranging from 0.04 m to 0.08 m, (b) diameters ranging from 0.09 m to 0.12 m
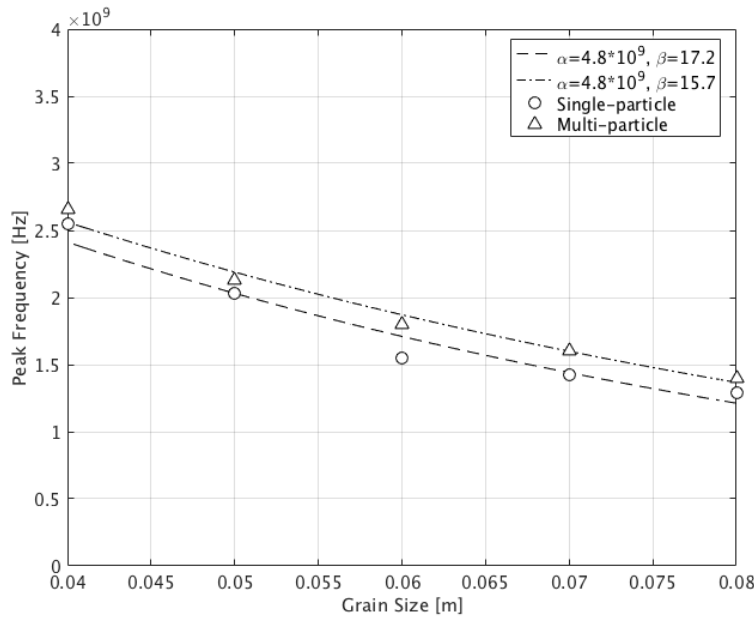
Figure 3.11: Exponential trend lines fitting the frequency peak against the grain size data collected for the single-particle (circular markers) and the mono-sized multi-particle (triangular markers) configurations

Time Domain

At the current stage of the research, the GPR signals obtained across the full set of scenarios using the 1000 MHz central frequency were simulated. In Fig. 3.12 the comparison between the measured and the simulated signals is shown for each combination of ballast and pollutant material. The overall relatively good matching between the radar sweeps indicates a substantial reliability of the used simulation-based approach. In addition, the good agreement between the measured and simulated signals (in terms of time distance between the first (i.e., air-ballast interface) and the last (i.e., ballast-PEC interface) peak) allowed to validate the values of the relative dielectric permittivity computed for the whole set of scenarios using the TDSP technique (Eq. 1.11).

3.6   Results

3.6.1   Frequency Domain

Clean ballast

By observing the frequency spectra of the signals collected over the three clean ballast arrangements, it was possible to detect different behaviours of the signals
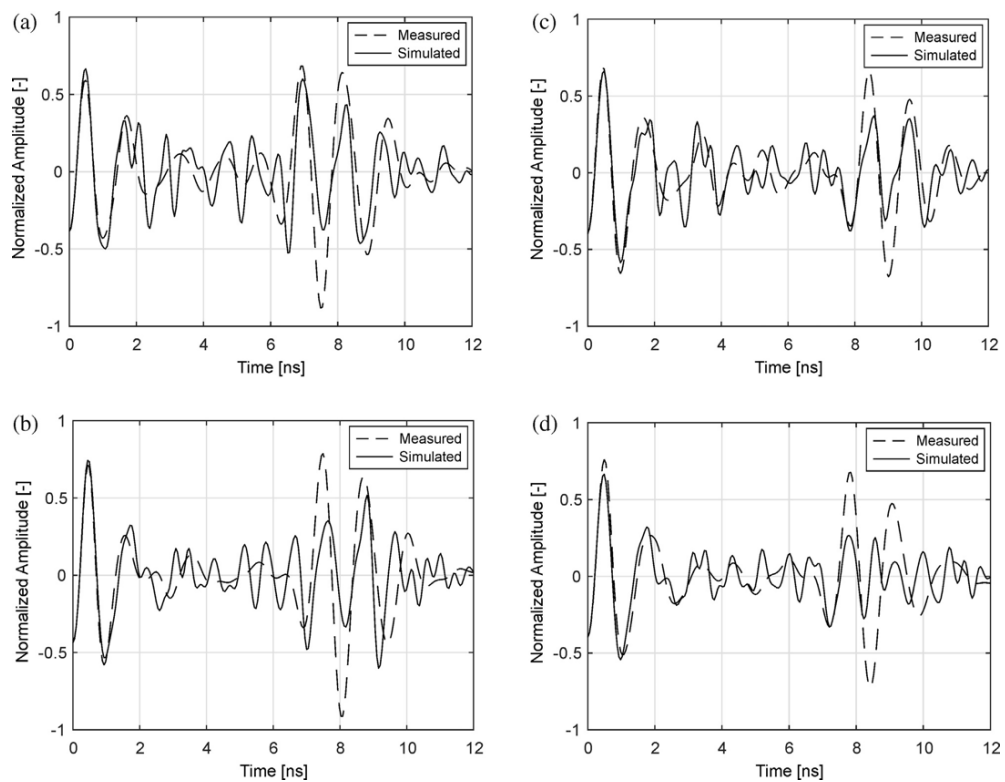
Figure 3.12: Comparison between measured (dashed line) and simulated data (solid line) for the investigated scenarios presented in Tab. 3.3: (a) Scenario 0, (b) Scenario I, (c) Scenario II, (d) Scenario III

collected with the 1000 MHz Horn antenna with respect to those collected with 2000 MHz.

Indeed, the three spectra from 1000 MHz antenna (Fig. 3.13) return a constant peak frequency P_f at 870 MHz, i.e. a distance from the nominal frequency equal to 130 MHz (13%), whereas for the 2000 MHz spectra (Fig. 3.14) a constant P_f value is detectable at 1450 MHz for both the observed signals (note that the last experiment had to be discharged for irregularity in testing procedures). In this latter case, the distance from the nominal frequency is 600 MHz, equal to 27.5% of the nominal frequency.

Hence, what is observed is a slight shifting of P_f away from the nominal frequency, towards lower frequency values. This phenomenon results in a slight measure for 1000 MHz signals (Fig. 3.13), whereas it is more evident for 2000 MHz spectra (Fig. 3.14). Concerning the former case, the frequency shift can be most likely related to the internal coupling of the antenna [20]. In the latter, instead, the extent of this shifting is much greater, which involves a need for interpretation of what is observed.

Actually, such an occurrence is in good accordance with theoretical assumptions in Sections 3.2 and 3.3. Indeed, by applying Eq. 3.5 to the values of P_f derived by 1000 MHz and 2000 MHz datasets, different values of D^* are retrieved, as shown in Tab. 3.5. The values obtained from the regression of multi-particle numerical simulation (Tab. 3.4) were purposely utilised.

Dataset	Observed P_f	D*
1000 MHz	870 MHz	0.109 m
2000 MHz	1450 MHz	0.076 m

Table 3.5: Results from the application of Eq. 3.5 to the dataset collected over clean ballast configurations

Indeed, on the one hand the 1000 MHz dataset returns a diameter D^*_{1000} value (0.109 m) clearly out of the range of diameters that are likely to be observed in the real ballast grading. This confirms that the slight frequency shift can not be due to the geometric features of the material, but rather to internal coupling of the antenna, as previously mentioned.

On the other hand, 2000 MHz dataset returns a D^*_{2000} (0.076 m) which is perfectly included between the range of possible ballast particles diameters. In this case, as numerical simulations demonstrate (Fig. 3.10), the geometric features have significant influences on the shape of the spectra, shifting the P_f towards the resonant frequency.

Figure 3.13: Frequency spectra collected with the 1000 MHz Horn antenna, over the testing box filled up with three different clean ballast configurations

Figure 3.14: Frequency spectra collected with the 2000 MHz Horn antenna, over the testing box filled up with two different clean ballast configurations
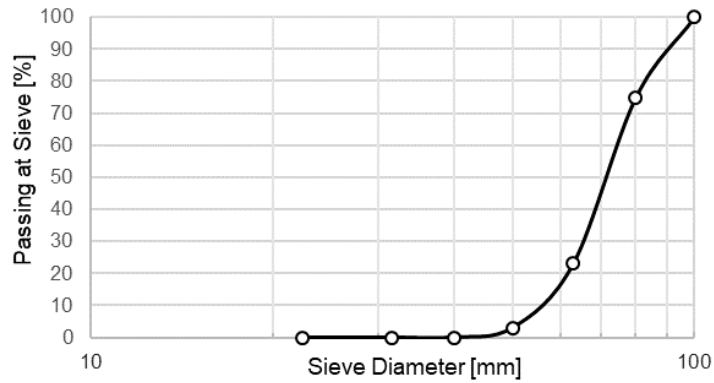
Figure 3.15: Grading curve obtained by sieve method [94] from the clean ballast configuration (CB)

As a result, the difference between the two behaviours can be reasonably related to the specific grading curve of the utilised ballast (i.e. the characteristic diameter D^*), which generates resonant effects at 1450 MHz, being in a central range of the 2000 MHz frequency bandwidth, but only at the border of that obtained by 1000 MHz antenna. In this latter case, indeed, a minor energy is involved in the resonance process, and the main P_f remains located around the nominal frequency, whereas only a minor peak is observed around the resonance frequency, as shown in Fig. 3.13.

Further insights about the definition of the characteristic diameter D^* retrieved from the model application are addressed by observing the ballast grading curve obtained by sieve method [94] from the clean ballast configuration (CB). Comparing the value of D^*_{2000} with the curve of passing material it is possible to conclude that the characteristic diameter D^* recognized by Eq. 3.5 as responsible of the resonance phenomen, represents the 60% of passing material in the grading curve ($P_{60\%}$).

Fouled ballast

In Fig. 3.16 and 3.17 the spectra collected by means of both horn 1000 MHz and 2000 MHz antennas on the total four surveyed scenarios (Tab. 3.3) are reported, respectively. Such an analysis allows to evaluate the influence of the clay pollution onto the spectral behaviour of the ballast-clay mixture.

As far as the 1000 MHz dataset is concerned, Fig. 3.13 shows no specific trend of the frequency spectra in terms of peak frequency P_f. Indeed, as reported in Tab. 3.6, the value of P_f is found to range between 760 MHz and 950 MHz,

i.e. between a distance from the nominal frequency of 5% and 24%, without any regular pattern.

Scenario	Observed P_f	Distance from nominal
0	870 MHz	13%
I	860 MHz	14%
II	950 MHz	5%
III	760 MHz	24%

Table 3.6: Results from the application of Eq. 3.5 to the dataset collected over clean ballast configurations, with the 1000 MHz Horn antenna

Scenario	Observed P_f	Distance from nominal
0	1450 MHz	27.5%
I	1550 MHz	22.5%
II	1750 MHz	12.5%
III	1730 MHz	13.5%

Table 3.7: Results from the application of Eq. 3.5 to the dataset collected over clean ballast configurations, by the 2000 MHz Horn antenna

Concerning the 2000 MHz dataset, a greater variability of the shape of the spectra for increasing fouling level is osberved, as Fig. 3.17 witnesses.

In Tab. 3.7, the values of the observed P_f and the relevant distance from the nominal frequency are reported. A sever difference of the EM behaviour of the mixtures is observed between the scenarios ["0" ,"I"], and the scenarios ["II", "III"], which roughly sort the tested conditions of ballast into "poorly fouled" and "highly fouled". Indeed, a greater influence of renonant effects are observed for the "poorly fouled" scenarios, with a shift of P_f ranging between 27.5% and 22.5%, whereas for "highly fouled" scenarios such effects result negligible, as the distances from the nominal frequency tend to the values observed for 1000 MHz dataset.

It is herein worthy to furtherly discuss some outcomes resulting from the above analysis.

As a result of the spectral analysis of the GPR data collected over the railway ballast with varying fouling conditions, the increasing pollution of the ballast air voids is observed not to affect the EM spectra of the GPR signals collected by a 1000 MHz Horn antenna. Most probably, the differences between the tested scenarios are rather related to both internal coupling effects and environmental clutter generated in laboratory.
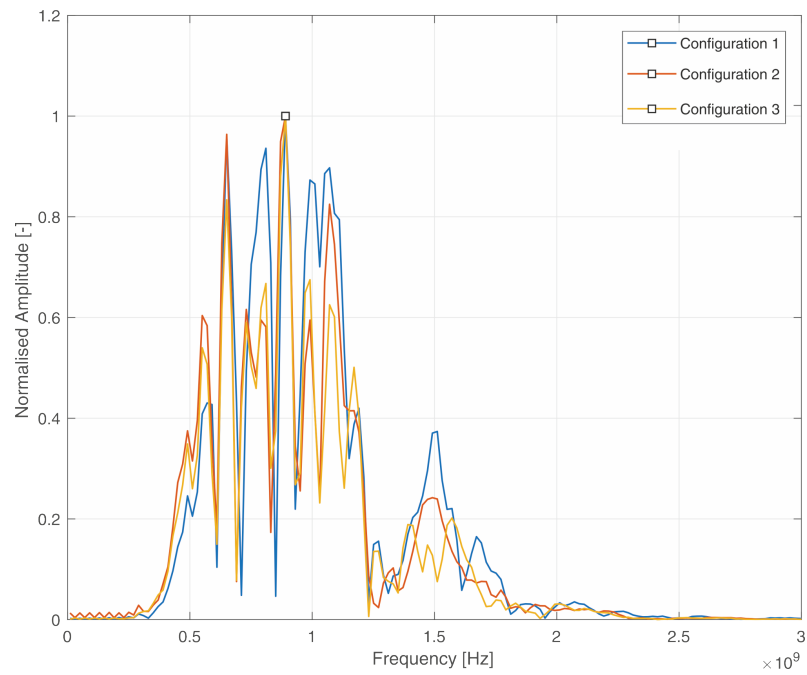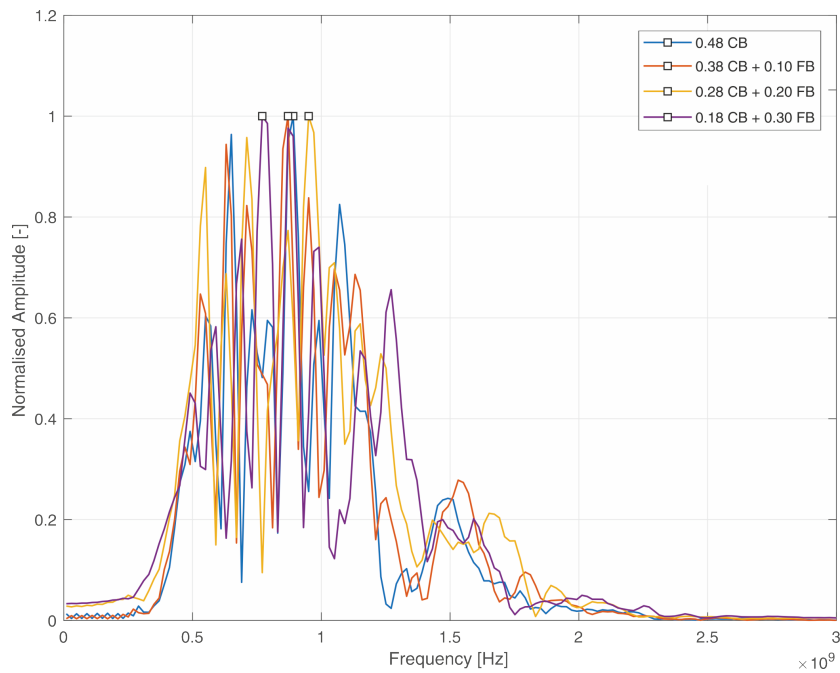
Figure 3.16: Frequency spectra collected with the 1000 MHz Horn antenna, over the testing box filled up with the overall four mixtures, namely, Scenario 0, Scenario I, Scenario II and Scenario III
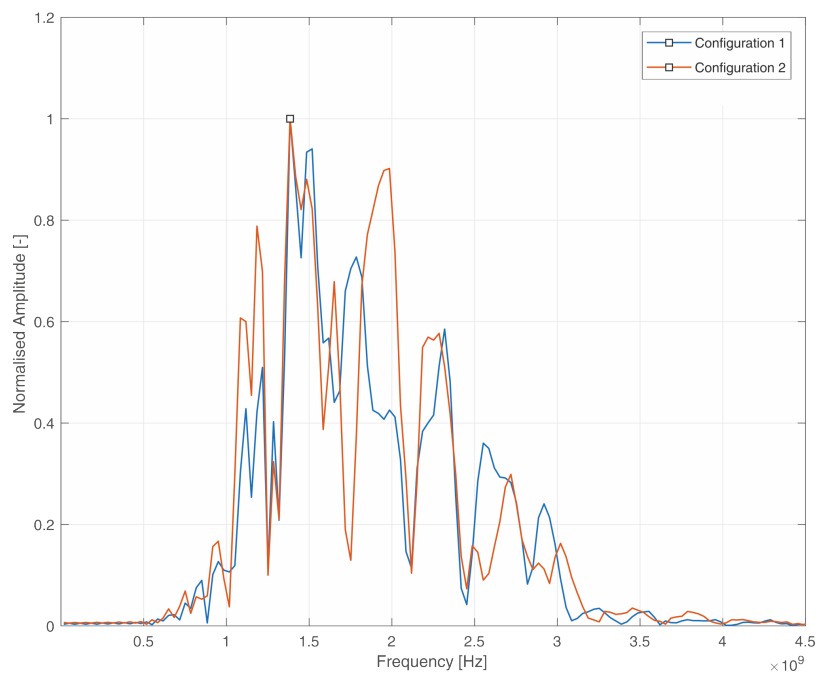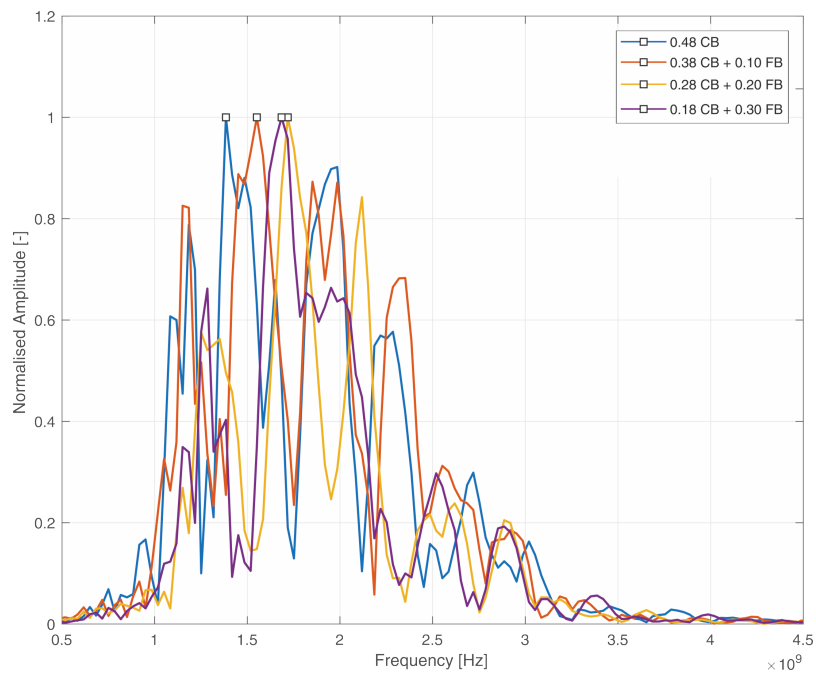

Figure 3.17: Frequency spectra collected with the 2000 MHz Horn antenna, over the testing box filled up with the overall four mixtures, namely, Scenario 0, Scenario I, Scenario II and Scenario III

On the other hand, a significant influence of pollution on the shape of the back-received spectra is observed, for the 2000 MHz dataset. In particular, it is reasonable to assume that, as the presence of polluting soil within the ballast voids increases, the rate of signal energy involved in resonance phenomenon due to the geometric features of the ballast particles gets progressively limited, up to the negligible levels reached for fouling interface located at 0.30 m from the surface.

Such an occurrence evidences the great flexibility of the model. Indeed, as explained in Fig. 3.18, depending on the case, this frequency-based model can be directly utilised for retrieving the geometric features of railway ballast, or invesely employed for inferring about the presence of fouling within ballast voids. Once the GPR data have been post-processed and analysed, a comparison between the observed P_f and the nominal frequency can be performed. Two possibilities can occur:

- The frequency values do *not* correspond or their difference is such that it can not be related to the antenna coupling. Hence, information about the geometric features of the railway ballast composing the track-bed can be inferred. In this case, a cross-checking with a laboratory-derived real ballast grading curve can confirm or exclude a potential fragmentation of the ballast aggregates, which involves a change in grading.

- The frequency values *do* correspond or their difference is such that it can be related to the antenna coupling. Therefore, if the frequency bandwidth had been properly chosen, resonance effects can be excluded. Nevertheless, in this case it is also possible that the extent of the pollution of the ballast voids is such that any resonance process have been compromised, so preventing any shift of P_f. In this case, a cross-checking with an on-site inspection can clearify the actual reason of the EM behaviour.

3.6.2   Time Domain

In order to minimise the stochastic variability of the signals, a number of 100 traces were collected at each reproduced scenario and the average trace was computed. In view of this, one unique (average) A-scan was related to each tested configuration. The average traces representative of the four investigated scenarios are depicted in Fig. 3.19.
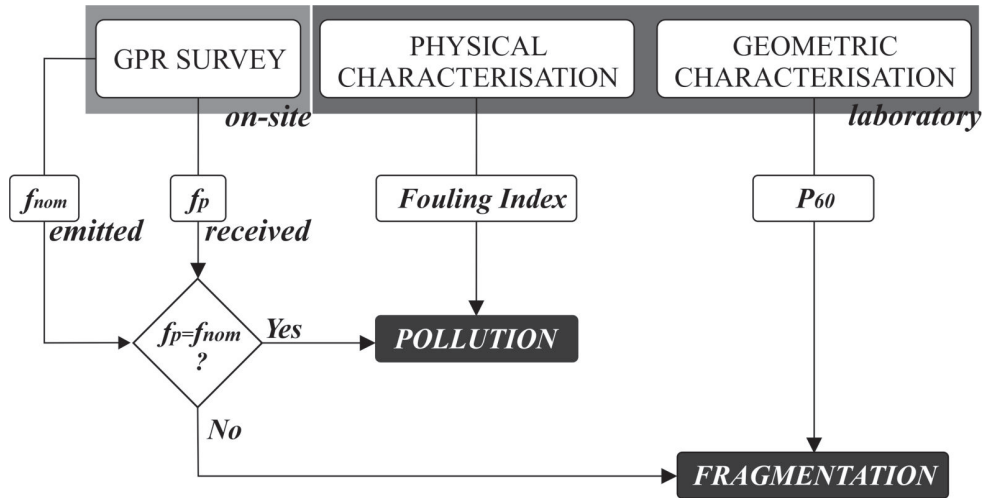
Figure 3.18: Working principles of the frequency-based model for inferring information about fouling and fragmentation of railway ballast
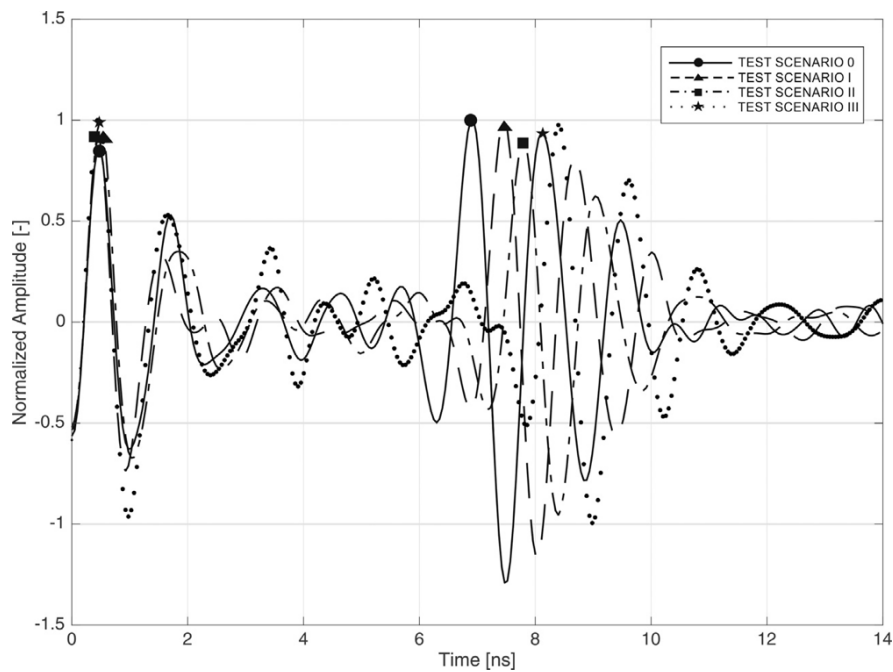
Figure 3.19: Average traces obtained for the four tested scenarios. Line styles indicate the different scenarios, whereas the markers point out the position of the reflection peaks at the interfaces between the air-ballast and the ballast-metal plate

Dielectric permittivity calculated by signal processing methods

Thereby, the value of the relative dielectric permittivity ε_r of the ballast/air/pollutant mix was inferred from each of these traces using differing processing techniques. The time-domain signal picking (TDSP) technique [20] accounts for the time interval between the reflection peaks of the first (air/ballast) and the last interface (ballast/PEC), i.e., the two-way travel time t taken by the EM wave for propagating through the material. Since the thickness h of the tank was known, it was possible to infer the propagation speed $v = 2h/t$, hence, the relative dielectric permittivity as follows:

$$\varepsilon_r = \left(\frac{c_0}{v}\right)^2 \tag{3.6}$$

with c_0 being the speed of light.

The surface reflection method (SRM) [24] is based on the comparison between the amplitude A_0 of the reflection peak from the air/surface interface, and the reference amplitude A_{PEC} reflected by a metal plate (perfect electric conductor (PEC)) larger than the GPR footprint. The relevant relationship is expressed as follows:

$$\varepsilon_r = \left[\frac{\left(1 + \frac{A_0}{A_{PEC}}\right)}{\left(1 - \frac{A_0}{A_{PEC}}\right)}\right]^2 \tag{3.7}$$

In order to reach the maximum accuracy in the estimation of the permittivity, both the amplitudes must be recorded at the same height from the reflector. In this regard, it is worth to emphasize the difficulty to reach a stable value for the height during the operations. This is due to the size and the rough shape of the ballast aggregates which cannot provide a smooth reflection interface.

Dielectric permittivity calculated by theoretical methods

The volumetric mixing formula (VMF) approach was performed to compute the dielectrics using a theoretical multiphase modelling of the investigated scenarios. This method requires the knowledge of both the relative dielectric permittivity $\varepsilon_{r,i}$ and the corresponding volumetric fraction f_i of each ith component of the n-phase mix. These parameters are arranged in the linear combination given by Eq 3.8:

$$\varepsilon_r^\alpha = \sum_{i=1}^n f_i \varepsilon_{r,i}^\alpha \tag{3.8}$$

with α being a geometric fitting parameter, whose values were investigated in the literature [102][103]. In this study, a value of 0.5 was used for the α factor. Tab. 3.8 lists the parameters set in Eq. 3.8. The values of the dielectric permittivity of the ballast (i.e., the dielectrics of the source limestone-derived rock) and the methacrylate were derived from the literature [104]. The dielectric permittivity of the fouling silty soil was computed by the application of the TDSP technique on the GPR data collected within a 0.10 m height layer of this material (laid out within the (same) empty methacrylate tank).

i^{th} component	$\varepsilon_{r,i}$	f_i^0	f_i^I	f_i^{II}	f_i^{III}
Ballast	6.50	0.53	0.53	0.53	0.53
Soil	5.03	0.00	0.08	0.16	0.24
Methacrylate	4.00	0.08	0.08	0.08	0.08
Air	1.00	0.39	0.31	0.23	0.15

Table 3.8: Values of the parameters set in Eq. 3.8 with regards to the four tested scenarios

Methods comparison

Comparisons between the outcomes of each of the above two signal processing-based methods and the VMF are given in Fig. 3.20. The results obtained from the full set of used antenna frequencies are depicted.

With regard to the permittivity estimates by the TDSP technique (Fig. 3.20a), it is worth noting the overall good agreement between the dielectrics achieved in all the case-scenarios across the full set of used frequencies. Values of permittivity comprised between 3.51 and 5.35, which raise consistently with the increasing levels of fouling, were observed. This behaviour agreed with the theoretical assumption, since increasing rates of air voids ($\varepsilon_{r,a} = 1$) were progressively filled with the pollutant material, which was characterised by a higher permittivity value (i.e., $\varepsilon_{r,s} = 5.03$). Thereby, the relative dielectric permittivity of the whole multi-phase system tended to increase.

These results and the overall trend of permittivity values versus the level of fouling were well confirmed by the volumetric approach. The modulus of the incidences of the residuals (i.e., the percentage ratio of the difference between the VMF and the TDSP permittivity values (numerator), and the corresponding dielectrics by the VMF (denominator)) was comprised between 0.10% and 6.90%. In addition and with respect to the trend of the estimates obtained across the four investigated scenarios, the permittivity values retrieved with the TDSP were

overall lower than the corresponding VMF values. Exceptions were the estimates reached with both the 2000 MHz systems in the clean condition (i.e., scenario 0) and the permittivity retrieved with the 1000 MHz GPR in the highly-fouled condition (i.e., scenario III).

On the contrary, the outcomes from the application of the SRM were not consistent with the VMF estimates such as in the case of the TDSP technique. From Fig. **??**b, it is clear how the SRM approach provided lower values of permittivity with respect to both the VMF and the TDSP techniques, and proved to be not suitable to assess both the clean and the fouled ballast condition across all the investigated scenarios.

A possible motivation for this mismatching lies within the amplitude-based nature of the own method and the coarse grain-size and rough shape of the ballast aggregates. Indeed, the SRM relies on the value of the first-peak amplitude of the collected signal, which in turn depends on several factors including the configuration of the air-surface interface.

In this regard, it is worth mentioning that the surface configuration of the four scenarios (i.e., the arrangement of the clean ballast aggregates at the top of the tank) has changed in all the investigated cases, due to the requirements of the testing protocol for laying out the material. In addition, it is well known how the wave-length of the signal is a critical survey parameter mostly in the case of railway ballast, due to the variability of the dimension and shape of the aggregates, as well as of the volume of the air-filled voids (which can vary according to the fouling level).

The consistency between the wavelength of a GPR signal and the dimension of the targets in a railway track bed (e.g., the ballast aggregates or the air voids) can generate considerable scattering patterns and it can affect, amongst the other, the first-peak amplitude of the signal. As a rule of thumb, the lower is the frequency of the investigation, the longer is the signal wavelength, the smaller will be the scattering generated by the ballast aggregates and the air voids. In such a case, the energy extracted from the signal will be lower [71][79].

According to the wavelengths of the two central frequencies used in this study, it can be seen how the highest permittivity values closer to the above VMF (and TDSP) permittivity estimates (which are both expected to well approximate the searched dielectrics), were reached by the 1000 MHz antenna system (Fig. 3.20b). Indeed, this was due to the longer wavelength and the lower sensitivity of this antenna frequency towards the rough shape of the surface aggregates and the dimensions of the air voids. This fact generated less scattering and lower impact on the first-peak amplitude of the signal. Thereby, permittivity estimates much
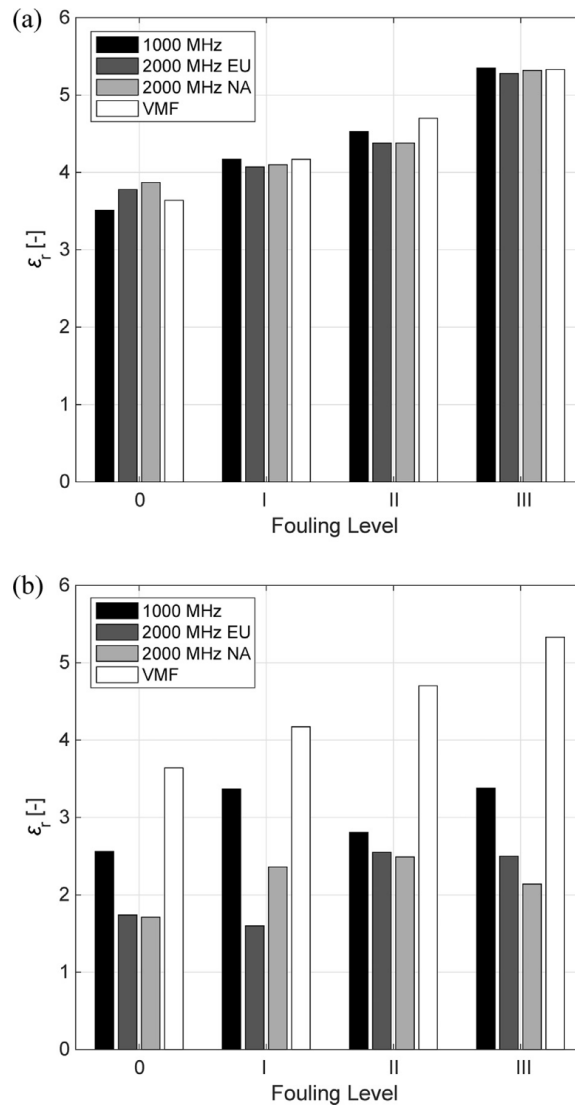
Figure 3.20: Relative dielectric permittivity estimates from (a) the TDSP technique (acquisitions made with the 1000 MHz, 2000 MHz European (EU) and 2000 MHz North American (NA) antenna systems) and the VMF, and (b) the SRM (1000 MHz, 2000 MHz EU and 2000 MHz NA antenna systems) and the VMF

closer to the expected ones were reached.

3.7   Conclusions

In this work, it was analysed the spectral behaviour of 2000 MHz groundpenetrating radar (GPR) signals collected under a multi-stage process in terms of ballast grain size. Furthermore, the modelling of "critical" geometric features of the ballast aggregates and the peak of the frequency spectrum was developed. The study reported on the possibility to retrieve relevant information about the grain size of the ballast aggregates in the rail subsurface layers and the possible segregation of the aggregates under heavy cyclic loading.

To that effect, a bottom-up methodology for the assessment of railway ballast using ground-penetrating radar (GPR – 2000 MHz horn antenna) was developed. The theoretical framework was underpinned by the case of "analogous" electrical and mechanical systems, which were representative of the "ballast aggregates condition" (i.e., the geometric features and the arrangement of the aggregates) against the (electromagnetic) EM field interaction. To validate the theoretical assumptions, a number of finite-difference time-domain (FDTD) simulations of the GPR signal and actual GPR tests in the laboratory were carried out. These tests allowed investigating thoroughly the propagation and the scattering of the EM waves in a ballast layer of a typical rail track-bed. The spectral response of the GPR data in the frequency domain was first analysed in the case of mono-sized single- and multi-particle configurations of round-shaped ballast aggregates with different diameters and electric properties consistent with literature references. Afterwards, the numerical scenario was rendered more complex by using multi-sized particles under compaction conditions close to reality.

Overall, the spectral analyses from both the simulation cases and the laboratory tests confirmed a shift of the frequency spectrum peak as a function of the dimensions of the aggregate particles, as it was expected by the theoretical assumptions. In this regard, it was proved a decreasing trend of the peak of the frequency spectrum as the value of the diameter increased in the 0.04÷0.09 m range. The simulations from the simplified mono-sized multi-particle scenarios turned out to provide more irregular shapes of the frequency spectra than the single-particle simulations. In addition, the range of applicability of the resonance method was proved to be slightly different among the single and the multi-particle simulations. This was likely due to the scattering and the surface effects that arose from the EM wave propagation in the multi-particle model. With regard to the

real-scale simulations and the laboratory investigations, comprehensive geometric parameters (i.e., equivalent diameters of the aggregates) representative of the grain size distributions of the ballast were set using a circular and an elliptic approximation of the aggregates shape, respectively.

Hence, experimental relationships between the aggregate diameter and the peak of the frequency spectrum were found from the results of the single- and the multi-particle simulations. The modelling of the multi-particle simulation scenarios was developed to underpin the proposed theoretical assumptions and to infer information about the grain size of the ballast aggregates from the real-scale simulations and the laboratory (actual) GPR tests. Overall, the experimental model tended to underestimate the computed equivalent diameter. In addition, the elliptic approximation used for the shape of the ballast aggregates (i.e., the case of the laboratory GPR tests) performed better, with percentage errors lower than 20%.

Further theoretical investigations might be aimed at developing the proposed frequency-based methodology by the use of stepped-frequency continuous-wave (SFCW) GPR systems. In addition, the effectiveness of the model could be tested against different conditions of fouling, e.g., in the presence of fine material that rises from the foundation level and fills the inter-particle voids. To that effect, dedicated simulations and real-life tests could be developed following the methodology discussed in this study.

As far as the phyisical investigation of the track-bed is concerned, this work reports on the ground-penetrating radar (GPR)-based assessment of railway ballast which was progressively "polluted" with a fine-grained silty soil material. The experimental setup was designed to represent the real-life scenario of a ballast layer within a railway track bed. To this purpose, a methacrylate square-based tank sized 1.47 m x 1.47 m x 0.48 m height (inside dimensions) was manufactured and filled with clean ballast aggregates.

The air-filled inter-particle voids were progressively "polluted" with a fine-grained silty soil, classified as A4 according to the AASHTO soil classification. Four levels of fouling within the ballast aggregate particles were reproduced. The GPR tests were performed at each fouling step using pulsed GPR systems equipped with differing air-coupled antennas of 1000 MHz and 2000 MHz central frequencies.

The relative dielectric permittivity values of the ballast-silty soil mixes were retrieved using two signal-processing-based methods, i.e., the time-domain signal picking (TDSP) technique and the surface reflection method (SRM), and one

theoretical-based model, i.e., the volumetric mixing formula (VMF).

The results showed that the values of the dielectric permittivity increased with the level of fouling and were comprised between 3.51 and 5.35. The comparison between the above three models proved that the SRM was not suitable for assessing the permittivity of the materials under investigation across the range of the used antenna frequencies. Good matching was found between the permittivity values assessed by the TDSP technique and the VMF approach. In particular, the best agreement was observed in the case of data collected with the 1000 MHz antenna system.

Chapter 4

Advanced survey procedures

For both road and applications, as shown in Chapters 2 and 3, prediction models have been proposed. These models were calibrated using part of the dataset collected within the context of dedicated experimental activities. These activities were carried out in both laboratory and real life environments. Numerical simulation was used to support the evidence of these experimental activities. These activities were carried out in both laboratory and real life environments. Numerical simulation was used to support the evidence of these experimental activities.

The calibrated models have been finally tested against the remaining dataset for validation purposes. The encouraging results proved the viability of both the proposals for effective network-scale monitoring campaigns.

In Sections 2.4.2 and 3.4.1, the testing equipment used for the surveys are described. This Chapter provides some procedural insights about potential integration between NDTs for surveys of the transport assets at the network level.

4.1 Roads: GPR and Curviameter

The experimental-based model discussed in Chapter 2 relies on the use of high-frequency GPR systems equipped with air-launched antennas. These systems work at the traffic speed as they are mounted on an instrumented vehicle and suspended in the air without any contact with the pavement surface. These systems ensure a very high productivity in terms of roads' stretches analysed over short time spans, that might reach up to hundreds of kilometres investigated per day.

It is known that the travel speed of the EM waves propagating through a layered medium needs to be calibrated by knowledge of the actual thickness of

the layers. In this study, this information has been retrieved by design charts. For a higher accuracy, it might be assessed by digging holes or coring the pavement structure. As a drawback, the need for corings would turn the methodology into a quasi non-destructive method. Hence, this would imply a significant increase of the survey costs and provide only a discrete knowledge of the actual thicknesses.

Furthermore, the calibration stretch equal to $\sim 10\%$ of the total length of the inspection required by the model, involves the use of a mechanical-based testing equipment for ground-truthing. To this aim, the LFWD non-destructive testing equipment has been used in the case presented in this Chapter.

Despite the substantial advantage held by this equimpment - mostly related to the easier handling of the equipment within the test site, and the relatively limited commercial cost – the LFWD has proven several disadvantages (i.e., Section 2.4.2). Indeed, the reliability of the results showed a significant affection caused by the test conditions. This is exacerbated by the difficulty to comply with the condition of of a perfect vertical drop of the falling weight, which is witnessed by the extent of the trimmed-off data. Furthermore, the deflection basin collected with the LFWD hardly reaches the depth of 30 cm, as reported in [44]. This could represent a practical issue in case of thick base layer. Both of the above drawbacks might be easily overcome by using a FWD, which can be towed also by a vehicle for faster acquisitions.

In addittion, both the equipment show further intrisic disadvantages that limit the overall suitability for more extended surveys at the network level. In fact, the FWD requires the equipment to stand in a specific test position for some time. Hence, if we assume an estimated time for carrying out a single measurement as equal to 1 minute, an overall amount of daily tests in around 200 can be envisaged. The fastest version of the FWD method of data collection (i.e., the Fast Falling Weight Deflectometer -FFWD-) reduces the time needed for a single test of 45%, thereby reaching a daily productivity of 2400 measurements. Besides, FWD testing procedures hardly comply with traffic operations and require the closure of a lane where the measurements are being collected.

The Curviameter (Fig. 4.1) is a deflection-based survey device that partially makes up for such drawbacks [105][106]. The functioning principles of the Curviameter (Fig. 4.2) rely on the use of a set of geophones to measure the velocity of vertical displacement of the road pavement, exerted by the passage of the rear axle of a truck.

Typically, three geophones are fixed on a chain that lays over the investigated surface. Each sensor, alternately, actively measures the deflection bowl at a particular position, while the truck proceeds forward over 4 meters, at a constant

Figure 4.1: The Curviameter testing system
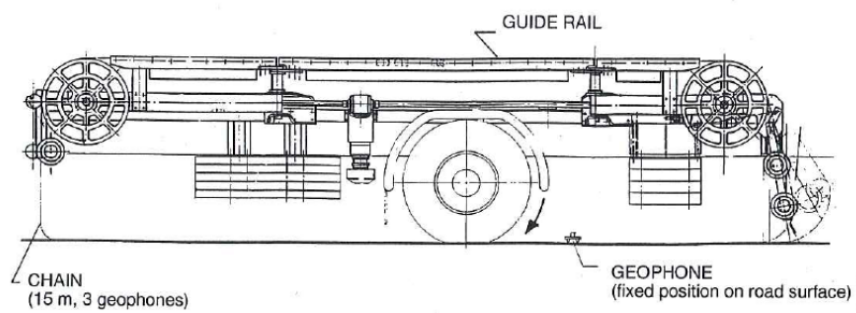
Figure 4.2: Scheme of a Curviameter [104]

speed of up to 18 km/h. The discrete spacing between two consecutive deflection measurements is 5 m.

The active geophone stores a discrete graph of 100 points, which by post-processing returns in a complete deflection bowl. The on-board software is capable of providing in real time the maximal deflection (D_{max}), the radius of curvature (R_C) of the deflection bowl, and the indicator λ, so defined:

$$\lambda = \frac{\mu}{h} \tag{4.1}$$

with μ being the opening width of the deflection pattern measured at half the height of D_{max}, namely h.

Once the deflection bowl is calculated, back-analysis procedures can be applied in order to retrieve the moduli of elasticity of the layers composing the pavement.

An experimental activity has been planned and carried out in the District of Madrid and Guadalajara (ES), in order to evaluate the feasibility of an integration of GPR and Curviameter for raising the current productivity of the Curviameter from 18 km/h up to the maximum traffic speed allowed by local traffic rules. This would occur by integrating a high-resolution air-launched GPR system in the Curviameter lorry, and by implementing the self-calibrating model presented in Chapter 2.
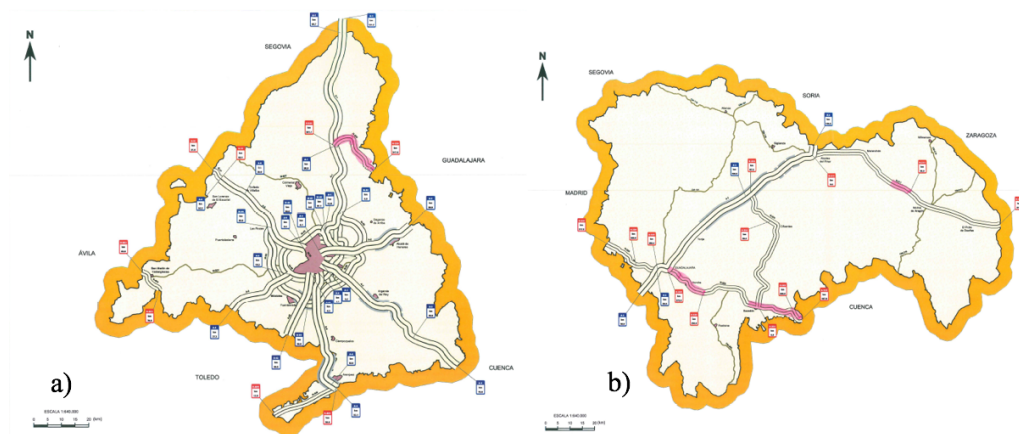
Figure 4.3: The investigated road stretches in the District of a) Madrid and b) Guadalajara

The experimental campaign, organised within the context of a collaboration between Roma Tre University, IDS Georadar S.p.a. and Euroconsult Nueva Tecnologias S.A., different Roadways have been surveyed by both GPR and Curviameter devices in the District of Madrid and Guadalajara.

In particular, the two-lane Roadways N211 and N320 characterised by typical flexible pavements, have been investigated. Geometrical information about the flexible pavements were furnished by local Administrations, as reported in Tab. 4.1.

Road	Pavement		
	HMA (m)	Bond Base (m)	Loose Base (m)
N211	0.12	-	0.50
N320	0.20	-	0.45

Table 4.1: Geometric configuration of the pavement by Aministration Inventory Database

The GPR test system ulitised in the road surveys consisted in a pulsed GPR system equipped with three Horn Antenna manufactured by IDS Georadar S.p.A., that was mounted onto a vehicle by means of a dielectric support, as shown in Fig. 4.4. More specifically, a 1000 MHz, a 2000 MHz and a low-powered 2000 MHz (suitable for North American regulations) have been employed.

Curviameter tests were performed by Euroconsult Nuevas Tecnologias S.A. using a CURVIAMETRO MT-5000.2 (Fig. 4.4).

The GPR systems have been set to collect a trace every 0.021 m, whereas the Curviameter measured the deflection basin with a 5 m interval. The two datasets have been matched by means of GPS coordinates.

The transverse allignment of GPR and Curviameter measurements within the investigated lane has been ensured by visually alligning the Curviameter sensing chain with the center of the instrumented vehicle, corresponding to the GPR antenna.

The collected dataset has been finally post-processed consistently with the procedures described in Chapter 2. The travel speeds of the propagating EM waves has been calibrated along the scanned stretches by means of corings (e.g., Fig. 4.5). The model was calibrated randomly selecting 10% of the total scanned length. Part of the preliminary results obtained by applying the experimental-based model to the dataset are presented in Fig. 4.5. Promising outcomes have been achieve also in this case, confirming the good performances of the this approach in predicting the mechanical properties in flexible pavements.

Note that local evident mismatches, such as reported at km 331,900 (Fig. 4.5b) and km 334,850, are related to the presence of particular elements (bridges, services, etc.) that can produce different geometrical configuration of the pavement, and a consequent misinterpretation by the model.

(a) *The employed radar system.*   (b) *The employed Curviameter system.*

Figure 4.4: The test equipment

As far as the procedural insights are concerned, the high frequency horn antennas allowed at complessively collecting data for roughly 120 km of pavement in the two days of tests. Even though the Curviameter was found to generate a very limited interference with road traffic, its productivity resulted significantively lower than that of GPR. Indeed, in the same time, 40 km have been tested by means of Curviameter, which is boradly equal to 33% of the GPR scans.

In such a framework, using GPR for the comprehensive surveys at the network level, and Curviameter for only collecting ground-truth data necessary for

Figure 4.5: A core extracted within Roadway N320, Madrid (ES)
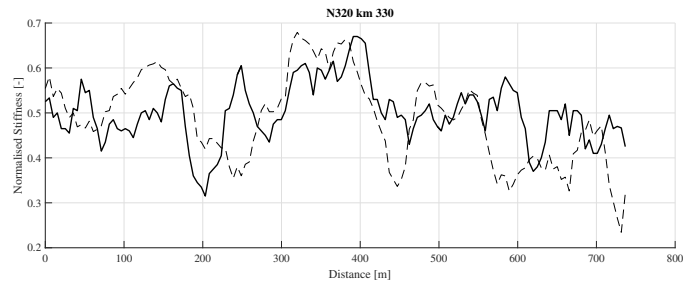
(a) *Roadway N320, km 330.*
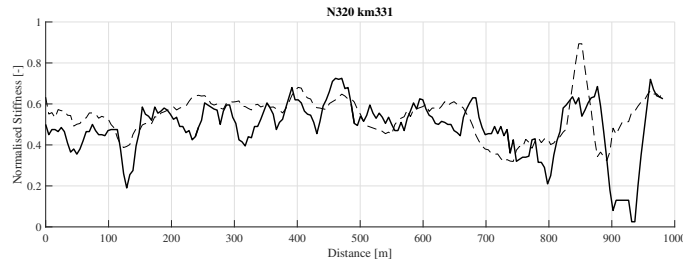
(b) *Roadway N320, km 331.*
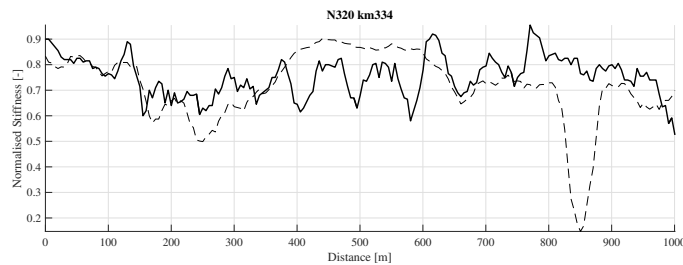
(c) *Roadway N320, km 334.*
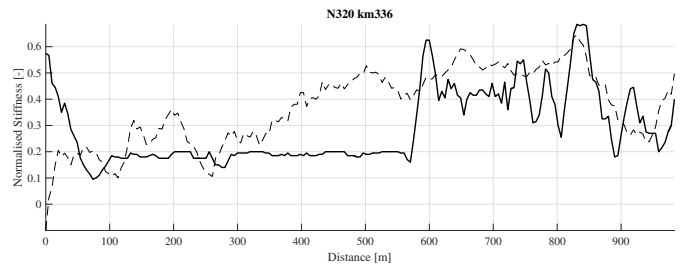
(d) *Roadway N320, km 336.*
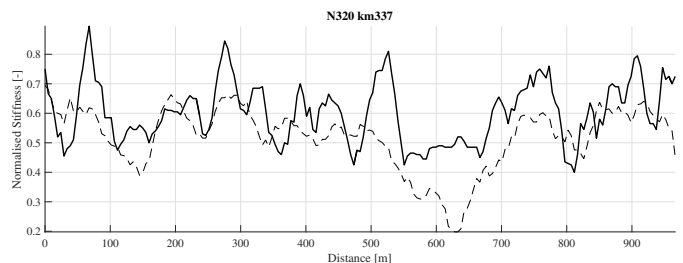
(e) *Roadway N320, km 337.*

Figure 4.6: Result of the application of the prediction model to part of the dataset collected within the experimental activity. The stiffness observed by Curviameter is plotted in solid line, whereas the dashed line represents the predicted values

calibration porpuses, would be a solution capable of maximising the productivity of the survey processes, while minimising the interference with local traffic. As a confirm, considering the actual need of the model for a calibration stretch (10%), it was possible to run the calibration of the model over a total of 4 out of the collected 40 km.

4.2   Railways: GPR and Image Analysis

In Chapter 3, a novel frequency-based approach for inferring information about geometric and physical properties of the ballast composing a railway track-bed has been presented. This method basically works by comparing the emitted and received frequency spectra obtained by GPR survey, and searching for potential shift of peak frequency from the nominal value.

The frequency of the spectrum peak, when different than nominal, has been related to a characteristic diameter of the ballast aggregates, representative of the 70% passing at the sieve method. The presence of great amount of fine particle filling the intergranular voids was found to limit the influence of geometrical properties on the frequency spectra, tending to return the peak frequency towards the nominal value.

Accordingly, the model can be applied with a double scope. Indeed, if the geometrical information retrieved by spectral analysis do not correspond to a reference grading curve, a change in the aggregates size, and hence fragmentation, could be occurred. On the other hand if the peak frequency expected by grading curve is not observed in the spectral analysis, but rather the received peak frequency has returned towards the nominal value, an high level of fouling is well expected.

In both cases, it is of crucial importance to have reliable information (i.e., grading curve) about the actual geometrical condition of the ballast aggregates, as a reference for assessing both the fragmentation and fouling analysis. Such an information can be provided by the companies or administrations managing the asset but, most often, are not available at all. In this case, on site inspection and consequent laboratory analyses are required. However, such an approach appears as highly time- and cost-expensive and, in addition, provides only a very discrete knowledge about the grading at the scale-network.

As a potential solution to the problem, an ad hoc image analysis algorithm was developed in order to infer the geometric properties (grading) of the ballast by photographic survey.

Figure 4.7: Plan view of the ballast-filled methacrylate tank, from Test 1. (a): the raw picture taken with a photocamera suspended in the air above the center of the formwork. (b): the binary image obtained from the processing of the raw picture.

The same laboratory set-up presented in Section 3.4 has been utilised. In particular, aerial picture to the planar view of the methacrylate thank have been shot by means of a high definition camera, for three different spatial distribution of the same railway ballast sample namely, Test 1, Test 2 and Test 3.

The proposed algorithm is composed of two main steps. Firstly, a threshold to the RGB image is set, such that the original image is transformed into a binary matrix. The pixels of this matrix are filled with "ones", if they exceed the above set threshold; else (pixels below the threshold), the pixels are filled with "zeroes". Hence, morphological operators are required for cleaning up the image from the smaller objects, which can be attributed to clutter rather than to the actual size of the ballast particles. In Fig. 4.7 the planar picture of the ballast configuration from Test 1 (Fig. 4.7a) along with the corresponding binary matrix (Fig. 4.7b), are reported.

In the second step, the algorithm is aimed at recognising the different particles. This is a relatively complex procedure, which is highly dependent on the quality of the photography. Particularly, the condition of lighting has great influence on the reliability of the process. Indeed, since the system searches for zero-filled areas (i.e., void cells) within the analysed matrix in order to define the size of the ballast particles, the light contrast of the raw image is a crucial variable that may affect the reliability of the proposed algorithm. In view of a poor contrast of the raw image, the algorithm may fail in detecting the contour of the particle; hence this may be not recognized as a single particle. To prevent this failure, a threshold to the maximum admitted size of the recognized particles was arbitrary set.
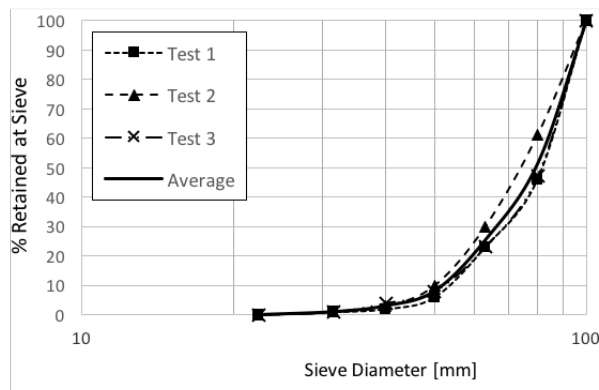
Figure 4.8: Grading curves obtained from the image analysis run on Test 1 (square-marked), Test 2 (triangle-marked), Test 3 (cross-marked), and the curve interpolating the average values (solid line)

Thereby, the algorithm detects only the fraction of particles that complies with the above set filters. The reliability of this approach used for the partition of the dataset was proven. The comparison of the grain size distribution retrieved by means of the discussed algorithm with that defined through the sieve method (see 3.4.1), performed in the laboratory environment, is shown in Fig. 4.8. The normalised root mean square deviation (NMRSD) is equal to 8%, 14% and 15% for Test 1, 2 and 3, respectively.

The final outcome of this second step is a sequence of recognized particles with corresponding areas expressed in number of pixels. To outline the grading curves from the analyses of the images, the areas of the ballast particle has been converted from pixels to cm^2, by taking the known dimension of the methacrylate tank as scale reference. Subsequently, a specific diameter was assigned to each particle by referring to the equivalent virtual circle-shaped particles (with same area of those captured from the image analysis).

Finally, the volume of the aggregates was calculated after assuming the aggregate particles as 3-D spheres. To pass from volume to weight units, it was used the information on the density of the ballast aggregates, as per the aforementioned laboratory tests.

Chapter 5

General Conclusions & Recommendations

The numerical and experimental results discussed in the previous Chapters are summarized here. This Chapter concludes the thesis and it provides recommendations for practical applications and usage in the fields of interest.

5.1 Conclusions

The first research objective consisted in finding an appropriate electromagnetic model capable to assess the mechanical response of road flexible pavements by means of air-launched high-frequency GPR systems. The findings might be of interest for administrations and managing companies in order to manage more efficiently their asset maintenance programs. From Chapter 2 we can conclude that:

- The model uses ground-truth data of road stiffness inferred from LFWD as well as geometric and physical information of the pavement structure derived from a GPR system equipped with high-frequency horn antennas.

- The geometric thickness of the base layer and the presence of clayey soil material rising from the subgrade up to the shallower layers of the pavement are found to be key factors affecting the whole stiffness of a pavement superstructure.

- A rate of 10% of the data taken over the total length of the road investigated is a sufficient percentage for the calibration of the proposed experimental-based model. This is an important outcome, as it allows to use the available

non-destructive testing equipment for assessment of the stiffness of road pavements (low productivity) for a limited extent of the road network.

- The model well matches the ground-truth data of stiffness for the investigated flexible pavement, with a NRMSD equal to 0.13.

- By averaging the data every 50 m and by sorting the results into dedicated stiffness classes, it is possible to qualitatively describe the mechanical behaviour of a pavement and to single out the areas of major decay.

The second main purpose of the study is to investigate the potential of GPR for the evaluation of the geometric and physical properties of ballast railway track- beds. The proposed model uses the data collected by air-launched GPR antennas mounted onto the railway convoy, in both the frequency and the time domains. The model is based on the comparison between the GPR emitted and back-received signals, in the spectral domain. As a result, a relationship between the peak frequency of the back-received spectrum and the geometric features of the ballast is found. Moreover, a dielectric assessment of the ballast mixes (i.e., clean aggregates with different levels of silty soil "pollutant" material) was carried out in the laboratory environment. The achieved results might be relevant for the development of an efficient track-bed monitoring program. Both the fragmentation of the aggregates and fouling of the ballast were assessed. From Chapter 3 we can therefore conclude:

- A shift of the peak frequency is related to resonance effects. These effects are generated by specific geometrical features of the ballast aggregates.

- The presence of fouling within the intergranular voids progressively inhibits the rate of energy involved in the resonance process. This implies the back-received spectrum to equal the emitted one.

- By spectral analysis, the geometric feature influencing the position of the peak frequency of the back-received spectrum can be roughly related to the 70% of the passing material in a sieving test, (P_{70}).

- To achieve unique results in terms of the assessment of the grading and the ballast pollution, a reference assessment of the actual conditions of the track-bed is advised.

In Chapter 4, procedural insights about further integrations of GPR and other NDTs for the investigation of the transport asset at the network level are given. In more detail, we can conclude:

- The use of Curviameter for calibration porpuses allows to reach a higher productivity in terms of time needed for testing, while reducing at minimum the interferences with local traffic.

- The suitability of Curviameter for flexible pavement investigations turns out to be substantially higher with respect to LFWD. This is confirmed by the significant lower extent of the data processing required. Furthermore, the deeper deflection basin generated by the Curviameter allows for an application of the model over the thicknesses of the base courses, as opposed to the LFWD. Indeed, the thicknesses of a base layer are usually higher than the depth of influence of the LFWD.

- The use of the image analysis technique exhibits good performance in providing an estimation of the grading curve of the railway ballast material. The proven viability of this methodology paves the way for relating a single GPR trace to the grading of ballast at specific sections of the track-bed. This is a fundamental condition for achieving a viable application of the "spectral analysis" methodology presented in Chapter 2.

5.2 Recommendations

The main object of this study is to investigate the integration of NDTs for assessing the mechanical properties of road and railway superstructures. In accordance with the preliminary assumptions, the capabilities of non-destructive testing methods to identify the causative factors leading to decay have been therefore investigated. More specifically, the pavement stiffness has been related to geometric weaknesses as well as to the presence of fine materials (rather than to the actual distress recognition). On the other hand, the condition of the track-bed has been related to the fragmentation of the ballast aggregates as well as to the fouling of the track-bed (rather than to the observed rails deformation).

However, the amount of the experimental equipment used in this study and the dimension of the collected dataset require a number of final recommendations. These can be useful to follow prior to the practical application of the presented models at the real-life scale. More specifically, in the case of road flexible pavements, the following recommendations can be listed.

- The parametric model has been calibrated by means of LFWD data. It is worth noting that, as a mechanical testing device for bound layers, LFWD is less acknowledged than FWD. However, the model is set to re-calibrate

with reference to the selected calibration stretch and to the input ground-truth data.

- No correction factors due to the temperature of the material during the experimental tests have been considered, since the temperature recorded was approximatively equal to the reference value, by manufacturer indications. A further investigation of the influence of the temperature parameter on the model is therefore expected.

The following recommendations can be listed in the case of railways:

- The resonance effects induced by the geometrical features of the ballast are only triggered if the characteristic frequency belongs to the operating bandwidth of the emitted signal. This implies that an incorrect selection of the central frequency of the used GPR system might prevent this detection. As a general recommendation, a central frequency comprised between 1500 MHz and 2500 MHz should avoid any detection problem.

- The matching between the emitted and the back-received spectrum is related to three likely interpretations: i) the pollution of the voids inhibits the resonance effect; ii) the resonance frequency does not belong to the spectrum bandwidth; iii) the effective geometric features of the aggregates determine a peak frequency equal to the nominal frequency. In order to identify the most likely interpretation, an additional GPR survey with a different central frequency of investigation is suggested.

Summary

This thesis investigates the potential application of non-destructive testing (NDTs) methods within the context of predictive maintenance protocols. In particular, the integration of ground-penetrating radar (GPR) and other NDTs for the assessment of the mechanical response of both road pavements and railway track-beds have been investigated.

In this regard, the study is aimed at proposing experimental-based models for the early-stage detection of decay areas within a transport network. This might allow to plan a high-priority maintenance scheme in order to prevent further development of the damage.

In Chapter 1 it is discussed the theoretical background on which the models are based. Accordingly, a general overview of the electromagnetic fundamentals and the GPR principles is given, along with an outline of the elastic theory at the foundation of the deflection-based testing equipment.

Then, the main road applications are described in Chapter 2. In particular, a parametric model taking as input the thickness of the base course and the clayey material contribution, calculated by GPR. For calibration porpuses, ground-truth data collectd by Light Falling Weight Deflectometer (LFWD) over a 10% of the investigation length have been used. The model has been tested through an experimental campaign held in the District of Rieti, Italy, where 1500 m of a rural road have been surveyed by both GPR and LFWD. The application of the model resulted in promising results. According to the main goal of the study, a *ad hoc* qualitative approach has been proposed, which allows at easily detect the low-stiffness area among the surveyed asset.

Chapter 3 deals with the railway application. In this case the main objective of the study was to propose a methodology capable of characterising the geometric and physical properties of the ballast aggregates composing the railway track-bed. A frequency-based model was purposely proposed. The model is based on the comparison between the emitted and back-received signals, collected by on-site GPR surveys. The features of the ballast grading curve have

been related to the peak frequency of the back-received spectra, according to the resonance and scattering processes triggered when the aggregates are illuminated by an EM field. To calibrated the model, a set of finite difference time domain (FDTD) numerical simulations has been run, whereas the validation of the model has been performed by realising an *ad hoc* experimental scenario in laboratory environment, for various material fouling level. As a result, ballast fouling extent was found to limit the triggering of the resonance effects.

In Chapter 4, further integrations of GPR and other NDTs are presented, with particular reference to the procedural insights. Specifically, promising results have been obtained from the coupling of air-launched GPR systems with Curviameter and Image analysis for road and railways inspections, respectively.

Bibliography

[1] Roja F.,L., *Filling potholes: macroeconomic effects of maintenance versus new investments in public infrastructure*, Journal of Public Economics, 87, 2281-2304, 2003

[2] Gyamfi, P., Gutierrez, L., Yepes, G., *Infrastructure Maintenance in LAC: The Cost of Neglect and Options for Improvement*, 1, Latin American and Caribbean Technical Department, The World Bank, 1992

[3] Devarajan, S., Swaroop, V., Zou, H., *The composition of public expenditure and economic growth*, Journal of Monetary Economics, 37(2), 313-344, 1996

[4] Karaa, F.,A., *Infrastructures Maintenance Management System Development*, Journal of Professional Issues Engineering, 115, 422-432, 1989

[5] Maser, K., R., *Inventory, condition, and performance assessment in infrastructure facilities mnagement*, Journal of Professional Issues Engineering, 114(3), 271-275, 1988

[6] Bengtsson, M., *Condition Based Maintenance System Technology-Where is Development Heading?*, Proceedings of the 17th European Maintenance Congress, AMS (Spanish Maintenance Society), Barcelona, Spain, 2004

[7] Bevilacqua, M., Braglia, M., *The analytic hierarchy process applied to maintenance strategy selection*, Reliability Engineering and System Safety, 70, 71-83,

[8] Horner, R., El-Haram, M., Munns, A., *Building maintenance strategy: a new management approach*, Journal of Quality in Maintenance Engineering, 3(4), 273-280, 1997

[9] Mitchell, J.S., *Five to Ten Year Vision for CBM*, ATP Fall Meeting – Condition Based Maintenance Workshop, Atlanta, Georgia, 1998

[10] Andersson, M., *Strategic Planning of Track Maintenance. State of the Art*, Tritainfra, 2-35, 2002

[11] Hysplip, J. P., *Substructure Maintenance Management: Its Time Has Come*, Proceedings of the Arema 2007 Annual Conference, Calgary, Canada, 2007

[12] Granstrom, R., *Maintenance for improved punctuality : a study of condition monitoring technology for the Swedish railway sector*, Ph.D. Dissertation, 2005

[13] De La Garza, J.M., Pinero, J.C., Ozbek, M.E., Via Jr., C.E., *Sampling procedure for performance-based road maintenance evaluations*, Transportation Research Record, 2044, 11-18, 2008

[14] Mitchell, J.S., *Five to Ten Year Vision for CBM*, ATP Fall Meeting – Condition Based Maintenance Workshop, Atlanta, Georgia, 1998

[15] Tosti, F., *Experimental and theoretical investigation on road pavements and materials through ground-penetrating radar*, PhD dissertation, 2014

[16] Beutel, R., Reinhardt, H.W., Grosse, C.U., Glaubitt, A., Krause, M., Maierhofer, C., Algernon, D., Wiggenhauser, H., Schickert, M., *Comparative performance tests and validation of NDT methods for concrete testing*, Journal of Nondestructive Evaluation , 27, 59-65, 2008

[17] Maierhofer, C., *Planning a non-destructive test programme for reinforced concrete structures*, Woodhead Publishing Limited, 2(1), 11-13, 2010

[18] Benedetto, A., Tosti, F., Bianchini Ciampoli, L., D'amico, F., *GPR Applications Across Engineering and Geosciences Disciplines in Italy: A Review*, IEEE Journal of Selected Topics in Applied Earth Observations and Remote Sensing, 9(7), 2952-2965, 2016

[19] Plati, C., Georgiou, P., Loizos, A., *Use of infrared thermography for assessing HMA paving and compaction*, Transportation Research Part C, 46, 192-208, 2014

[20] Daniels, D.J., *Ground Penetrating Radar*, The Institution of Electrical Engineers, London, 2004

[21] Annan, A.P., *Transmission Dispersion and GPR*, Journal of Environmental and Engineering Geophysics, 0(2), 125-136

[22] Wait, J.R., *Geo-Electromagnetism*, Accademic Press, 1982

[23] Hohmann, G.W., Ward, S.H., *Electromagnetic Theory for Geophysical Applications. Electromagnetic Methods in Applied Geophysics - Theory*, Society of Exploration Geophysicists, 1987

[24] Davis, J.L., Annan, A.P., *Applications of Ground Penetrating Radar to Mining, Ground Water and Geotechnical Projects: Selected Case Histories*, Ground Penetrating Radar, Gelogical Survey of Canada, 90(4), 49-55. 1992

[25] Jol, H., *Ground Penetrating Radar Theory and Application*, Elsevier Ed. , 2008

[26] Gagarin, N., Mekemson, J. *Step-frequency ground-penetrating-radar array calibration requirements to estimate dielectric properties of pavements*, Near Surface Geophysics, 14(2), 105-110, 2016

[27] Lahouar, S., Al-Qadi, I.L., Loulizi, A., Clark, T.M., Lee, D.T., *Approach to determining In Situ dielectric constant of pavements: Development and implementation at interstate 81 in Virginia*, Transportation Research Record, 1806(1), 81-87, 2002

[28] Loizos A., Plati C., *Accuracy of pavement thicknesses estimation using different ground penetrating radar analysis approaches*, NDT & E International, 40(2), 147-157, 2007

[29] Cauwelaert, van F., *Les bases essentielles des modeles de dimensionnement*, Journee Technique LAVOC, Ecole Polytechnique Federal de Lausanne, 1989

[30] Yoder, E.J., Witczak, M.W., *Principles of pavement design, 2nd Edition*, John Wiley & Sons, New York, 1975

[31] Forster, R.G., Ulery, H.H., *Tabulated values for determining the complete pattern of stresses, strains and deflections beneath a uniform circular load on a homogeneous half space*, Highway Research Board Bulletin, 342, 1962

[32] Burmister, D.M., *The general theory of stresses and displacements in layered soil systems*, Journal of Applied Physics, 16, 1945

[33] Burmister, D.M., *Evaluation of pavement systems of the WASHO Road Test by layered systems method*, Highway Research Bulletin, 177, 1958

[34] Huang, Y.H., *Computation of equivalent single-wheel loads using layered theory*, Highway Research Board, 1969

[35] Acum, W.E.A., Fox, L., *Computation of load stresses in a three-layer elastic system*, Geotechnique, 2, 293-300, 1951

[36] Jones, A., *Tables of stresses in three-layer elastic systems*, Highway Research Board Bulletin, 342, , 1962

[37] Peattie, K.R., *Stress and strain factors for three-layer elastic systems*, Highway Research Board Bulletin, 342, 1962

[38] Odemark, N., *Undersökning av elasticitetsegenskaperna hos olika jordarter samt teori för beräkning av beläggingar enligt elasticitetsteorin*, Stockholm, Statens väginstitut, Meddelande 77, 1949

[39] Bush, A.J., Baladi, G.J., *Nondestructive Testing of Pavements and Backcalculation of Moduli*, American Society for Testing and Materials - ASTM, STP1026, 1989

[40] Van Cauwelaert, F.J., Alexander, D.R., White, D.T., Barker, W.R., *Multilayer elastic program for backcalculating layer moduli in pavement evaluation*, American Society for Testing and Materials - ASTM, STP1026, A. J. Bush and G. Y. Baladi, eds., 1989

[41] Mehta, Y., Roque, R., *Evaluation of FWD data for determination of layer moduli of pavements*, Journal of Materials in Civil Engineering, 15(1), 25-31, 2003

[42] American Society tor Testing and Materials (ASTM) *Standard test method for measuring deflections with a Light Weight Detlectometer (LWD)*, Annual Book of ASTM Standards, E 2583, 2007

[43] K. A. Alshibli, Farsakh, M.A., Seyman, E., *Laboratory evaluation of the geogauge and light falling weight deflectometer as construction control tools*, Journal of Materials in Civil Engineering, 17(5), 560-569, 2005

[44] Benedetto, A., Tosti, F., Di Domenico, L. *Elliptic model for prediction of detlections induced by a Light Falling Weight Deflectometer*, Journal of Terramechanics, 49(1), 1-12, 2012

[45] Tosti, F., Adabi, S., Pajewski, L., Schettini, G., Benedetto, A. *Large-scale analysis of dielectric and mechanical properties of pavement using GPR and LFWD*, Proceedings of the 15th International Conference on Ground Penetrating Radar, GPR 2014, 868-873, 2014

[46] ASTM D1195/D1195M-09 , *Standard test method for repetitive static plate load tests of soils and flexible pavement components, for use in evaluation and design of airport and highway pavements*, ASTM International, West Conshohocken, PA., 2009

[47] ASTM D4695-03, *Standard Guide for General Pavement Deflection Measurements*, ASTM International, West Conshohocken, PA., 2008

[48] ASTM D4429-09a, *Standard Test Method for CBR (California Bearing Ratio) of Soils in Place*, ASTM International, West Conshohocken, PA., 2009

[49] More, R., *Ground Penetrating Radar for Evaluating Subsurface Conditions for Transportation Facilities*, Synthesis of Highway Practice, 255,National Cooperative Highway Research Program, Transportation Research Board, Washington, D.C., USA, 1998.

[50] Scullion, T.,Saarenketo, T., *Road evaluation with ground penetrating radar*, Journal of Applied Geophysics, 43, 119–138, 2000

[51] Fredlung, D. G., Rahardjo, H. , Fredlung, M.D., *Unsaturated Soil Mechanics in Engineering Practice*, Jhon Wiley & Sons Edt., 2002

[52] Mitchell, J.K., *Fundamentals of Soil Behaviour*, Second Edition. John Wiley & Sons Edt., 1993

[53] Saarenketo, T., *Electrical properties of water in clay and silty soils*, Journal of Applied Geophysics, 40(1-3), pp. 73-88, 1998

[54] Tosti, F., Patriarca, C., Slob, E., Benedetto, A., Lambot, S., *Clay content evaluation in soils through GPR signal processing*, Journal of Applied Geophysics, 97, pp. 69-80, 2013

[55] Benedetto, F., Tosti, F., *GPR spectral analysis for clay content evaluation by the frequency shift method*, Journal of Applied Geophysics, 97, pp. 89-96, 2013

[56] Tosti, F., Benedetto, A., Bianchini Ciampoli, L., Lambot, S., Patriarca, C., Slob, E.C. *GPR analysis of clayey soil behaviour in unsaturated conditions for pavement engineering and geoscience applications*, Near Surface Geophysics, 14(2), pp. 127-144, 2016

[57] Novak, M., Birgisson, B., Roque, R.,*Near-surface stress states in flexible pavements using measured radial tire contact stresses and ADINA* ,Computers & Structures, 81, 859-870, 2003

[58] Oteng-Seifah, S., Manke, P.G.,*Study of Rutting in Flexible Highway Pavements in Oklahoma (Abridgment)* ,Computers & Structures, Transportation Research Record, 602, 97-99, 1976

[59] Simpson, A.L., Daleiden, J.F., Hadley, W.O., *Rutting Analysis from a Different Perspective*,Transportation Research Record, 1473, 9-17, 1995

[60] Tosti, F., Adabi, S., Pajewski, L., Schettini, G., Benedetto, A *Large-scale analysis of dielectric and mechanical properties of pavement using GPR and LFWD*, Proceedings of the 15th International Conference on Ground Penetrating Radar, Brussels, pp. 868-873, 2014

[61] Al-Qadi, I.L., Lahouar, S., *Measuring layer thicknesses with GPR – Theory to practice*, Construction & Building Materials, 19, 763-772, 2005

[62] Tutumler, E., Little, D.S., Kim, S.-H., *A validated model for predicting field performance of aggregate base courses*, in Proc. of the 82nd Annual Meeting of the Transportation Research Board, Washington, 2003

[63] Huang, Y.H., *Pavement Analysis and Design*, Prentice-Hall Ed., 2004

[64] ISPRA – Istituto Superiore per la Protezione e la Ricerca Ambientale, http://sgi.isprambiente.it/geoportal/catalog/sgilink/map100k.page (retrieved 22 Jun. 2017).

[65] Indraratna, B., *1st ralph proctor lecture of ISSMGE. Railroad performance with special reference to ballast and substructure characteristics*, Transportation Geotechniques,7,74–114, 2016

[66] Selig, E.T., Waters, J.M.,*Track geotechnology and substructure management*,Thomas Telford Ed., London, 1994

[67] Clark, M., McCann, D.M., Forde, M.C., *Infrared thermographic investigation of railway track ballast*, Non Destructive Testing & Evaluation International, 35(2), 83–94, 2002

[68] Anbazhagan, P., Buddhima I., Amarajeevi, G., *Characterization of clean and fouled rail track ballast subsurface using seismic surface survey method: model and field studies*, Journal of Testing Evaluations,39(5),831–41,2011

[69] Donohue, S., Gavin, K., Tolooiyan, A., *Geophysical and geotechnical assessment of a railway embankment failure*, Near Surface Geophysics, 9(1), 33–44, 2001

[70] Hugenschmidt, J., *Railway track inspection using GPR*, Journal of Applied Geophysics, 43, 147–55, 2000

[71] Roberts, R., Schutz, A., Al-Qadi, I.L., Tutumluer, E., *Characterizing railroad ballast using GPR: recent experiences in the United States*, In: Proceedings of the 4th international workshop on advanced ground penetrating radar (IWAGPR 2007), Naples, Italy, 2007

[72] Railway track and structures magazine, June 1985

[73] Clark, M.R., Gillespie, R., Kemp, T., McCann, D.M., Forde, M.C., *Electromagnetic properties of railway ballast*, Non Destructive Testing & Evaluation International, 34(5), 305–311, 2001

[74] Sussmann, T.R., O'Hara, K.R., Selig, E.T., *Development of material properties for railway application of ground penetrating radar*, In: Proceedings of the society of photooptical instrumentation engineers (SPIE), vol. 4758, 2002

[75] Tosti, F., Benedetto, A., Calvi, A., Bianchini Ciampoli, L., *Laboratory investigations for the electromagnetic characterization of railway ballast through GPR*, In Proceedings of the 16th international conference of ground penetrating radar (GPR 2016), Hong Kong, 2016

[76] Fontul S., Fortunato, E., De Chiara, F., *Evaluation of ballast fouling using GPR*, In Proceedings of the 15th international conference on ground penetrating radar (GPR 2014), 418–422, Bruxelles, Belgium, 2014

[77] Anbazhagan, P., Naresh Dixit, P.S., Bharatha, T.P., *Identification of type and degree of railway ballast fouling using ground coupled GPR antennas*, Journal of Applied Geophysics, 126, 183–190, 2016

[78] Roberts, R., Rudy, J., Al-Qadi, I.L., Tutumluer, E., *Railroad ballast fouling detection using ground penetrating radar – a new approach based on scattering from voids*, In Proceedings of the ninth european conference on NDT (ECNDT 2006), 1–8, Berlin, Germany, 2006

[79] Forde, M.C, De Bold, R., O'Connor, G., Morrissey, J.P., *New analysis of ground penetrating radar testing of a mixed railway trackbed*, In Transportation Research Board annual meeting, 2010

[80] Leng, Z., Al-Qadi, I.L., *Railroad ballast evaluation using ground-penetrating radar*, Transportation Research Records, 2159, 110–117, 2010

[81] Shao, W., Bouzerdoum, A., Phung, S.L., Su, L., Indraratna, B., Rujikiatkamjorn, C., *Automatic classification of ground-penetrating-radar signals*

for railway-ballast assessment, IEEE Transactions on Geoscience and Remote Sensing,49(10), 3961–72, 2011

[82] Xiao, J., Liu, L., *Multi-frequency GPR signal fusion using forward and inverse S-transform for detecting railway subgrade defects*, In Proceedings of the 8th international workshop on advanced ground penetrating radar (IWAGPR 2015), Florence, Italy, 2015

[83] Zhang, Q., Gascoyne, J., Eriksen, A., *Characterisation of ballast materials in trackbed using ground penetrating radar: part 1*, In Proceedings of the 5th IET conference on railway condition monitoring and non-destructive testing (RCM 2011), 1–8. Derby, United Kingdom, 2011

[84] Benedetto, A., Tosti, F., Bianchini Ciampoli, L., Calvi, A., Brancadoro, M.G., Alani, A.M., *Railway ballast condition assessment using ground-penetrating radar – an experimental, numerical simulation and modelling development*, Construction & Building Materials, 140, 508–20, 2016

[85] Bianchini Ciampoli, L., Tosti, F., Brancadoro, M.G., D'Amico, F., Alani, A.M., Benedetto, A., *A spectral analysis of ground-penetrating radar data for the assessment of the railway ballast geometric properties*, Non Destructive Testing & Evaluation International, 90, 39-47, 2017

[86] Tosti, F., Bianchini Ciampoli, L., Calvi, A., Alani, A.M., Benedetto, A., *An Investigation into the railway ballast dielectric properties using different GPR antennas and frequency systems*, Non Destructive Testing & Evaluation International, In press, 2017

[87] Benedetto, A., Tosti, F., Bianchini Ciampoli, L., Alani, A.M., Umiliaco, A., Brancadoro, M.G., *A simulation-based approach for railway applications using GPR* , In Proceedings of 2016 16th International Conference of Ground Penetrating Radar, GPR 2016, Hong Kong, 2016

[88] ASTM D6087-08, *Standard Test Method for Evaluating Asphalt-Covered Concrete Bridge Decks Using Ground Penetrating Radar*, ASTM International, West Conshohocken, PA, 2008

[89] F. Benedetto, F. Tosti, *A signal processing methodology for assessing the performance of ASTM standard test methods for GPR systems*, Signal Processing, 132, 327–337, 2017

[90] Bianchini Ciampoli, L., D'Amico, F., Calvi, A., Benedetto, F. and Tosti, F., *Signal processing for optimisation of low-powered GPR data with application in transportation engineering (roads and railways)*, In Proceedings of the Tenth International Conference on the Bearing Capacity of Roads, Railways and Airfields (BCRRA 2017), June 28-30, Athens, Greece, 2017

[91] EN 13450:2002/AC:2004, *Aggregates for railway ballast*, European Commission for Standardization, 2004.

[92] EN 1097-3:1998, *Tests for mechanical and physical properties of aggregates - Part 3: Determination of loose bulk density and voids*, European Committee for Standardization, 1998

[93] CEN ISO/TS 17892-1:2014, *Geotechnical investigation and testing - Laboratory testing of soil - Part 1: Determination of water content*, European Committee for Standardization, 2014

[94] EN 933-1:2012, *Tests for geometrical properties of aggregates - Part 1: Determination of particle size distribution -Sieving method*, European Committee for Standardization, 2012

[95] EN 933-4:2008, *Tests for geometrical properties of aggregates - Part 4: Determination of particle shape - Shape index*, European Committee for Standardization, 2008

[96] EN 1097-2:2010, *Tests for mechanical and physical properties of aggregates - Part 2: Methods for the determination of resistance to fragmentation*, European Committee for Standardization, 2010

[97] EN1097-6:2013, *Tests for mechanical and physical properties of aggregates-Part 6:Determination of particle density and water absorption*, European Committee for Standardization, 2013

[98] ASTM D4318-10e1, *Standard Test Methods for Liquid Limit, Plastic Limit, and Plasticity Index of Soils*, ASTM International, West Conshohocken, PA, 2010

[99] EN ISO 17892-3:2015, *Geotechnical Investigation and Testing – Laboratory Testing of Soil – Part 3: Determination of Particle Density*, European Committee for Standardization, 2015

[100] EN 13286-2:2005, *Unbound and Hydraulically Bound Mixtures – Part 2: Test Methods for the Determination of the Laboratory Reference Density and Water Content– Proctor Compaction*, European Committee for Standardization, 2015

[101] Benedetto, A., Umiliaco, A., *Evaluation of hydraulic permeability of open-graded asphalt mixes using a full numerical simulation*, Journal of Materials in Civil Engineering, 26(4), 599–606, 2014

[102] Birchak, J.R., Gardner, C.G., Hipp, J.E., Victor, J.M., *High dielectric constant microwave probes for sensing soil moisture*, Proc. IEEE, 62, 93–102,1974

[103] Lichtenecker, K., Rother, K., *Die herleitung des logarithmischen mischungsgesetzes aus allgemeinen prinzipien der stätionaren strömung*, Phys. Z , 32, 255–260, 1931

[104] Fensler, W.E. , Knott, E.F., Olte, A., Siegel, K.M., *The electromagnetic parameters of selected terrestrial and extraterrestrial rocks and glasses*, in: Z. Kopal, Z.K. Mikhailov (Eds.), The moon, IAU Symposium, 14, 545–565

[105] Van Geem, C., *Overview of interpretation techniques based on measurement of deflections and curvature radius obtained with the Curviameter*, in: 6th European FWD User's Group Meeting, Sterrebeek, 10-11 June, 2010

[106] Simonin, J.M., Geffard, J.L., Hornych, P., *Performance of Deflection Measurement Equipment and Data Interpretation in France*, in: International Symposium Non-Destructive Testing in Civil Engineering, September 15 - 17, Berlin, Germany, 2015

About the author

Luca Bianchini Ciampoli was born in Rome, Italy, on September 10th, 1989. He obtained in 2011 a B.Sc. in Civil Engineering from Roma Tre University in Rome, Italy. In the summer of 2014 he achieved the M.Sc. graduation at the same University in "Road Infrastructure and Trasportation Engineering". His Master Thesis, entitled "Frequency-based evaluation of physical properties of bearing soils through GPR", was developed at the Delft University of Technology, where he attended the Faculty of Civil Engineering and Geosciences as a visiting student.

He was finally granted of a Ph.D. scholarship from the Department of Engineering at Roma Tre University, in September 2014. During his Ph.D. he had the opportunity to attend the University of West London as guest researcher between September 2015 and January 2016, within the context of a project funded by COST Action TU1208 "Civil Engineering Application of Ground Penetrating Radar", focused on "Ground Penetrating Radar applications in Tunnels".

International journal publications

- Tosti, F., Bianchini Ciampoli, L., D'Amico, F., Alani, A. M., Benedetto, A., 2017e, An Investigation into the railway ballast dielectric properties using different GPR antennas and frequency systems. Non-Destructive Testing & Evaluations International, 93, 131-140, 2018 [I.F. 2.77]

- Benedetto, A., Tosti, F., Bianchini Ciampoli, L., Calvi, A., Brancadoro, M.G., Alani, A.M., 2017, Railway ballast condition assessment using ground-penetrating radar – An experimental, numerical simulation and modelling development. Construction & Building Materials, 140, 508-520, 2017 [I.F. 3.17]

- Bianchini Ciampoli, L., Brancadoro, M.G., Tosti, F., D'Amico, F., Alani, M.A., Benedetto, A., 2017, A spectral analysis of ground-penetrating radar data for the assessment of the railway ballast geometric properties. Non-Destructive Testing & Evaluations International, 90, pp. 9-47, 2017 [I.F.

2.77]

- Benedetto, A., Tosti, F., Bianchini Ciampoli, L., Calvi, A., Brancadoro, M.G., Alani, A.M., 2017, Railway ballast condition assessment using ground-penetrating radar: An experimental, numerical simulation and modelling development. Construction & Building Materials, 140, pp. 508-520, 2017 [I.F. 3.17]

- Benedetto, A., Tosti, F., Bianchini Ciampoli, L., D'Amico, F., A review of ground-penetrating radar signal processing techniques for advanced road inspections. Signal Processing, 132C, 201-209, 2017 [I.F. 3.11]

- Tosti, F., Benedetto, A., Bianchini Ciampoli, L., Lambot, S., Patriarca, C., and Slob, E.C., GPR analysis of clayey soils behavior in unsaturated conditions for pavement engineering and geoscience applications. Near Surface Geophysic, Vol. 14, 127-144, 2016 [I.F. 1.30]

- Benedetto, A., Tosti, F., Bianchini Ciampoli, L., D'Amico, F., Applications of Ground Penetrating Radar in Italy: a Review, IEEE Journal of Selected Topics in Applied Earth Observations and Remote Sensing, 9 (7), 2952-2965, 2016 [I.F. 2.91]

Accepted for publication

- Benedetto, A., Brancadoro, M.G., Bianchini Ciampoli, L., Alani, A.M., Tosti, F., 2017, A novel computer-aided model for the simulation of railway ballast by random sequential adsorption process. Computer-Aided Civil and Infrastructure Engineering, In press [I.F. 5.79]

- Tosti, F., Bianchini Ciampoli, L., D'Amico, F., Alani, A. M., Benedetto, A., 2017, An experimental based model for the assessment of the mechanical properties of road pavements using GPR. Construction & Building Materials, In Press [I.F. 3.17]

Conference publications

- Brancadoro, M.G., Bianchini Ciampoli, L., Ferrante, C., Benedetto, A., Tosti, F., Alani, A.M., An Investigation into the railway ballast grading using GPR and image analysis, 9th International Workshop on Advanced Ground Penetrating Radar (IWAGPR), Edinburgh, UK, 2017

- Alani, A.M., Tosti, F., Bianchini Ciampoli. L., Benedetto, F., Road foundation detailing using ground penetrating radar systems with different frequencies, 9th International Workshop on Advanced Ground Penetrating Radar (IWAGPR), Edinburgh, UK, 2017

- Pajewski, L., Benedetto, A., Loizos, A., Plati, C., Derobert, X., Tosti, F.,Alani, A.M., Bianchini Ciampoli, L., Perez-Garcia, V., GPR: main results achieved by Working Group 2 of COST Action TU1208. 10th International Conference on Bearing Capacity of Roads, Railways and Airports, Athens, Greece, 2017

- Tosti, F., Alani, A.M., Benedetto, A., Bianchini Ciampoli, L., Brancadoro, M.G., Pajewski, L., Investigation of flexible pavement by reflection amplitude data and FTDT modeling of high-frequency air-coupled GPR signals, 10th International Conference on Bearing Capacity of Roads, Railways and Airports, Athens, Greece, 2017

- Bianchini Ciampoli, L., D'Amico, F., Calvi, A., Tosti, F., A post processing scheme for optimising the signal of low-powered GPR systems in transportation engineering surveys. 10th International Conference on Bearing Capacity of Roads, Railways and Airports, Athens, Greece, 2017

- Brancadoro, M.G., Tosti, F., Bianchini Ciampoli, L., Pajewski, L., Pirrone, D., Benedetto, A., Alani, A.M., , How to create a full-wave GPR model of a 3D domain of railway track bed?. 10th International Conference on Bearing Capacity of Roads, Railways and Airports, Athens, Greece, 2017

- Bianchini Ciampoli, L., Tosti, F., Alani, A.M., Calvi, A., Benedetto, A., Railway ballast efficient maintenance through GPR: a review. 10th International Conference on Transport Infrastructures and System, Rome, Italy, 2017

- Benedetto A., Tosti F., Bianchini Ciampoli L., Pajewki L., Pirrone D., Umiliaco A., Brancadoro M.G., A simulation based approach for railway applications using GPR. 16th International Conference on Ground Penetrating Radar (GPR 2016), Hong Kong, Hong Kong, 2016

- Tosti F., Benedetto A., Calvi A., Bianchini Ciampoli L., 2016c, Laboratory Investigations for the Electromagnetic Characterization of Railway Ballast through GPR. 16th International Conference on Ground Penetrating Radar (GPR 2016), Hong Kong

- Bianchini Ciampoli, L., Alani, A.M., Benedetto, A., Tosti, F., Buried utilities detection with GPR: a comparison between employed central frequencies and processing procedures configurations. 16th International Conference on Ground Penetrating Radar (GPR 2016), Hong Kong, Hong Kong, 2016

- Tosti, F., Bianchini Ciampoli, L., Benedetto, A., Calvi, A., D'Amico, F., Prediction of rutting evolution in flexible pavement life cycle at the road network scale using an air-launched ground-penetrating radar system. 16th International Conference on Ground Penetrating Radar (GPR 2016), Hong Kong, Hong Kong, 2016

- Benedetto, A., Tosti, F., D'Amico, F., Bianchini Ciampoli, L., A semiempirical approach for investigating mechanical properties of pavement through GPR, Proc. of the COST Action TU1208 "Civil Engineering Applications of Ground Penetrating Radar" 2nd General Meeting, Vienna, Austria, 2015

- Tosti, F., D'Amico, F., Calvi, A., Bianchini Ciampoli, L., Benedetto, A., Potential of an air-launched GPR system for detecting pavement damages evolution: a case study. Proc. of the COST Action TU1208 "Civil Engineering Applications of Ground Penetrating Radar" 2nd General Meeting, Vienna, Austria, 2015

Accepted for publication

- Alani, A., Bianchini Ciampoli, L., Tosti, F., Brancadoro, M.G., Pirrone, D. and Benedetto, A., Health monitoring of a matured tree using ground penetrating radar – investigation of the tree root system and soil interaction (Extended Abstract). In: METROARCHAEO2017, 23-25 Oct 2017, Lecce, Italy, 2017, In Press

- Alani, A., Tosti, F., Banks, K., Bianchini Ciampoli, L. and Benedetto, A. (2017) Non-destructive assessment of a historic masonry arch bridge using ground penetrating radar and 3D laser scanner. In: METROARCHAEO2017, 23-25 Oct 2017, Lecce, Italy 2017, In Press

National journal publications

- Calvi A., Bianchini Ciampoli L., Brancadoro M.G., Cutolo E., Ballast Ferroviario: Monitoraggio del Degrato con Georadar. Strade&Autostrade, 3, 2016

- Benedetto A., Tosti F., Bianchini Ciampoli L., Georadar: le proprietà meccaniche della sovrastruttura stradale, Strade&Autostrade, 4, 2015

Acknowledgements

This thesis presents part of the scientific results that I achieved within the context of my PhD course.

However, what it can not describe is the wide extent of human and cultural experiences that I had the opportunity to face, during these three years.

Much of this I owe to my supervisor Prof. Dr. Andrea Benedetto, who from the beginning trusted on my quality beyond my actual worths. Most of all, I am grateful for his straitforwardness, and for the sincere concern about my growth as both a scientist and a man.

Also, I can hardly find the words to express my gratitude to Dr. Fabio Tosti. I have no doubts that, without his precious advices, bright example, and unvaluable friendship, my PhD would have yielded me much less satisfactions.

I could never forget the huge amount of "core-a-core" coffees taken with Spartaco Cera, nor the long hours of travel spent onto the Piaggio Porter during the surveys, nor of course how lucky I was to share my experience, along with the office, with such a person and a friend.

I am a firm believer of the Research as a path of sharing and cooperation, rather than of competition. In this sense, I owe much of my results to the colleagues surrounding me during this three years. I am very grateful to have found colleagues and friends as Chiara, Maria Giulia and Valerio, who shared my human and scientific joys and anxieties. I only wish I gave you back the same unvaluable support that you gave me, through these years.

Furthermore, I would like to thank Dr. Alessandro Calvi and Dr. Fabrizio D'Amico for the inspiration and guidance they provided me as young and talented researchers. Also, thank you for showing me how to properly tackle a survey mission.

I also wish to acknowledge Prof. Dr. Amir Morteza Alani for the support and the advices he granted me during the months I spent as visiting researcher at the University of West London. I would like to thank my external examiners, Prof. Dr. Andreas Loizos and Prof. Dr. Jorge Pais that, together with mentioned

Prof. Dr. Amir Morteza Alani, have agreed to embark on the task of evaluating the work presented in this document.

Finally, my deepest gratitude goes to my parents for all the kind of efforts spent on my human and cultural growth, and for the lessons teached me through their example, that I always keep in mind, as I always will.